Stony Brook University

Dynamic Behavior of Cellular Architectures and the Role of Topology

A Thesis Presented

by

Vincent Brick

to

The Graduate School

in Partial Fulfillment of the

Requirements

for the Degree of

Master of Science

in

Mechanical Engineering

Stony Brook University

December 2013

Stony Brook University

The Graduate School

Vincent Brick

We, the thesis committee for the above candidate for the

Master of Science degree, hereby recommend

acceptance of this thesis.

Maen Alkhader
Assistant Professor, Mechanical Engineering

Lifeng Wang
Assistant Professor, Mechanical Engineering

T. Venkatesh
Assistant Professor, Materials Science and Engineering

This thesis is accepted by the Graduate School

Charles Taber
Dean of the Graduate School

Abstract of the Thesis

Dynamic Behavior of Cellular Architectures and the Role of Topology

by

Vincent Brick

Master of Science

in

Mechanical Engineering

Stony Brook University

2013

This work investigates the dependence of strength and energy absorbance characteristics of cellular solids on inner topological features under high-strain-rate normal and mixed mode loading conditions. Topological features investigated in this work include cellular geometry, connectivity, in-plane and out-of-plane cellular aspect ratios. Varying the cellular geometry and connectivity is achieved by investigating cellular specimens with hexagonal, triangular, and square core cell geometries. This work utilizes explicit dynamic finite element simulations to examine the relationships among strength, energy absorbance, cellular geometry, and the underlying deformation mechanisms. Results over the length scales examined strongly indicate that hexagonal geometry has higher specific and overall energy absorption during all modes of loading when compared to triangular or square geometry. The controlling mechanism is identified as a combination of the number of plastic hinges present in each buckling leg and the distance between hinges (wave length). In addition, plastic hinges are found to be accountable for approximately all the absorbed energy, while the material between hinges is effectively unloaded. The way found to effectively control hinge formation is by controlling out-of-plane aspect ratio *H/L*.

In addition to the topology-energy coupling, this work investigates the potential for enhancing the energy absorbance characteristics and capacity of cellular solids by integrating them with a polymeric matrix such that the polymer fills all cellular voids. Results show that a composite cellular-polymer system with rate-responsive polymer has the potential to be used to create highly customized energy absorbing and force-shielding material. In addition, results show that for such composite system to be effective, its constituent materials (cellular and polymer) should be of comparable compliance.

To my Family

Table of Contents

Chapter 1 - Motivation

1.1 - Introduction

A honeycomb structure is one of three types of cellular solids, the other two being three dimensional open or closed foams as shown in Figure 1.1.1. Two-dimensional honeycombs like the ones used throughout this work, can be made by press forming sheets of metal into corrugated sheets and gluing them together. This gives double thickness at the bonded portion. Paper or cardboard honeycombs are similarly formed. Extrusion is another process, using a dye to create uniform wall thickness throughout the honeycomb if desired. The extrusion forming process is becoming more popular for honeycombs so this work assumes uniform wall thickness via an extrusion forming method [1]. The extrusion method is also advantageous because as with any type of bonding, delamination may occur if the bond has shear tolerance less than the bulk material or if it has degraded performance under varying temperature. Honeycombs are widely used as packaging aids, structural components, and energy absorbers.

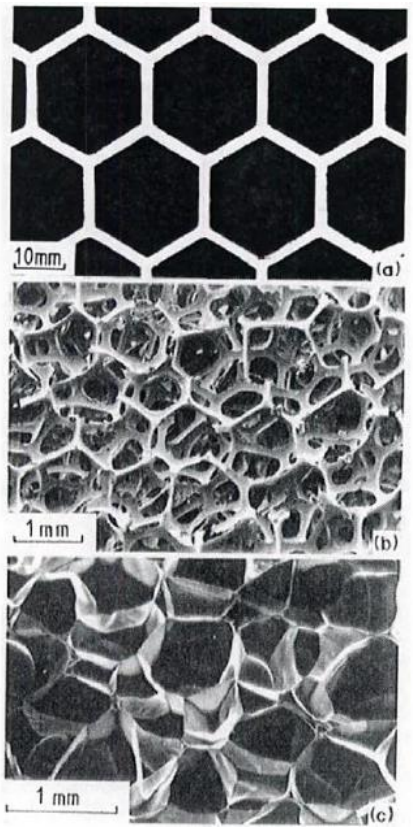

Figure 1.1.1 – The three types of cellular solids; (a) 2D honeycomb, (b) 3D open cell foam, and (c) 3D closed cell foam [1].

Packaging aids come mostly in paper or cardboard form because it's expensive to ship as weight increases. Lightweight foam packing peanuts are three-dimensional cellular structures, being a staple of the packaging industry because of their lightweight strength properties. Anything built with balsa wood is making use of the three-dimensional open cellular structure. Aircrafts use aluminum or paper-resin honeycombs as part of a composite sandwich panel system to provide superior bending stiffness and strength [1]. Bones also make use of cellular structure for support at reduced weight. It would be difficult to find any lightweight high strength structure that isn't fundamentally rooted in cellular solids.

Energy absorbance, along with force shieldability, are the focus of this work. Proceeding chapters will show that force shieldability is intrinsically related to energy absorbance and peak crush strength. Force shieldability can be defined as the mismatch between peak forces exerted on top and bottom honeycomb surfaces. Crush strength is the peak stress or force exhibited before progressive collapsing and bulk energy absorbance occurs. Energy absorbance and force shielding are important during impact scenarios and more often than not, weight and volume are restrictive factors. Honeycombs are widely used in the automotive and rail industries [2]. Aluminum is typically the core of choice because it offers high crush strength to weight ratio, a linear force curve with constant load, and absorbs energy over a long stroke [3]. It's not uncommon for honeycombs to be made from other materials, such as stainless-steel or polymers.

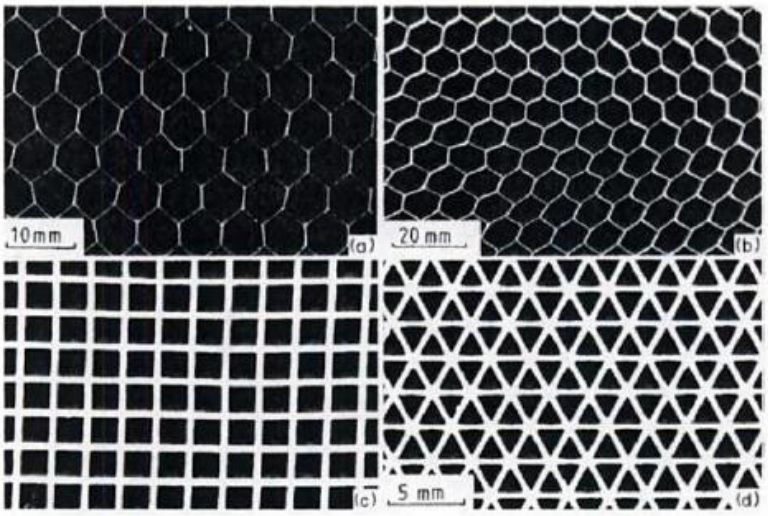

Figure 1.1.2 – More 2D honeycombs; (a) aluminum, (b) paper-phenolic resin, (c) square-cell ceramic, and (d) triangular-cell ceramic.

1.2 - Literature Review

While several things need to be considered during a literature review, the goal is to capture the progression of research over time. Since this thesis aims to identify optimal honeycomb geometry for energy absorption under dynamic loading, the literature review must encompass fundamental work involving and preceding dynamic absorption—namely dynamic and quasi-static experiments and simulations. These works are the focus of review in Section 1.2.1.

Several parameters, such as specimen height, cell size, and material to name a few, affect how cellular structures respond to loading. This work aims to investigate how geometric parameters such as wall thickness t, cell size L, extrusion height H and aspect ratios t/L, H/L, influence specific energy absorbed by different topologies. Since these studies involve small samples subjected to dynamic displacement, it may be necessary to consider the contribution strain-rate. Section 1.2.2 is used to display relevant materials strain rate sensitivity.

1.2.1 - Honeycomb Structures

Interest in honeycomb structures has grown ever since T. Wierzbicki published his analytical method in 1983. He used angle elements in a hexagonal cell structure to capture progressive collapsing during axial loading [4]. His work provided Eq. (1.2.1), an extremely simple function for describing the mean crush strength P_m of honeycombs. The parameters are wall thickness h, flow stress σ_o, and leg length D. Wierzbicki used this expression for mean crush strength to derive Eq. (1.2.2) and compare it to the experimental results of [5]. He found the best agreement when flow stress is equal to seventy-percent of ultimate strength.

$$P_m = 8.61\sigma_0 h^{\frac{5}{3}} D^{\frac{1}{3}} \tag{1.2.1}$$

$$\bar{\sigma}_m = 16.56\sigma_0 \left(\frac{h}{S}\right)^{5/3} \tag{1.2.2}$$

A comparison to Wierzbicki's model [6] shows a linear relationship between total number of cells and crush strength, proving the theoretical model from [4] vastly underestimates crush strength and buckling wavelength. They also found dynamic crush strength increases of 33% - 74% depending on impactor velocity. They attribute this enhancement to increasingly complex failure mechanisms, inertial and strain-rate effects, etc. Aluminum alloys 5052 and 5056 were the materials for their experiments. Ultimately, the recommendation was to use high-strength material with small cell size and core height to maximize the energy absorbance of hexagonal honeycombs.

A study [7] on how relative density effects the crush strength of stainless steel square honeycombs lead to Eq. (1.2.3). Their approach to relative density variation is to change cell size while holding wall thickness constant. They found Eq. (1.2.3) to fit their experimental results very well for square and regular hexagonal honeycombs. Peak stress is σ_p while $\bar{\rho}$ is relative density. This is the first time the onset of buckling in honeycombs is described by relative density.

$$\frac{\sigma_p}{\sigma_y \bar{\rho}} = 9.9\bar{\rho}^{0.75} \tag{1.2.3}$$

It has been shown that changing hexagonal angle regularity has no effect on mean crush strength once normalized by relative density [8]. This finding may imply a relationship between branch connectivity and crush strength because connectivity remains constant while angle changes.

An elastic-plastic linear hardening model was used to simulate response of a single three-point intersection of a hexagonal honeycomb by varying wall thickness t and branch angle [9].

They find that a regular hexagonal honeycomb (branch angle of 120º) has the highest crush strength (mean crush value throughout oscillatory collapse) per net cross-sectional honeycomb area. However when crush strength is evaluated per total occupied area, the results indicate lower branch angle yields a higher crush tolerance. The latter gives the inaccurate implication that lower branch angle leads to enhancements however this is only true when ignoring the mass contribution of the honeycomb. The former is a better performance exploitation because normalizing by material allows for an intrinsic rating.

The in-plane orientation of a regular hexagonal honeycomb structure is shown to impact failure strength under axial dominant mixed mode quasi-static loading [10]. Inherently, energy absorption rate is maximized when orientation angle reaches that for which failure strength is maximized. The experiments show between 10% increase and 28% decrease in energy absorption rate depending on shear contribution and in-plane orientation. This method has been extended to exploit any differences between proportional and non-proportional quasi-static combined loading [11]. The experimental results indicate that crush strength and non-normality plastic flow behavior are independent of loading path sequence and proportionality.

The out-of-plane compressive response of square honeycombs having relative density 10% with cell heights of 30 mm and 6 mm has been measured with impact velocities ranging from quasi-static to 300 m/s [12]. Results indicate strain rate sensitivity and web buckling inertial stabilization dominate the 30 mm specimens below 50 m/s, increasing front and back face stresses by a factor of two. This is significant considering the material used (304 stainless steel) has a dynamic strength enhancement factor of only 1.5 at the prescribed strain rate. This implies strain rate sensitivity may have an exaggerated effect when exploited in square honeycombs. Their technique for numerical analysis also proves to be in good agreement with experimental results.

Experimental results indicate that slightly irregular aluminum honeycombs under quasi-static axial compression have about sixty times higher mean crush strength than when loaded across faces [13]. In-plane loading across a top or bottom face is pure shear, so mean crush strength should be severely reduced during shear dominant loading due to the compromise in structural support.

Numerical and experimental results indicate a strong relationship between the number of layers axially in a honeycomb and increased crush strength [14]. Numerical studies show a linear

relationship while experimental results indicate nonlinearity. The numerical study also shows a decay relationship between foil thickness and crush strength. Experiments performed at quasi-static and approximately 2700 s^{-1} show stress enhancement due to strain rate sensitivity. It should be noted that single and multiple layer samples did not maintain the same overall height or relative density.

Expanded polystyrene foam is used to form a series composite system for axial loading in [15]. They use quasi-static and 7.5 m/s impact testing on regular hexagonal aluminum honeycombs back by EPS, forming a hybrid series setup. They observe energy absorption increased with the amount of honeycomb in the composite. Only marginal increases were observed due to strain rate sensitivity. Energy was additionally absorbed when honeycomb tore into the foam during collapse.

Systems composing of thin-walled aluminum tubes filled with hexagonal honeycombs may perform better when the honeycomb filler cell size is decreased [16]. An improvement is made in [17] to Wierzbicki's analytical model by considering curvature effects and flow stress. In doing so, mean crushing stress and wavelength calculation errors are each decreased by 15%.

A comprehensive study on the dynamic strength enhancement of hexagonal honeycombs subjected to combined loading is performed in [18]. The author finds peak and average strengths to decrease significantly with loading angle. Dynamic strength enhancement is found for every loading angle but becomes more pronounced as loading angle increases. They also study the effect cell-size and cell-wall thickness have on dynamic enhancement. Experimental results indicate larger cells with thin walls have an improved dynamic enhancement when compared to smaller cells with thicker walls. This is observed to be because larger cells are weaker when thickness is held constant, meaning failure loads are lower. As failure load decreases, any dynamic enhancement over quasi-static loading becomes more pronounced. The opposite occurs for smaller cells with thicker walls, where their elevated strength forces any dynamic enhancements to be less pronounced. They find the material of the honeycomb has large influence over dynamic enhancement.

1.2.2 - Strain Rate Sensitivity

It's necessary to investigate the strain rate sensitivity of a broad range of materials because honeycombs are being used for an increasing range of applications. These applications may be

static/structural, dynamic, or temperature sensitive. Dynamic applications may require force shielding such that plastic or metal materials are required as an absorber. This section is used to investigate the bulk and local strain-rate sensitivity of a broad range of honeycomb material candidates.

The strain rate sensitivity of 304L Stainless Steel has been experimentally investigated [19] by means of uniaxial tension and compression tests across 10^{-4} s^{-1} to 10^{4} s^{-1}. They used their experimental results to develop Eq. (1.2.4), expressing yield stress dependence on strain rate at room temperature. They find this relationship works well from quasi-static to about 100 s^{-1} but increasingly underestimates sensitivity thereafter. They attribute this mismatch at higher strain rates to an increased sensitivity during structural collapse. Their results show at least a 60% increase in yield stress from quasi-static to 10^{4} s^{-1}.

$$\dot{\epsilon} = 4.4 * 10^{7} * exp\left\{-302\left[1-\left(\frac{\sigma}{751}\right)^{\frac{1}{2}}\right]^{\frac{3}{2}}\right\} \tag{1.2.4}$$

The strain rate sensitivity of seventeen different polymers has been investigated [20] using uniaxial compression from quasi-static to 3 x 10^{4} s^{-1}. They find there is generally a log-linear relationship between strain rate and stress from quasi-static to 10^{3} s^{-1}. It's also found that measurements taken consistently at different strains weakly influenced sensitivity. Five of the seventeen—ABS, PET, PP, PVC, PVDF—showed a sudden increase in sensitivity at 10^{3} s^{-1}, establishing a new log-linear relationship. This means a threshold strain-rate exists, beyond which sensitivity increases rapidly for certain polymers.

The strain rate sensitivity of three common polymeric foams—expanded polystyrene, high-density polyethylene, and polyurethane—has been measured [21] from quasi-static to 2500 s^{-1}. The results confirm the bilinear rate sensitivity relationship witnessed by [20] for rates below and beyond 10^{3} s^{-1}.

Epoxy-based polymeric structural foams having densities and porosities between 0.83 – 1.46 g/cm^{3} and 50.5 – 6.8%, respectively, have been compared [22] from quasi-static to a strain rates up to 550 s^{-1}. Results indicate increased Young's Modulus and higher ultimate stress and strain failure under quasi-static loading as bulk density increases. High-density foams exhibit shear-dominated failure with large strain rates while low-density foams have random macroscopic failure. The foams exhibit increased yield stress and failure strength but decreased strain-to-failure

values under high strain-rates. Lastly, higher initial bulk density resulted in higher increased strain rate sensitivity and failure strength.

The compressive strain rate sensitivity of Polyurea and Polyurethane have been investigated from quasi-static to 10^4 s^{-1} [23]. Results indicate both are very rate sensitive, Polyurea having up to a five factor increase in flow stress at 10^5 s^{-1} and Polyurethane with a true yield stress increase factor of seventy.

A continuously extruded steel matrix is subjected to quasi-static and dynamic compression up to 10^3 s^{-1} in [24]. They find damage phenomena such as crack formation becomes significant at higher strain rates, dampening dynamic enhancement.

The high strain rate viscoplastic response of aluminum alloys 6082-T6 and 7075-T6 has been experimentally investigated [25]. Both materials exhibit a sharp enhancement just before 10^4 s^{-1}—alloy 6082 more than doubles its true stress when strain rates approach $4_E{}^4$ s^{-1}.

A unified constitutive model for the dynamic increase factor DIF of brittle and ductile materials has been proposed [26]. This model accurately approximates low-high strain-rate enhancement for a wide range of materials. The strain-rate range is quasi-static to 10^4 s^{-1} for most cases. Dynamic enhancement seems to plateau beyond this loading rate. The material constants for Eq. (1.2.5) are given in the corresponding article.

$$DIF = (1 + A\varepsilon^n)\left\{DIF_{max} - \frac{DIF_{max} - [1 + B(log\,\dot{\varepsilon} - log\,\dot{\varepsilon}_0)]}{1 + exp[C(log\,\dot{\varepsilon} - log\,\dot{\varepsilon}_0)]}\right\} \qquad (1.2.5)$$

Chapter 2 - Modeling Technique

2.1 - Introduction

It's important to have a sound approach when performing these analysis, so this chapter focuses of establishing a guideline to follow. How Abaqus uses the Finite Element Method is first described in Section 2.2. The modeling aspects most relevant to this work are element type, mesh, and boundary conditions. Holding extrusion height *H* constant for all simulations while controlling loading rate allows each topology to be subjected to the same strain-rate. Finding the mesh density where response is independent of element size is also important and is shown in Section 2.3.1. These findings are used during the benchmark in Section 2.4.

2.2 - The Finite Element Method

The finite element method (FEM) allows a domain to be discretized into finite and measureable quantities called elements. These elements are subjected to loading just as would be in a physical situation and results are obtained based on elemental displacement. The method is rooted with the ability to satisfy stress equilibrium through the principle of virtual work [27]. Finite element analysis (FEA) exclusively applies FEM to solve problems. The object of this chapter is not to derive FEM but to highlight how Abaqus uses it to solve problems applicable to this work.

FEM can be used to solve all kinds of problems but to cover the bulk of them, one would say the method is used to solve either static or dynamic problems. The equilibrium equations are the same, being that static and dynamic problems can ultimately be defined by Eq. (2.2.1). This is the equation of motion for a dynamic system but simplifies to Eq. (2.2.2) when static problems are being solved. *M* denotes a mass matrix, *K* a stiffness matrix, *u* a displacement vector, and *F* a force vector. Double overbars indicate an *n x n* matrix whereas a single overbar represents an *n x 1* vector. All physical quantities are concentrated at element characteristic points called nodes.

$$\bar{\bar{M}}\frac{d^2\bar{u}}{dt^2} + \bar{\bar{K}}\bar{u} = \bar{F}(t) \tag{2.2.1}$$

2.2.1 - Static

Static problems are those with no time dependence—namely, those where inertial forces are neglibeable. Structural problems and others where acceleration can be ignored fall under into the 'static' regime. Ignoring inertial effects means Eq. (2.2.1) simplifies to Eq. (2.2.2). Static

problems are either linear or nonlinear, the latter involving contact, plasticity, or large geometric variation. Linear static problems are solved all at once by simply inverting Eq. (2.2.2). Non-linear static problems lead to a system of nonlinear equations which unfortunately cannot be inverted until they're linearized. These types of problems have path dependent solutions, meaning the end result is a compilation of all preceding steps. Total loading is normally reached after several smaller increments to ensure the solution converges.

$$\bar{F} = \bar{\bar{K}}\bar{u} \tag{2.2.2}$$

$$\bar{F}(\bar{u}) = 0 \tag{2.2.3}$$

As seen in Eq. (2.2.3), the problem is now emphasized as a balance between internal and external forces. Problems involving plasticity are nonlinear but essentially mean stiffness is a function of displacement. It's important to understand that *Ku* hasn't been set to zero in Eq. (2.2.3), but is more or less absorbed into the left hand side. The force vector is nonlinear, composed of external and internal parameters that ultimately dictate the movement of each node. *F* is, as before, a vector of length characteristic to the problem size. The first step in solving a nonlinear static problem is to expand each *F* component as a Taylor series. This is done in Eq. (2.2.4) , where $f(u_0)$ represents one component of the total force vector. Eq. (2.2.4) is easily rearranged to solve for the displacement of the current step. This is done over and over until **F** is below a preset tolerance or essentially equal to zero.

$$f(u_0) + (u - u_0)\left(\frac{df(u)}{du}\right)_{u=u0} = 0 \tag{2.2.4}$$

$$u - u_0 = \Delta u = -\frac{f(u_0)}{\left(\frac{df(u)}{du}\right)_{u=u0}} \tag{2.2.5}$$

$f_{u0}{}'$ is derived from f_0 and u_0, the former being known and the latter is an initial guess. Eq. (2.2.5) is solved for the new value of Δu which is then checked for correctness with Eq. (2.2.3). If not correct, the current *u* value is used as u_0 for the next guess and the process repeats. This process is called Newton's method or the Newton-Raphson method [27].

2.2.2 - Dynamic

Dynamic problems are those for which inertial effects cannot be ignored. This means the acceleration and mass term in Eq. (2.2.1) cannot be ignored as before. The two types of dynamic analysis are generalized as Implicit and Explicit. The process for solving an implicit dynamic

problem is similar to nonlinear static ones, the difference being that the mass and inertia matrices are included and inverted over and over for as many time-steps are necessary to solve the time-dependent problem. An implicit technique is good for solving problems over large time scales where transient response is important and the system size is not prohibitively large. A large system makes inverting the *K* matrix a lengthy process and doing dozens of inversions dramatically effects solve time. Even so, this makes implicit dynamic the best option for solving large timescale problems because explicit may require a prohibitively small time increment.

The procedure for an explicit problem is quite different than implicit. The matrices are not inverted because values for velocity and acceleration are assumed at the beginning of analysis, so the equations of motion can be integrated at very small time increment to find the next position, velocity, and acceleration state for each node in the model. Abaqus uses central-difference time integration, which is very inexpensive numerically [28]. A problem can quickly become unsolvable if the stable time increment is too small compared to interaction time required in the problem.

Eq. (2.2.6) shows the minimum stable time increment is approximately a function of the minimum characteristic length and dilatational wave speed or speed of sound in the material. The minimum characteristic length L_{min} for simulations is the smallest element side length. Eq. (2.2.7) shows dilatational wave speed as a function of density ρ and Lame material constants λ and μ [29]. A progressive estimate of minimum stable time increment Δt is given by Eqn. (2.2.8) in terms of minimum element length, density, and Young's Modulus for a linear elastic isotropic material with Poisson's ratio of 1/3. Eqn. (2.2.8) shows that there is a limitation on how small elements can be as well as the density to Young's modulus ratio.

$$\Delta t \cong \frac{L_{min}}{c_d} \tag{2.2.6}$$

$$c_d = \sqrt{\frac{\lambda + 2\mu}{\rho}} \tag{2.2.7}$$

$$\Delta t \cong L_{min}\sqrt{\frac{2}{3}\frac{\rho}{E}} \tag{2.2.8}$$

2.3 - Element Selection

The two applicable element choices are brick and shell elements. The general rules for large displacement shell elements are 1) the shell thickness must be small compared to the next smallest characteristic length, 2) plane sections initially normal to the shell mid-surface remain normal after deformation, allowing shear deformation to be ignored, and 3) the stress component normal to the shell mid-surface is very small compared with other stress components, and can be ignored [30]. It makes sense to proceed using shell elements since honeycombs meant for energy absorption are typically shell-like structures [31]. Figure 2.3.1 shows how shear along shell thickness is very small compared to that along the shell plane. Abaqus offers several types of shell elements however S4R is chosen because it's formulated using reduced integration and has hourglass control. Reduced integration and hourglass control help prevent shear locking and improve convergence rates.

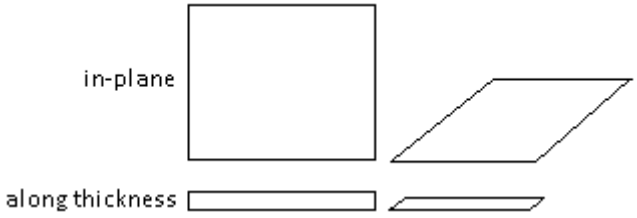

Figure 2.3.1 – Showing (top) in-plane and (bottom) thickness shears for a typical shell.

2.3.1 - Mesh Sensitivity Analysis

2.3.1.1 - Setup

It's necessary to find the element size that has a converged solution for the types of models in this work. A mesh sensitivity analysis is performed on a regular hexagonal cell to accomplish this. The geometry of the hexagon in Figure 2.3.2 is as follows: extruded height H of 15 mm, leg length L of 2.5 mm, and thickness t of 0.1 mm. The material is AISI 304 Stainless-Steel, having density ρ of 8060 kg/m^3, Young's Modulus E of 200 GPa, Poisson's Ratio v of 0.29. The material follows a linear hardening elastic-plastic scheme with yield data presented in Table 2.3.1.

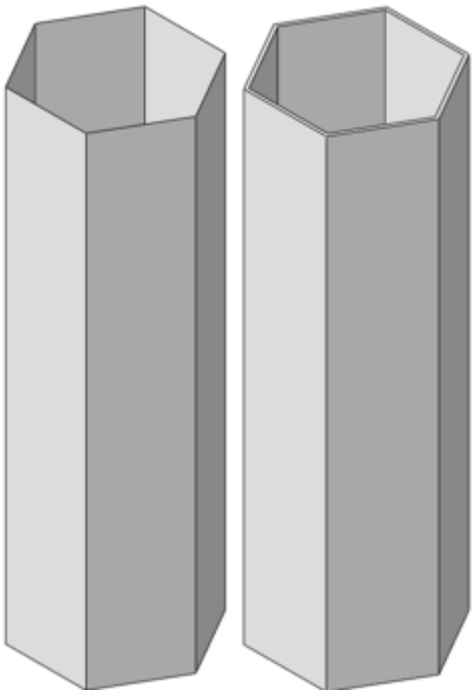

Figure 2.3.2 – Shell (left) and brick (right) hexagonal extrusion for mesh sensitivity analysis.

Table 2.3.1 – Hexagonal cell yield properties.

Yield Stress σ_y [MPa]	210	267	551
Plastic Strain ε_y	0	0.01	0.27

It should be noted that the results are heavily dependent on these properties but it isn't the value of the results that matters in a mesh sensitivity analysis, but their convergence to a singular quantitative value. Rigid frictionless surfaces are placed on the top and bottom of the hexagon to represent high yield materials, which are assumed to deform minimally during loading when compared to the honeycomb. The model assembly is shown in Figure 2.3.3. The bottom and top rigid surfaces are encastre and axially free to move, respectively. The nodes on the top and bottom surfaces of the hexagonal cell are pin tied to each respective rigid surface. These boundary conditions ensure the collapse mechanism is consistent across varying mesh densities.

It's important to apply loading such that progressive plastic failure is captured. For this, 60% strain is applied by moving the top piece axially at a prescribed velocity. A velocity of 50 m/s is chosen to simulate an abrupt impact on the structure. The velocity of an impactor is assumed to be zero at the instant contact is made, then reaches its impact value in a fraction of a second, decelerating from there on as the impact proceeds. This process is applied in Abaqus with an 'Amplitude' such that maximum velocity is reach 15 μs after contact. A total simulation time of

200 μs is required to achieve the desired strain at the prescribed velocity. Strain-rate sensitivity could easily be included with a subroutine but is intentionally left out for this analysis because it introduces deformation detail beyond that which is necessary for mesh convergence.

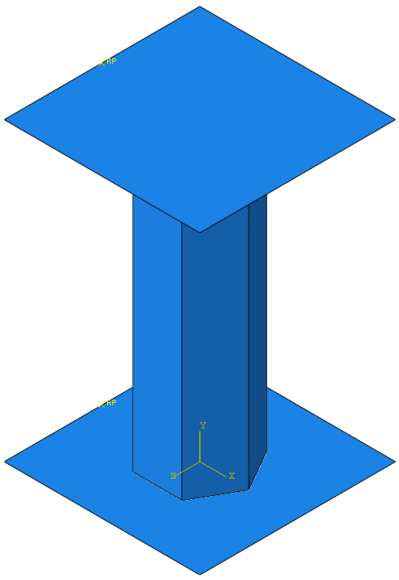

Figure 2.3.3 – Honeycomb assembly with rigid analytical top and bottom plates.

There are several ways to monitor the convergence progression across different mesh densities, the two most primarily applicable to buckling analysis can be defined by physical deformation or energy absorption. An example of monitoring physical deformation would be to watch how the failure mode changes with more elements, paying particular attention to the amplitude and frequency of buckling waves upon inception and progression of failure. Monitoring energy absorption for convergence is accomplished by either maximizing plastic dissipative or minimizing strain energy, respectively. This is further explained by looking at what happens to the hexagonal cell as it's crushed. The structure is deformed elastically until strain exceeds the yield value at 200 MPa, which is when plastic deformation begins. Plastic deformation is dependent on the level of detail available in the geometry during collapse—detail prescribed solely by the mesh. In short, the amount of plastic deformation allowed to accumulate over the time it takes to reach 60% strain will become maximized as mesh density increases. Conversely, strain energy is a result of the structures inability to reach yield stress or is present after yield stress as a residual strain energy. We then expect strain energy to become minimized as the mesh sensitivity analysis approaches a converged solution. Monitoring energy is finite and tabular compared to

the subjectivity introduced by visually inspecting buckling modes, therefore energy convergence is the chosen method. Since strain and plastic energies are conversely related for this type of analysis, either are sufficient. Accordingly, strain energy is chosen to be monitored and minimized for the proceedings.

2.3.1.2 - Results

Mesh densities are defined by prescribing elements along in-plane cell wall length L and extrusion height H in the format $L_{elements}$ x $H_{elements}$. As an example, a 5x10 mesh would result in five elements along each cell wall and ten along the extrusion height. *Figure 2.3.4* shows low and high density meshes deforming over 50 *μs*. Vastly different failure modes are seen depending on mesh density. Figure 2.3.5 shows the strain energy of the hexagonal honeycomb converging towards a minimized value over several density iterations, the last three densities most nearly converged. From Figure 2.3.6, it is clear strain energy is converged at density 60x200. Using the hexagons aforementioned geometry, we find the global element dimensions of insensitive mesh are 41.7 μm and 75 μm. A similar analysis [12] using global mesh size instead of leg length and extrusion height found results became insensitive to mesh density at global element size *t/2*, or 50 μm for our case—where *t* is wall thickness. This mesh density was implemented and the results are compared in Figure 2.3.5–Figure 2.3.6. Very good agreement is found with the *t/2* global element size approximation.

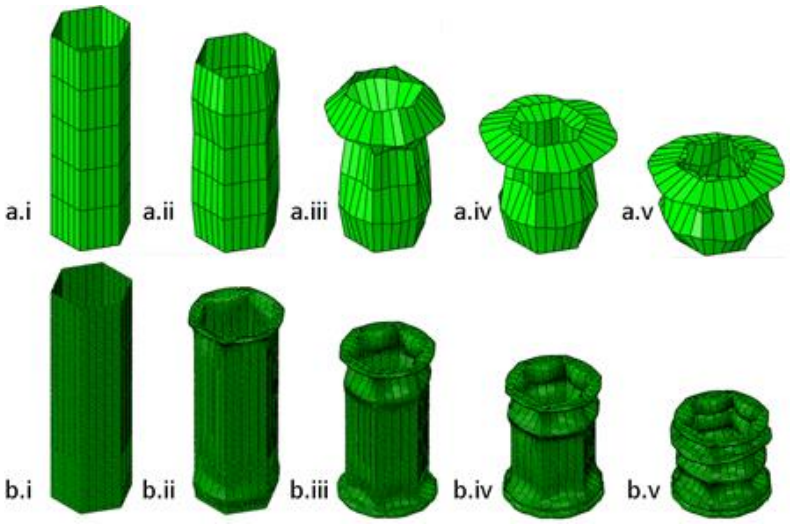

Figure 2.3.4 – Shell honeycomb failure progression at interval 50 μs for a) 5x5 and b) 5x100

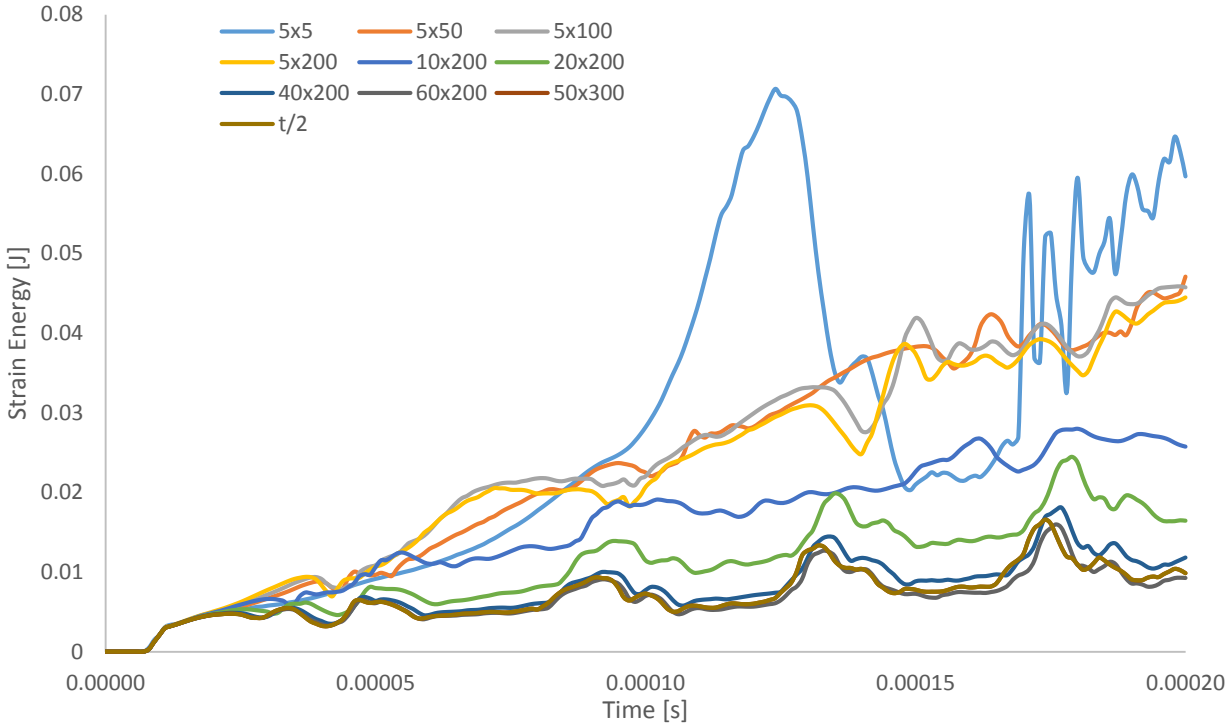

Figure 2.3.5 – Strain energy vs. time, showing convergence across multiple mesh densities.

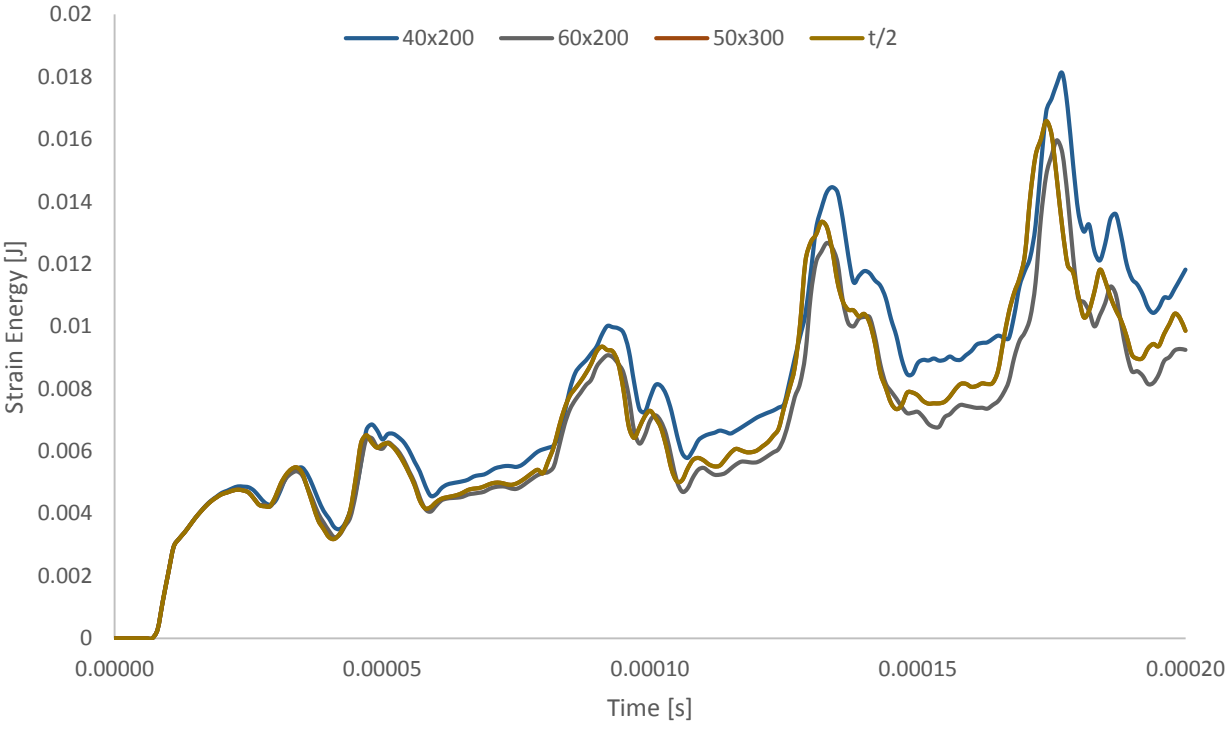

Figure 2.3.6 – Converged strain energy at specified densities.

A way to check the accuracy of results in Abaqus is to compare real to artificial energy. Artificial energies are introduced to increase the convergence rate of results in Abaqus, speeding up overall solve time. Results are admissible provided artificial energies are consistently below a threshold value of about 5% of total energy. Evaluating artificial contributions can be done by pulling resultant strain, plastic dissipation, viscous, and artificial energy terms. Viscous energy is generated due to assigning a bulk viscosity to the material as an aid in drowning out the noise of solution fluctuations [28]. Artificial energy also acts to suppress unnecessary noise in the solution. Bulk viscosity and hourglass control have a hand in solution convergence for the Explicit solver however their default values can be adjusted if an eventual solution has more than marginal error. For our primarily plastic dissipative model, error can be quantified by adding viscous and artificial energies and dividing their sum by that of strain and plastic dissipative energies. All four of these energies continue to rise with increasing strain due to constant kinetic energy input into the system as the top analytical piece crushes the honeycomb. It's reasonable then to take the error at the last time step, when it should be largest. Viscous, artificial, strain, and plastic dissipative energies are 8.48 mJ, 48.2 mJ, 9.86 mJ, and 2.52 J, respectively. This leads to only 2.1% error in results, which is below the 5% threshold value.

2.4 - Benchmark

2.4.1 - Setup

In order to gauge the accuracy of the current modeling technique, existing experimental and numerical results are attempted to be replicated. The paper chosen is '*Dynamic Compressive Response of Stainless-Steel Square Honeycombs'* by Radford *et al*. The properties in the following table are used [12]. The rate sensitivity of stainless-steel [12] is also considered by employing a yield stress ratio sub-option in Abaqus. Rigid surfaces are tied to the top and bottom faces of the honeycomb such that no rotations occur. S4R elements with default hourglass and bulk viscosity are used. It's important to note that these boundary conditions and material models cannot match exactly those from the paper due to subjective interpretation. The paper uses heights of 6 mm and 30 mm, the taller specimen being chosen to correlate results with. Cell size L of 6 mm and wall thickness b of 0.3 mm match those in the paper and can be found on Table 2.3.1. Velocities of 20 ms^{-1}, 50 ms^{-1}, and 240 ms^{-1} are used to match those in the paper.

Table 2.4.1 – AISI type 304 stainless-steel.

ρ [kg/m^3]	E [GPa]	σ_y [GPa]	σ_U [GPa]	ν	H [m]	b [m]	L [m]
8060	210	0.3	0.7	0.3	0.030	0.0003	0.006

Table 2.4.2 – Stainless-steel rate sensitivity data.

σ_y/σ_s Ratio R	1	1.06	1.12	1.17	1.27	1.45	1.63
Strain Rate $\dot{\varepsilon}$	0	1_E^{-2}	1	1_E^{1}	1_E^{2}	1_E^{3}	1_E^{4}

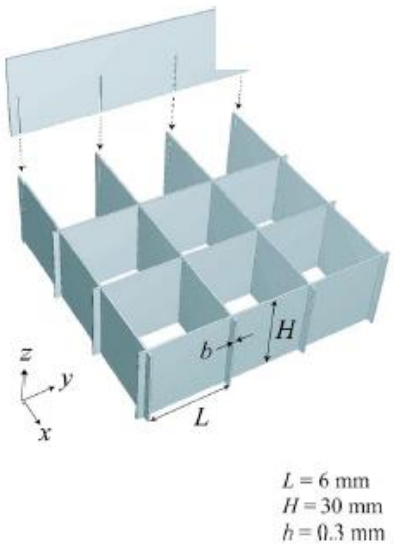

Figure 2.4.1 – Benchmark geometry [12]

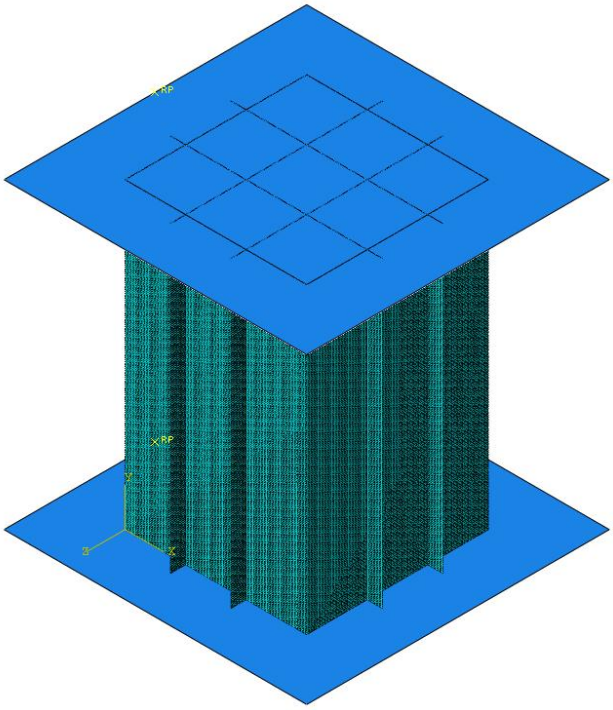

Figure 2.4.2 – Meshed 30 mm specimen with top and bottom rigid surfaces.

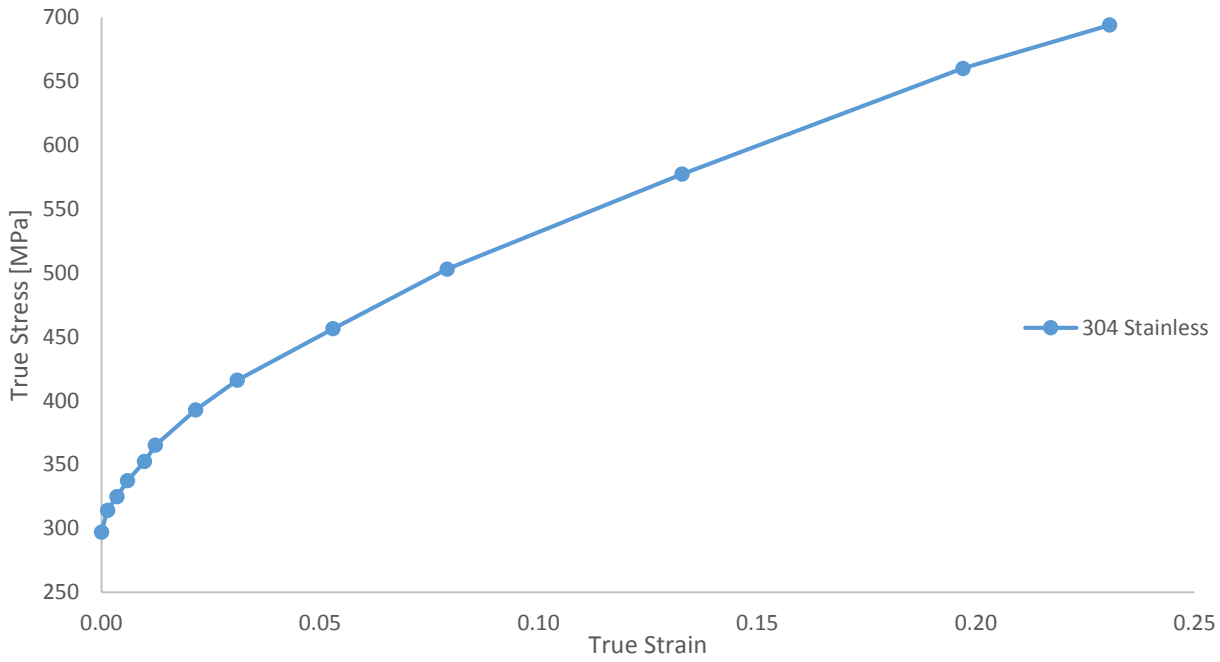

Figure 2.4.3 – Quasi-static plastic stress vs. true strain relation employed during analysis [12].

2.4.2 - Results

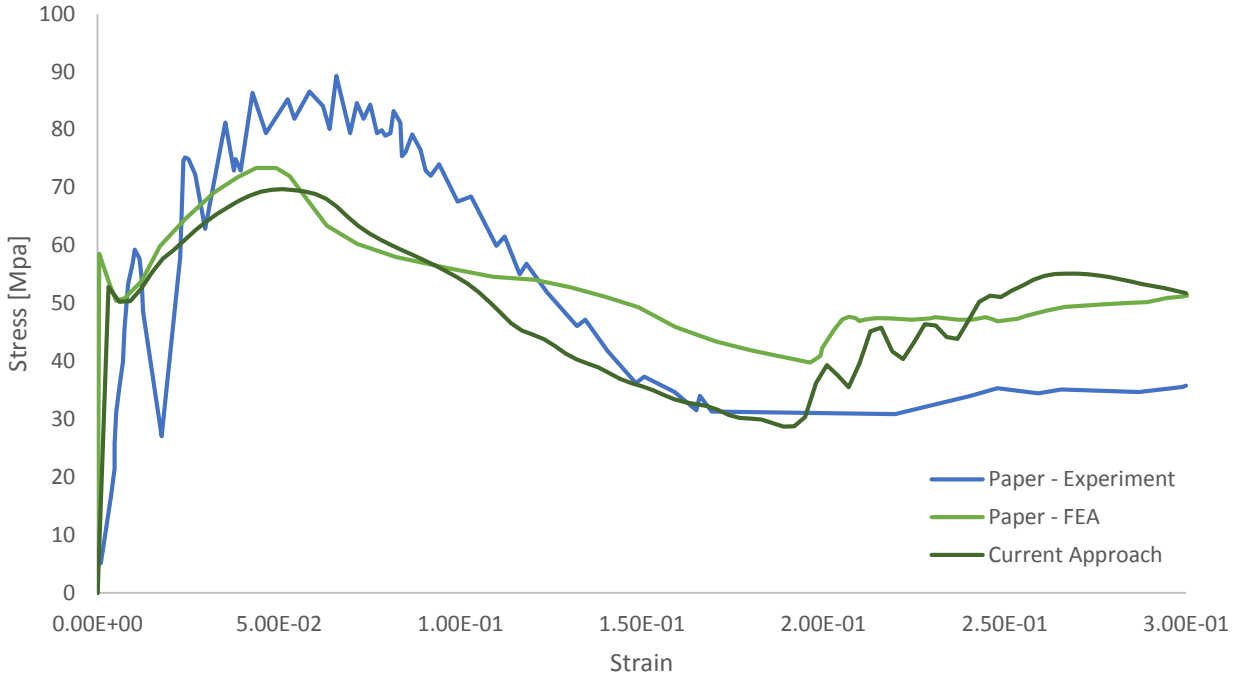

Figure 2.4.4 – Stress-strain response for 20 ms^{-1} loading.

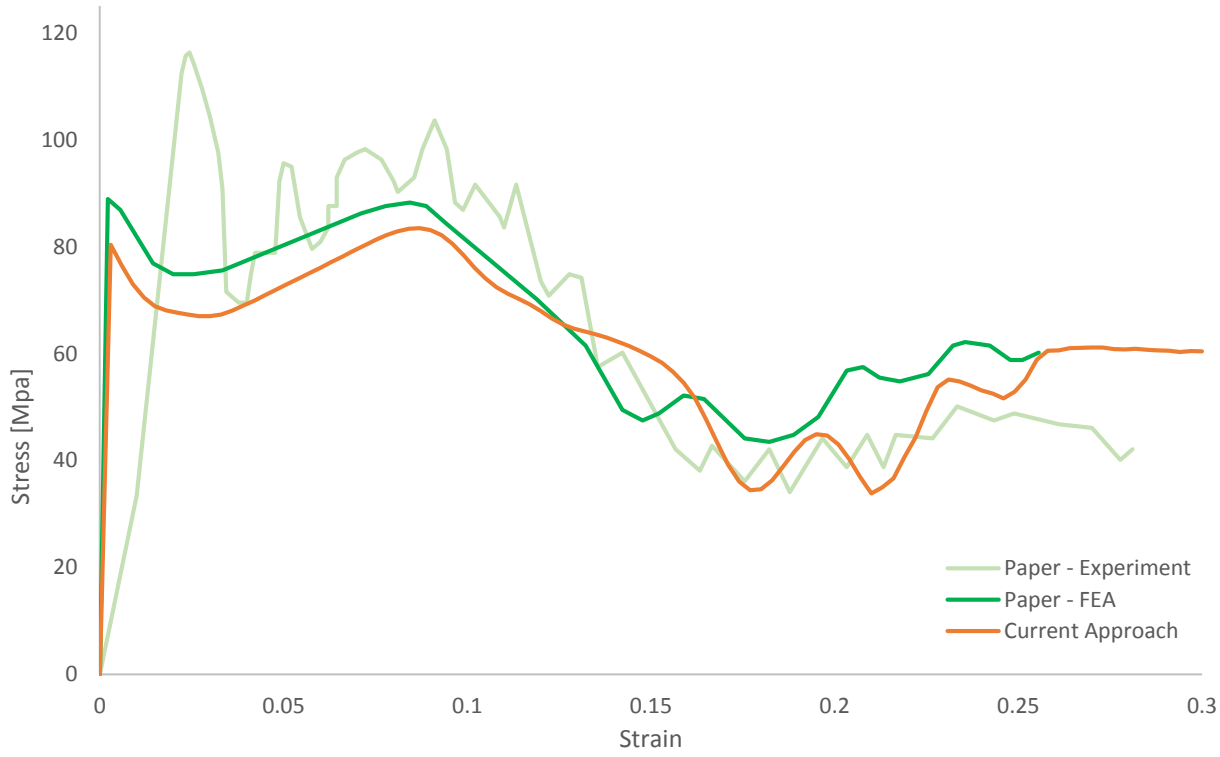

Figure 2.4.5 – Stress-strain response for 50 ms^{-1} loading.

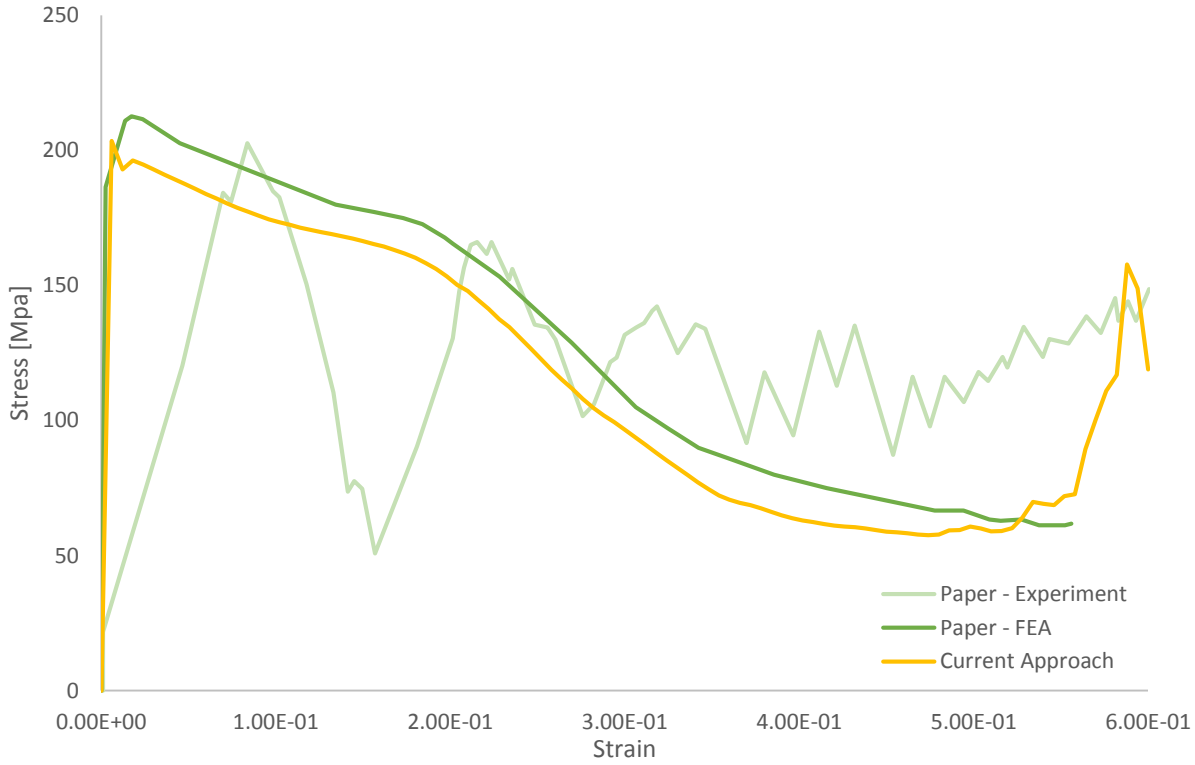

Figure 2.4.6 – Stress-strain response for 240 ms^{-1} loading.

Figure 2.4.4 – Figure 2.4.6 show that the approach presented here, as with that in the published paper, has accuracy dependent on loading rate. Figure 2.4.4 shows the current approach matches peak stress very well for the 20 ms^{-1} case but deviates from the paper results as strain increases. Figure 2.4.5 shows a good match between the combination of experimental and computational paper results for the 50 ms^{-1} case. Figure 2.4.6 shows a good match with paper computational results for the 240 ms^{-1} case, deviating from experimental results in the same manner as the paper computational method.

It's important to note one fundamental difference between the present approach and that of the paper; this approach doesn't introduce imperfections into the model but the paper uses low and high-order modes of perturbation to acquire an initial 'imperfect' state, then scales these results and uses the subsequent shape as the initial impact state. This approach was intentionally ignored because their results indicate the initial imperfections, regardless of mode, had negligible effect on the stress-strain response [12]. It can be concluded that the modeling technique outlined by this chapter should produce results with the accuracy and consistency necessary for the proposed comparative topological analysis.

Chapter 3 - Geometric Comparison

3.1 - Introduction

The intent of this chapter is to provide a baseline for future analysis. Square and triangular cell constructions are chosen to be compared against regular hexagonal. Each topology is of 4x4 cell number with no periodic boundary conditions. This is done to mimic the experimental case, where a Split-Hopkinson bar will likely dictate the sample size be smaller than 1 in^2. Accordingly, employing periodicity would not give results comparable to current dynamic loading processes. The comparison is done at relative density $\bar{\rho}$ of 20%.

3.2 - External Constraints

Similar experimental research has been performed using cell heights as little as 6 mm [12] and as large as 150 mm [9]. A fixed cell height of 100 mm is chosen because it's on the larger end of the spectrum, allowing for greater overall energy absorption. It's important to choose a realistic cell size L, to do so means first considering a realistic out-of-plane aspect ratio *H/L*. Aspect ratio has been shown to effect resultant mean crush strength [7]. Since H has been established as constant at 100 mm, L must vary when t is held constant in order to maintain the correct $\bar{\rho}$ value. The results of [7] were obtained over a range of $1 \leq H/L \leq 5$. Inherently, the range chosen for this paper is $2.5 \leq H/L \leq 5$. This forces the cell size to vary within the bounds of 20 mm $\leq L \leq$ 30 mm. The above procedure aims to minimize experimental results dependence on aspect ratio. As such, impactor velocity must be chosen with equal care.

Strain rate has been shown to significantly affect the strength of nickel based honeycombs [14]. Material sensitivity can be removed from the proceeding comparisons if steps are taken to ensure its contribution is negligible. Metals tend to be relatively insensitive to strain rate when applied values are below 10^3 s^{-1} [26]. Any loading resulting in strain rates below this value are then acceptable. A realistic impact loading rate can be found by noting the speed limit on the New York State thruway, which is 65 mph or 29 m/s. A value of 30 m/s combined with 100 mm cell height gives a strain rate of $3E^2$ s^{-1}, which is safely beneath the threshold sensitivity value. The loading rate 30 m/s is chosen to represent a scenario where energy absorbance is desired for a specific type of impact. How a 4x4 cell is defined will affect the response of the honeycomb. Square and rectangular geometries have their outer boundary with thickness t. This is chosen to

be the case because having continuous linkage on the perimeter will ensure the response is of the strongest bonded 4x4 cell. Any other cut will have multiple free legs, contributing less to overall stiffness then when they are bonded on the perimeter. This is also a realistic depiction of the physical system, since trimming the legs outside the boundary would be easy and result in the best honeycomb per allowed area.

The hexagonal 4x4 cell is made with the same bounding connectivity in mind. It's worth mentioning that the hexagonal geometry would be more challenging to implement experimentally because the top and bottom outermost hexagons have their boundary legs with *t/2*—which would be difficult to make as thicknesses approach 1 mm. Figure 3.3.1 shows each honeycomb as described.

3.3 - Boundary Conditions

Each honeycomb is bonded to rigid top and bottom plates using the tie constraint such that in-plane displacement is fixed while axial displacement and rotations are allowed—otherwise known as a pin tie. This represents a physical system initially bonded at the top and bottom but not well enough to withstand significant dynamic loading stress, and where friction between the honeycomb and top/bottom surfaces restrains displacement but allows rotation. General contact between all surfaces is introduced as hard and frictionless. Both of these conditions are admissibly found in literature [12]. Velocity of the top plate is 30 m/s in the compressive axial direction as discussed in the previous section.

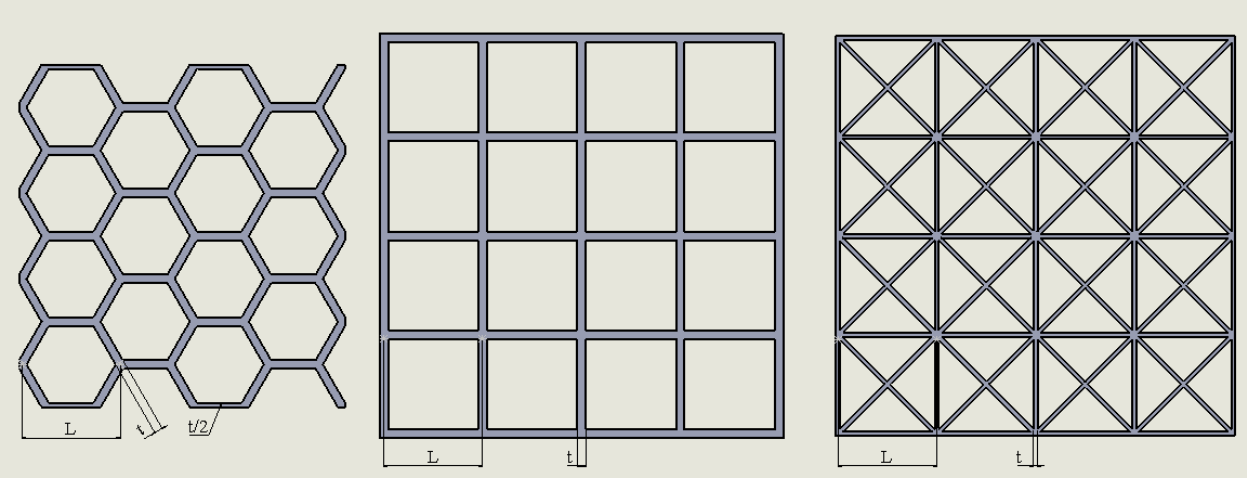

Figure 3.3.1 – Hexagonal, square, and triangular 4x4 honeycombs, $\bar{\rho}$ of 20% at L of 20mm with corresponding thickness t.

3.4 - Procedure

Relative density is directly proportional to area when the geometry is extruded. Such proportionality is used to derive Eqn. (3.4.1), which relates relative density, cell length, and wall thickness for an *n* x *n* square geometry. A_E is empty cell area while A_T is the total cross-sectional area occupied by the *n* x *n* model. Cell size varies while relative density is constant at 20%. Three *L* values are chosen to span the range mentioned above—corresponding *t* values and overall model size are found by using 4 for *n*, relative density of 0.20, and the desired cell size to solve Eq. (3.4.1) for thickness. The results for 20, 25, and 30 cell size are given in Table 3.4.1. The process formulating the geometry for triangular and hexagonal honeycombs is exactly the same as for square honeycombs—Equations (3.4.2) and (3.4.3) are for triangular and hexagonal topology, respectively.

$$\bar{\rho} = 1 - \frac{A_E}{A_T} = 1 - \left[\frac{n(L-t)}{nL+t}\right]^2 \tag{3.4.1}$$

$$\bar{\rho} = 1 - \frac{A_E}{A_T} = 1 - \left[\frac{n(L-t\left(1+\sqrt{2}\right))}{(nL+t)}\right]^2 \tag{3.4.2}$$

$$\bar{\rho} = 1 - \frac{Ae}{A_T} = 1 - \frac{\left(L\sqrt{3}-2t\right)^2(3n+1)}{L(9nL+4t\sqrt{3}+3L)} \tag{3.4.3}$$

Table 3.4.1 – Fixed cell heights and inherited parameters for square honeycombs.

L [mm]	20	25	30
B [mm]	81.73	102.16	122.59
t [mm]	1.73	2.16	2.59

Table 3.4.2 – Fixed cell heights and inherited parameters for triangular honeycombs.

L [mm]	20	25	30
B [mm]	80.80	101.00	121.20
t [mm]	0.80	1.00	1.20

Table 3.4.3 – Fixed cell heights and inherited parameters for hexagonal honeycombs.

L [mm]	20	25	30
B_1 [mm]	65.98	82.49	98.98
B_2 [mm]	69.28	86.60	103.9
t [mm]	1.71	2.14	2.57

3.5 - Results

3.5.1 - Mass Normalizing

The artificial energy is found to be less than 3% of combined plastic and strain energy for each respective cell size, ensuring error hasn't snowballed during the simulation. Mesh sensitivity analysis similar to that performed in the previous section confirmed elements of size *t/2* managed to give a converged solution. All proceeding results also fall under the threshold artificial percentage unless otherwise mentioned. Figure 3.5.1 shows that energy absorbed increases with cell size, Figure 3.5.2 indicating the relationship is very linear. This is due to the fact that the overall amount of honeycomb material increases with cell size if relative density is held constant. Imagine two 4x4 honeycombs; one is small enough to sit on top of a desk while the other spans a room. While they both may have equal relative densities if *nxn* is the same, the overall amount of honeycomb material composing each 4x4 is vastly different. Such differences must be eliminated to compare honeycomb geometry, so normalizing all geometries with respect to one is essential. This process is shown in Table 3.5.1, where the smallest area A_0 is chosen to be the normalizing parameter. This happens to be the area of the smallest square honeycomb. It's clear from Figure 3.5.3 that there is little variation in energy absorption across cell sizes within a close aspect ratio range once their relative masses are considered. This leaves the amount of energy absorbed after 40% strain as just over 20 KJ. Results for triangular and hexagonal honeycombs indicate the same type of behavior found in Figure 3.5.3.

Table 3.5.1 – Normalized area of square honeycombs.

	Square		
	20 mm	25 mm	30 mm
A [mm^2]	1339.11	2090.02	3007.38
A/A0	1.00	1.56	2.25

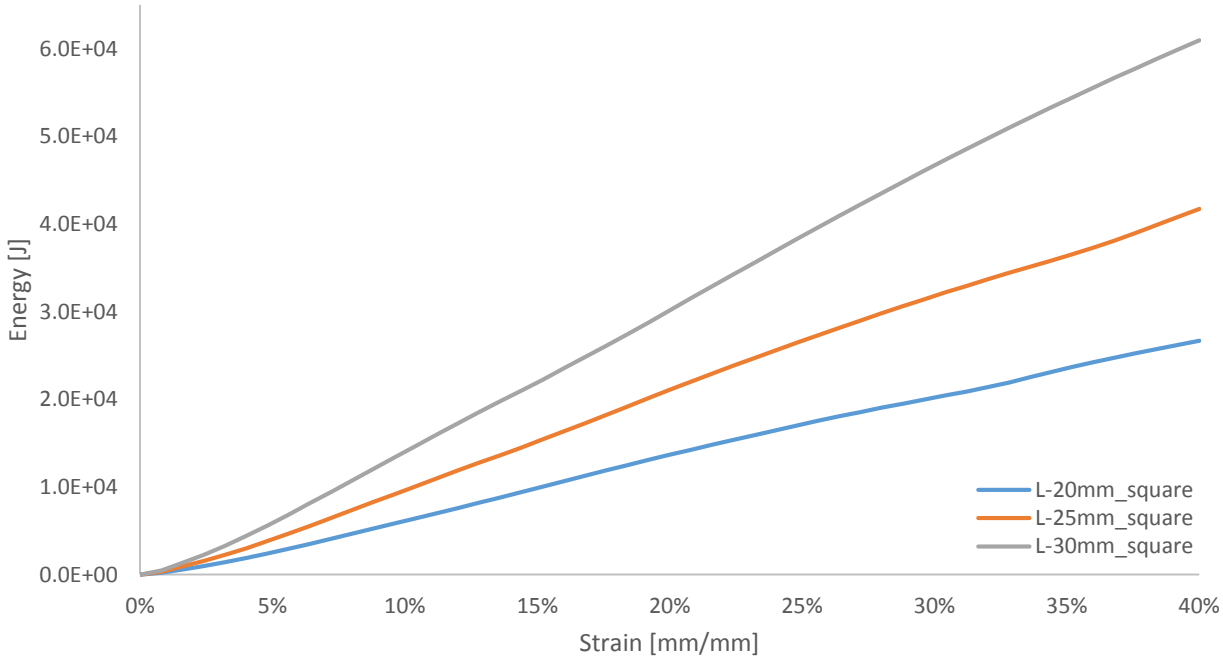

Figure 3.5.1 – Energy absorbed by square honeycombs up to 40% strain.

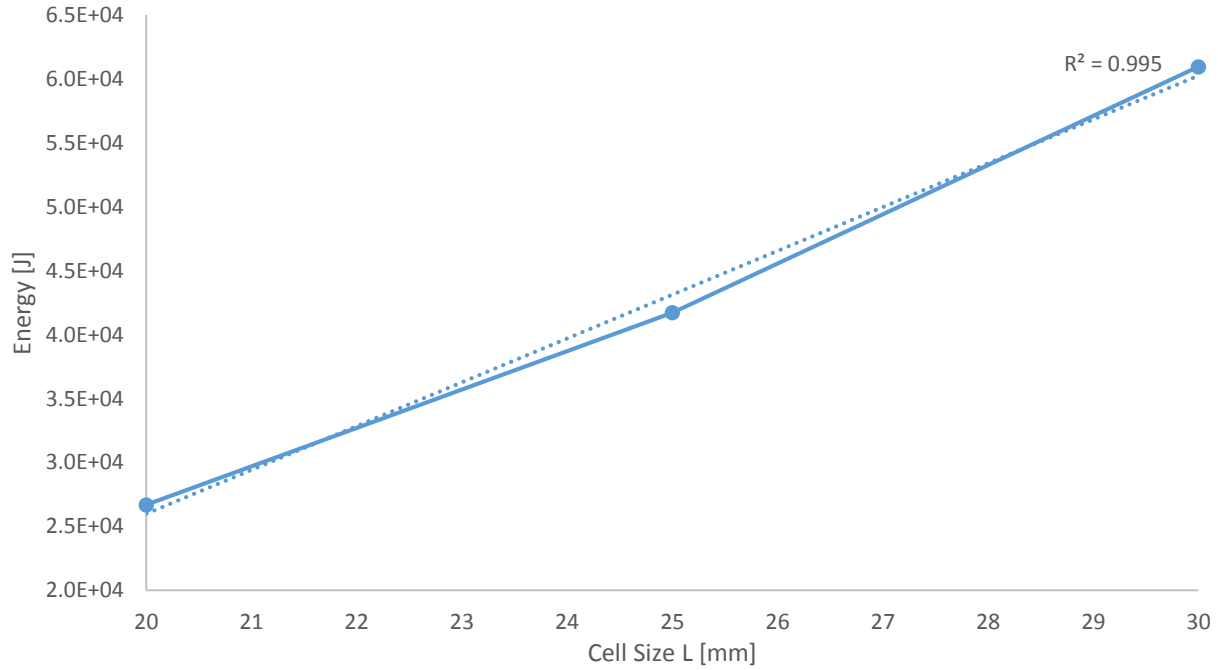

Figure 3.5.2 – Total energy absorbed by square honeycombs, indicating a strong linear dependence on cell size.

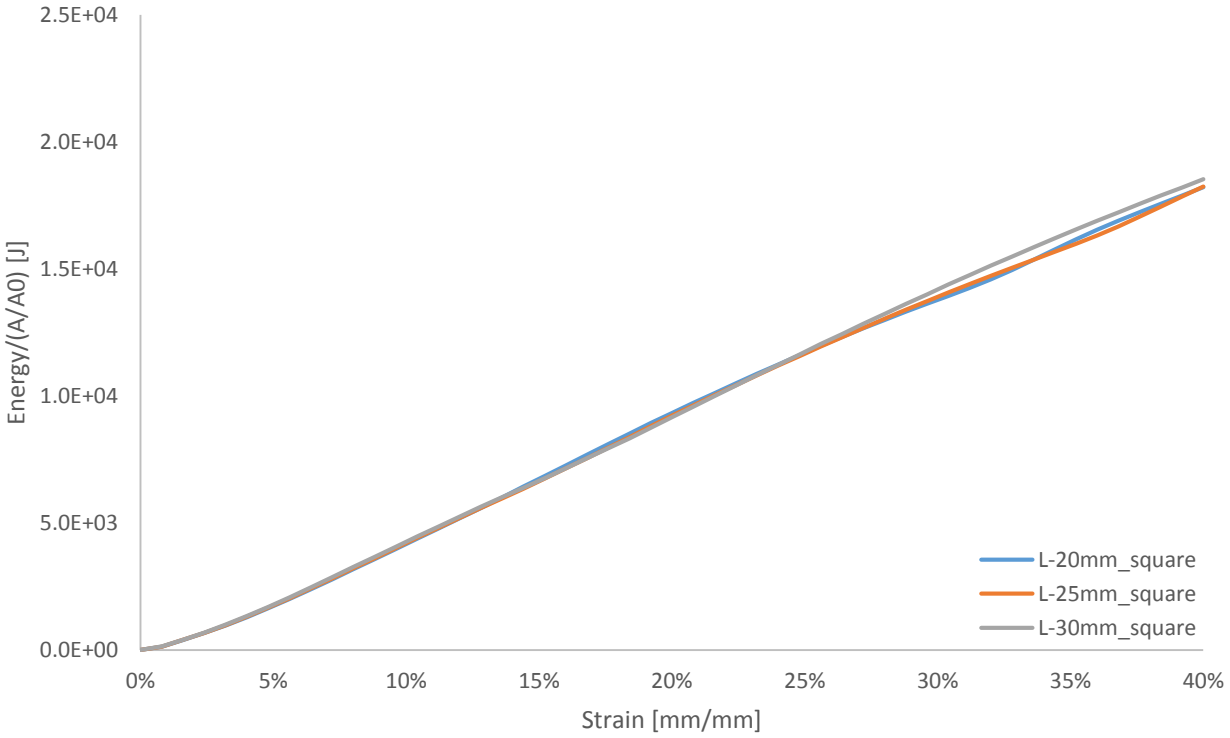

Figure 3.5.3 – Normalized energy absorbed by square honeycombs up to 40% strain.

3.5.2 - Square, Triangular, Hexagonal Honeycombs

Table 3.5.2 is used to find the area or mass contribution factors across all geometries with respect to the smallest area—which is the 20 mm hexagon. Figure 3.5.7 shows that all geometries have consistent specific energy absorption across similar cell sizes and that hexagonal structure absorbs the most energy.

Table 3.5.2 – Normalized area of honeycombs.

	Hexagon			Square			Triangle		
	20mm	25mm	30mm	20mm	25mm	30mm	20mm	25mm	30mm
A	914.3	1429	2057	1339	2090	3007	1305	2039	2936
A/A0	1.00	1.56	2.25	1.46	2.29	3.29	1.43	2.23	3.21

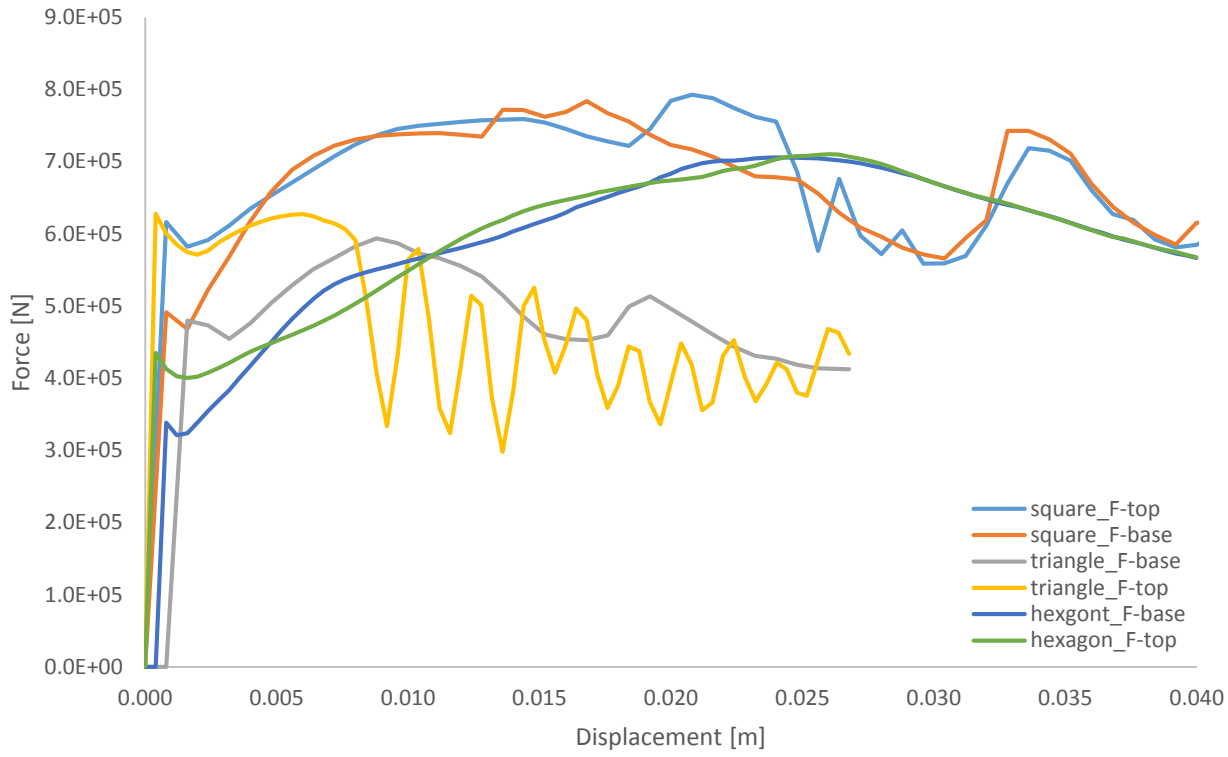

Figure 3.5.4 – Force-displacement plots for honeycombs of 20 mm cell size.

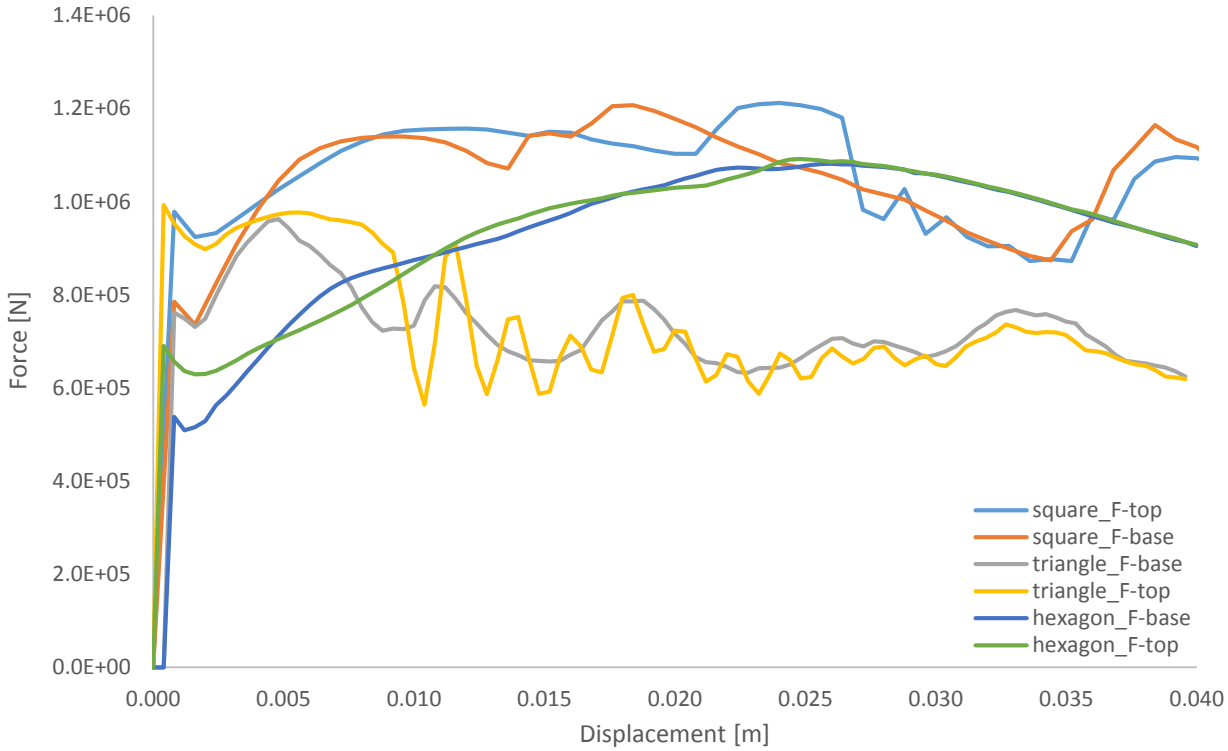

Figure 3.5.5 – Force-displacement plots for honeycombs of 25 mm cell size.

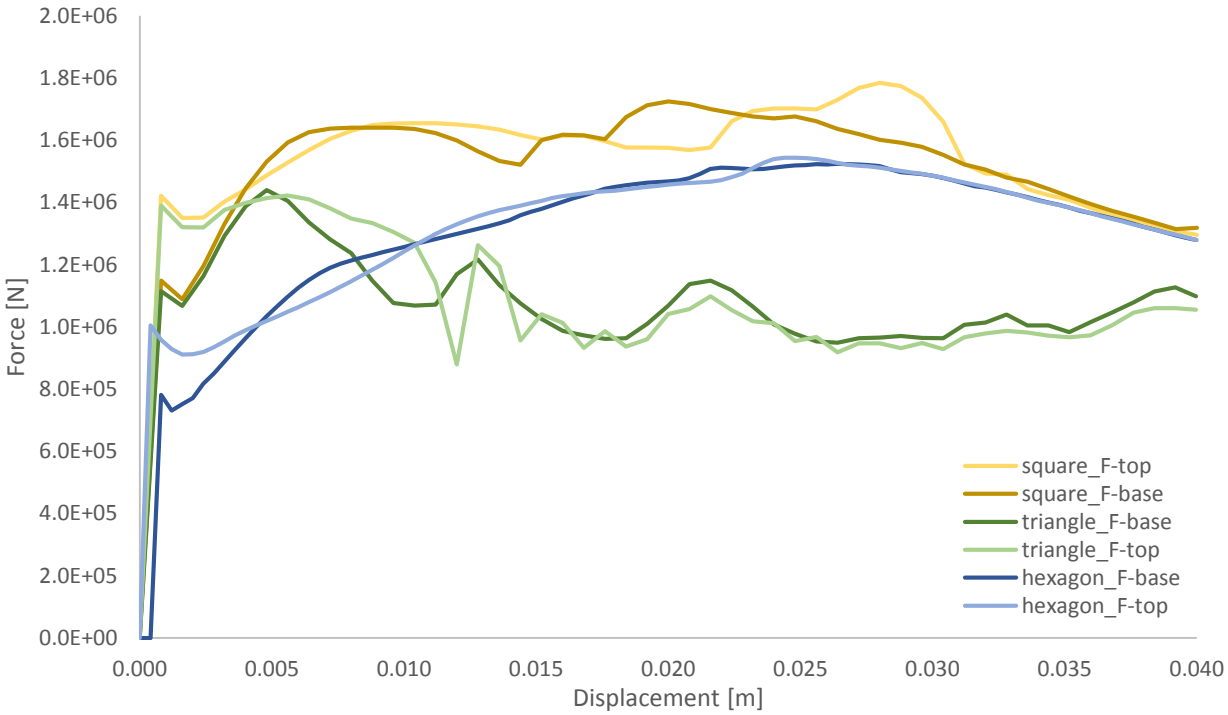

Figure 3.5.6 – Force-displacement plots for honeycombs of 30 mm cell size.

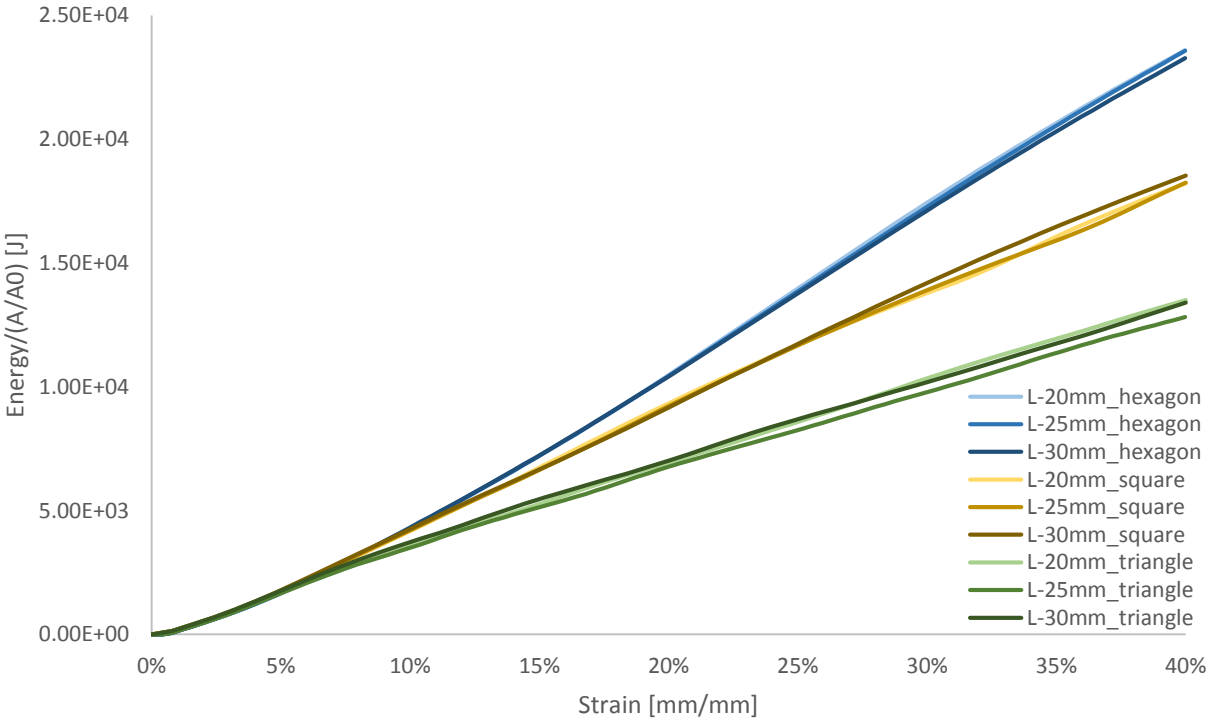

Figure 3.5.7 – Normalized energy absorbed by honeycombs up to 40% strain.

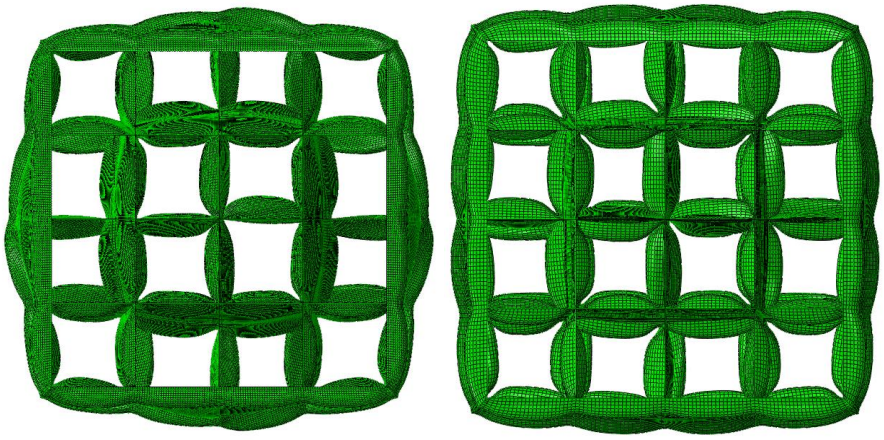

Figure 3.5.8 – Top view of end state for square 4x4 structure with (left) L = 30mm and (right) L = 20mm.

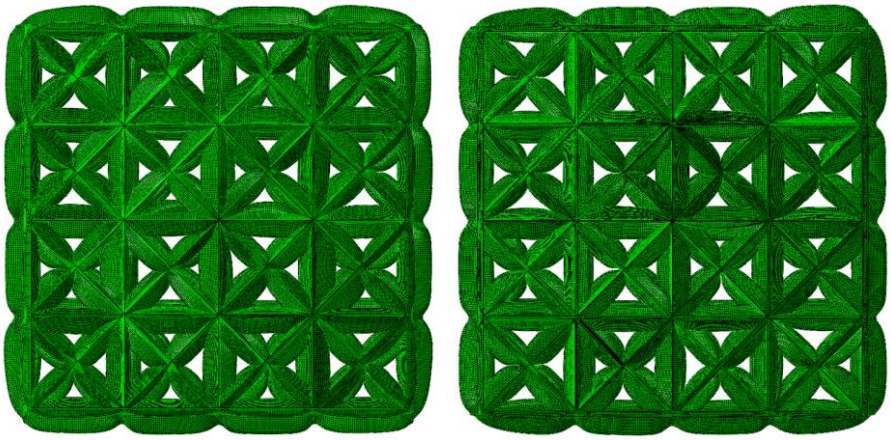

Figure 3.5.9 – Top view of end state for triangular 4x4 structure with (left) L = 30mm and (right) L = 20mm.

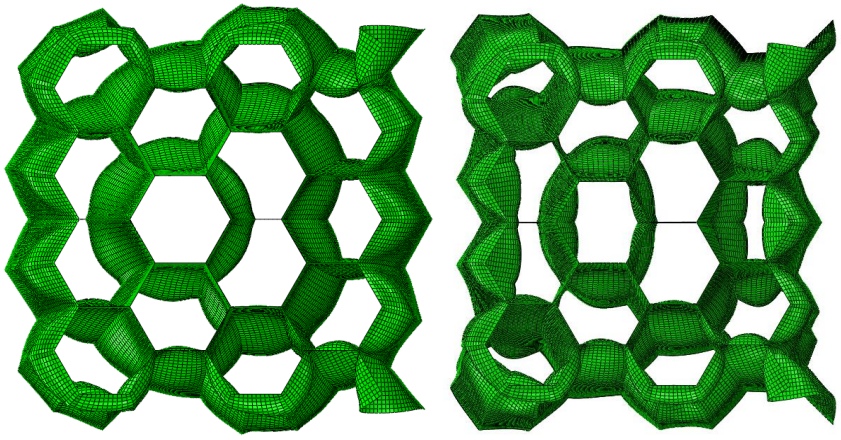

Figure 3.5.10 – Top view of end state for hexagonal 4x4 structure with (left) L = 30mm and (right) L = 20mm.

3.6 - Discussion

Figure 3.5.1 and Figure 3.5.2 shows that energy absorbed by square topology increases with cell size but as previously mentioned, this is only because the overall honeycomb size and mass are increasing. Figure 3.5.3 shows that energy absorbed is the same across cell sizes once normalized by the extra mass present in the system. Figure 3.5.7 confirms the same trend for triangular and hexagonal honeycombs. Figure 3.5.4–Figure 3.5.6 show there is a mismatch between top and bottom plate forces during most of the loading for all topologies. Hexagonal topology consistently has the least mismatch amplitude and reaches dynamic equilibrium the fastest. The response of 20 mm triangular cell structure was not completed beyond 26 % strain because the minimum time-step required became prohibitively small. Figure 3.5.7 shows the topological order of specific energy absorbed from highest to lowest is hexagonal, square, and then triangular. Taking the average specific energy absorbed by each cell structure, hexagonal geometry absorbs 28 % and 77 % more energy than square and triangular, respectively. Figure 3.5.8–Figure 3.5.10 show no significant difference in overall deformation behavior between different cell sizes of the same topology or between different topologies. This chapter has shown that hexagonal cell structure is capable of absorbing more energy per unit mass when compared to square or triangular structures of the same relative density. It's important to investigate how parameters like connectivity and aspect ratio can affect energy absorbance.

Chapter 4 - Connectivity and Thickness

4.1 - Introduction

The previous chapter showed: The same geometry with similar cell size has exactly the same energy absorbing capability once normalized by relative mass; and There is a dependence on the combination of thickness and connectivity. This chapter will use the results from the previous chapter to investigate the thickness and connectivity dependence.

4.2 - External Constraints

All proceeding geometries will have the same mass (area), which is found under the assumption that relative density is 20%. There will be at least four simulations for each geometry: a 4x4, 3x3, 2x2, and 1x1. Unlike the previous chapter, where the bounding area was inherited from cell size, this chapter uses a consistent boundary area as well as occupied area. Triangular geometry is chosen to be the prescriber of this condition and is therefore examined first. It's important to keep loading consistent throughout cell structure changes so that results are comparable. Accordingly, applied velocity, contact, and tie conditions are the same as in the previous chapter. Extrusion length of the structures is also the same.

4.2.1 - Procedure, Triangular Honeycomb

The first simulation is a 4x4 structure, meaning n is 4 in the previous triangle relation. Selecting a thickness of 1.5 mm means the equation can be solved for cell size—which is 37.48 mm. Knowing L and t, the base cell length B is found to be 151.42 mm. Boundary area remains the same for all simulations in this chapter, which means dimension B will remain the same for square and triangular geometries. Eqn. (4.2.1) is introduced to solve the previous chapter's relative density equation for two variables. B is constant and n corresponds to which nxn cell structure is being considered. Inserting this equation into the previous relative density equation for triangular honeycombs of $1 \leq n \leq 4$ outputs the corresponding L and t values seen in Table 4.2.1.

$$B = nL + t \tag{4.2.1}$$

Table 4.2.1 – Geometry parameters for triangular honeycombs.

nxn	4x4	3x3	2x2	1x1
C	208	120	56	16
L [mm]	37.48	49.83	74.34	146.73
t [mm]	1.50	1.94	2.74	4.68
t/L x10^3	40.02	38.92	36.89	31.91

Connectivity is introduced as *C* to quantify the connectedness of each structure. Figure 4.2.1 shows a 2x2 triangle, composed of thirteen joints. Corner joints J1, J3, J11, J13 have three legs, middle boundary joints J2, J6, J8, J12 have five legs, first-order cross-joints J4, J5, J9, J10 have four legs, and second-order cross-joint J7 has eight legs. Connectivity *C* is found by multiplying each joint by the number of legs tied to it. The total connectivity of the structure would then be equal to the sum of joint connectivities as seen in the equation below. J_i corresponds to the total number of type *i* joint and K_i is the number of legs in that type of joint. Finding *C* for the 2x2 triangle is performed below. The first term corresponds to corner joints, the second is middle boundary joints, third being first-order cross-joints, and fourth being the second-order cross-joint. Although *K* and *J* will vary with geometry and *n*, the process for calculating connectivity is always the same.

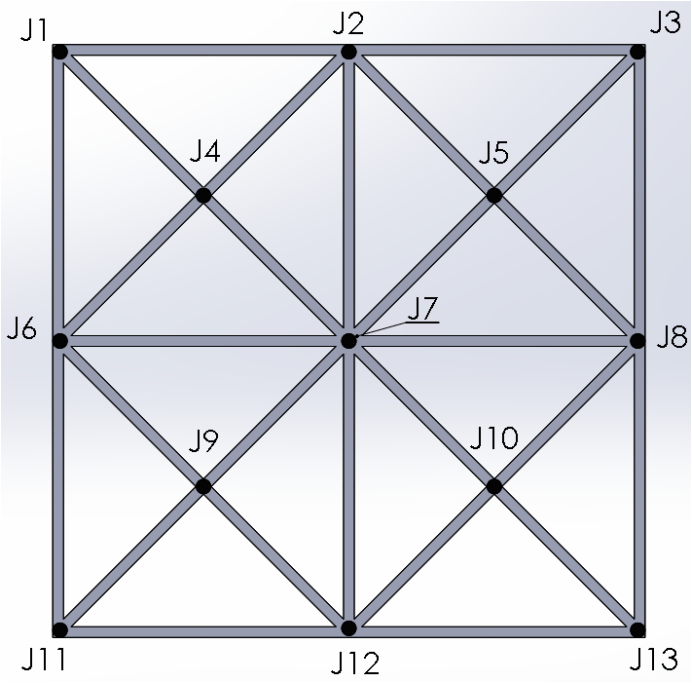

Figure 4.2.1 – Joints for connectivity of 2x2 triangle.

$$C = \sum_{i=1}^{n} K_i J_i \tag{4.2.2}$$

$$C = \sum_{i=1}^{n} K_i J_i = K_1 J_1 + K_2 J_2 + K_3 J_3 + K_4 J_4 \tag{4.2.3}$$
$$= 3 * 4 + 5 * 4 + 4 * 4 + 8 * 1 = 56$$

4.2.2 - Square Honeycomb

The same procedure is used for square honeycombs with the exception that the triangular relative density equation is used and solved for $1 \leq n \leq 6$. A larger range is used to be sure a recognizable pattern evolves.

Table 4.2.2 – Geometry parameters for square honeycombs.

nxn	6x6	5x5	4x4	3x3	2x2	1x1
C	168	120	80	48	24	8
L [mm]	24.86	29.75	37.05	49.14	73.04	143.42
t [mm]	2.28	2.66	3.20	4.00	5.33	7.99
t/L x10^3	91.86	89.55	56.29	81.33	72.95	55.73

4.2.3 - Hexagonal Honeycomb

We will use the hexagonal relative density equation from the previous chapter but cannot use Eq. (4.2.1) because base and height dimensions must change in response to the *nxn* structure being considered. As mentioned above, bounding area must remain the same—so Eqn. (4.2.4) is developed predicated on consistent area throughout *nxn* structures. A_T is constant and equal to B^2 of square/triangular geometry. Since *n* corresponds to the *nxn* structure being considered, we can solve the two equations to obtain *L* and *t* values as seen on Table 4.2.3.

$$A_T = nL\frac{\sqrt{3}}{24}\left(9nL + 4t\sqrt{3} + 3L\right) \tag{4.2.4}$$

Table 4.2.3 – Geometry parameters for hexagonal honeycombs.

nxn	6x6	5x5	4x4	3x3	2x2	1x1
C	244	176	114	70	32	12
L [mm]	30.32	36.16	44.79	58.84	85.83	159.30
t [mm]	2.65	3.13	3.83	4.94	6.96	11.93
t/L x10^3	87.32	86.60	85.56	83.96	81.13	74.87
B [mm]	145.53	146.44	147.77	149.96	154.22	166.18
H [mm]	157.53	156.56	155.15	152.88	148.66	137.96

Figure 4.2.2 shows all the cell structures used for analysis. It's easy to confirm visually that external boundary area is the same throughout all the triangular and square structures. The hexagonal structures show a boundary aspect ratio change progressing from 6x6 to 1x1 structures, which can be verified on Table 4.2.3. The boundary area is confirmed constant and equal to the triangular/square geometries in each *nxn* case by multiplying *B* and *H*.

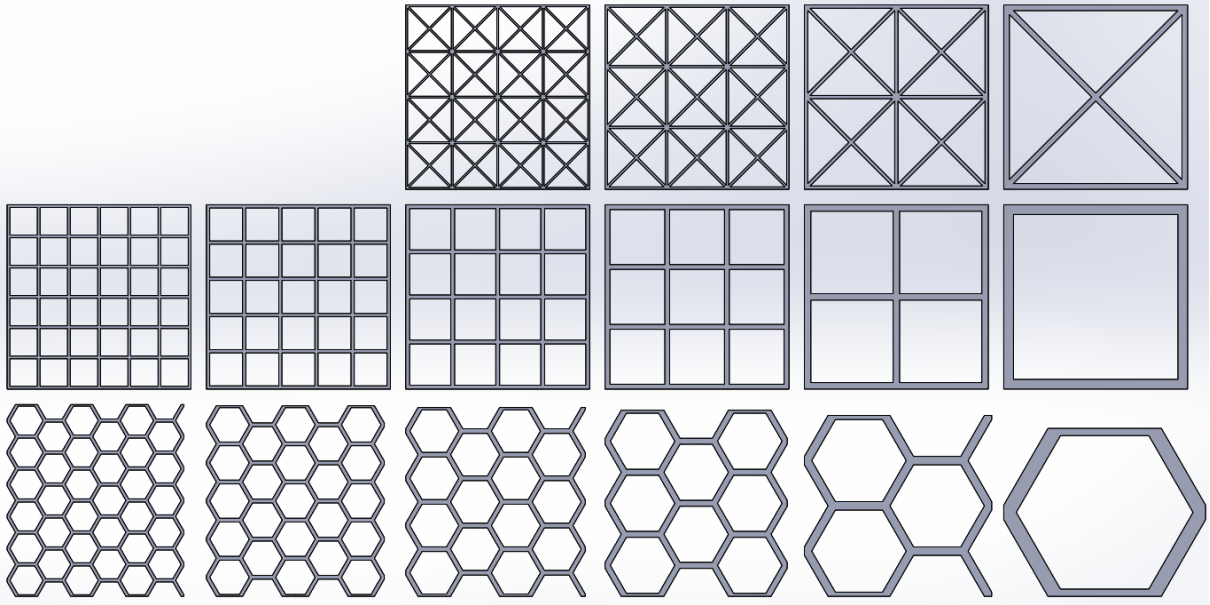

Figure 4.2.2 – nxn cell structures for triangular, square, and hexagonal honeycombs at $\bar{\rho}$ of 20%.

4.3 - Results

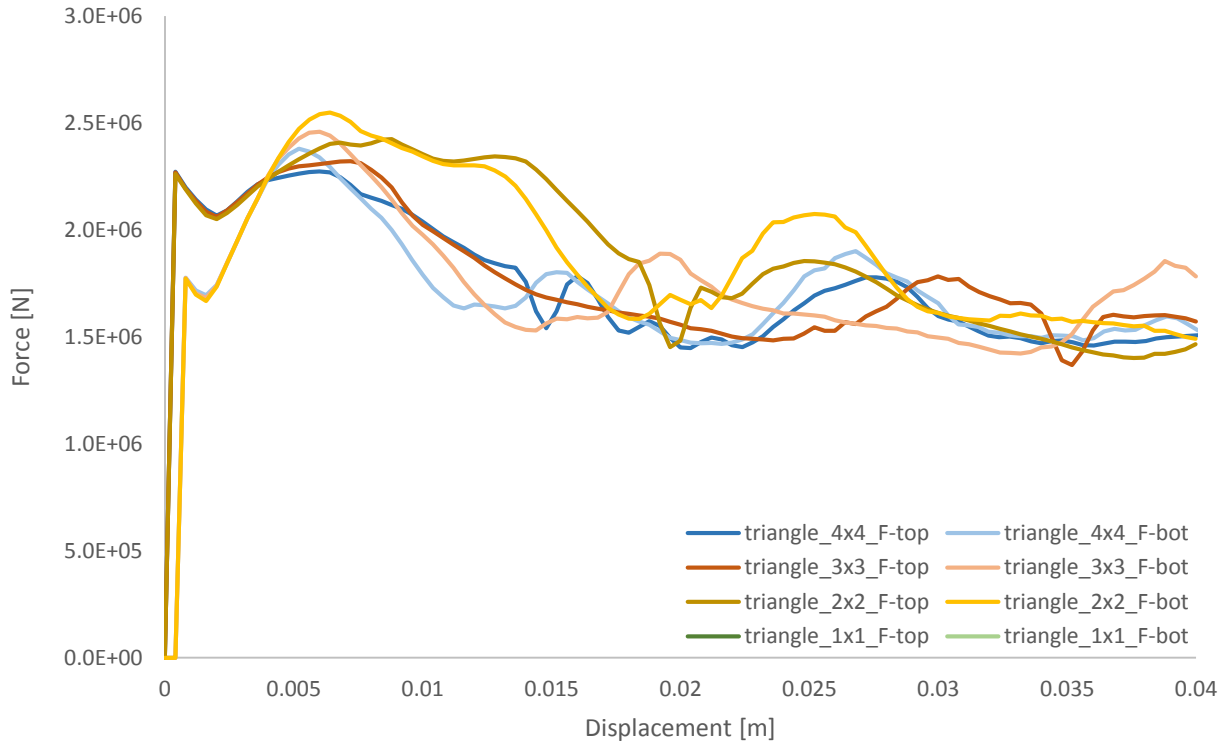

Figure 4.3.1 – Force displacement curves for triangular honeycombs.

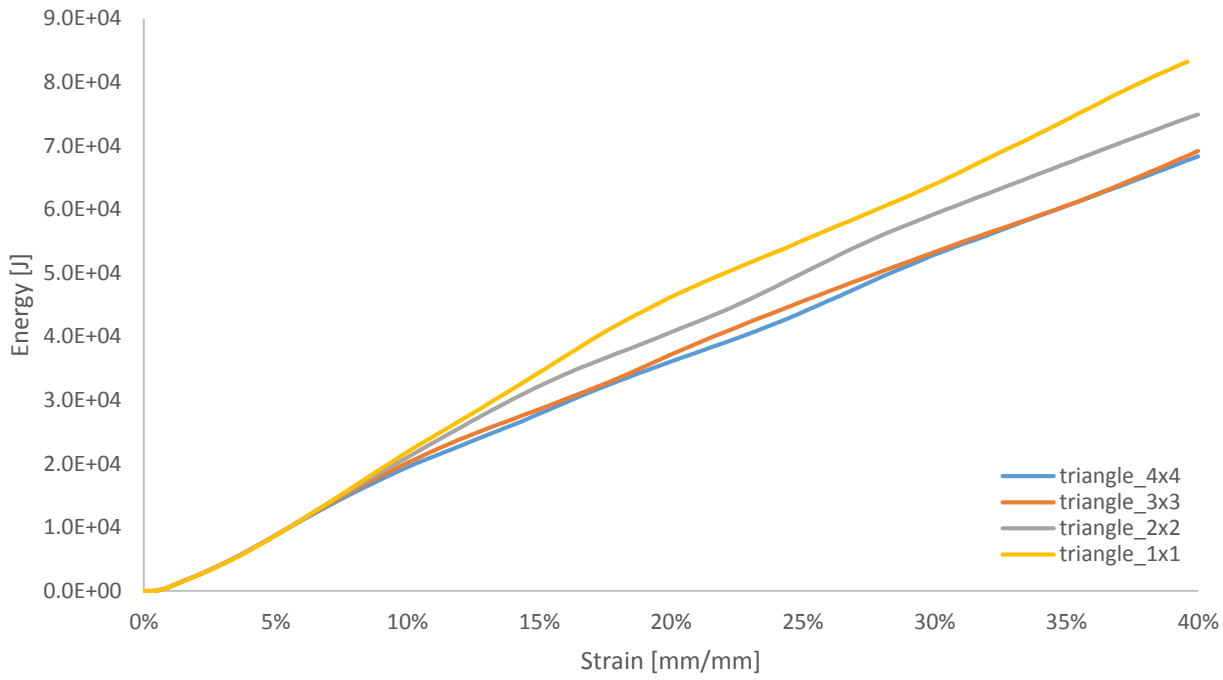

Figure 4.3.2 – Energy absorbed by triangular honeycombs of equal mass and boundary area.

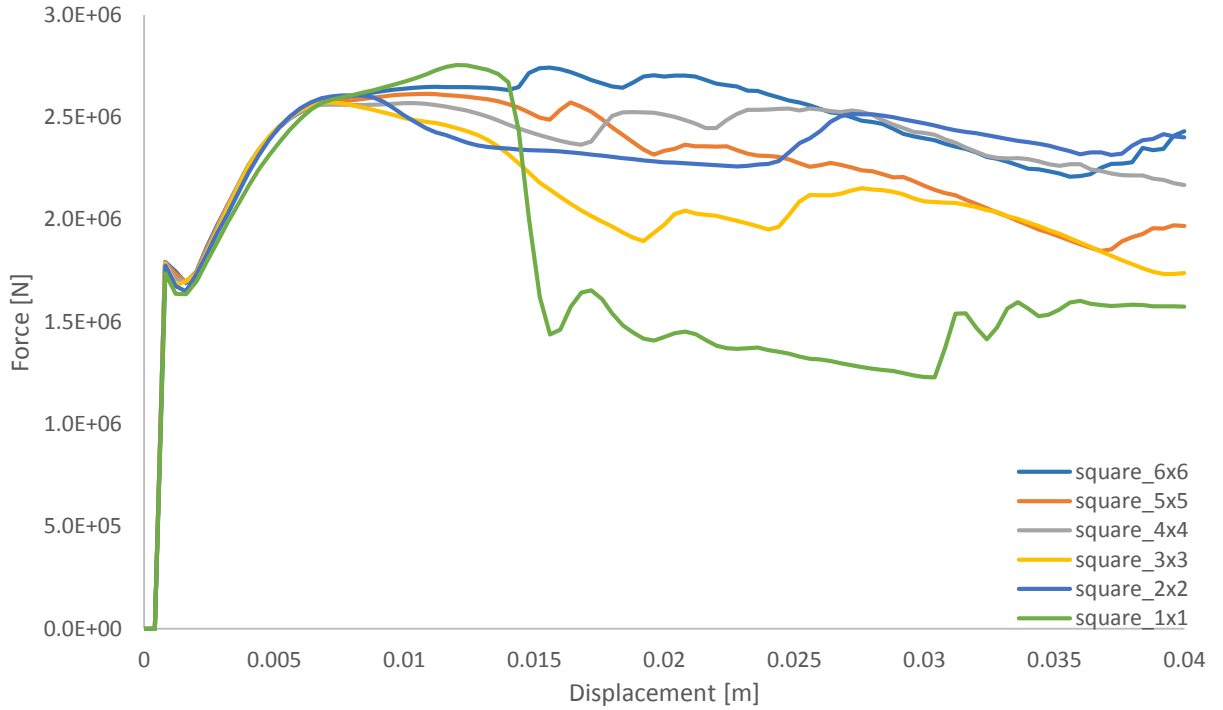

Figure 4.3.3 – Force displacement curves for square honeycombs.

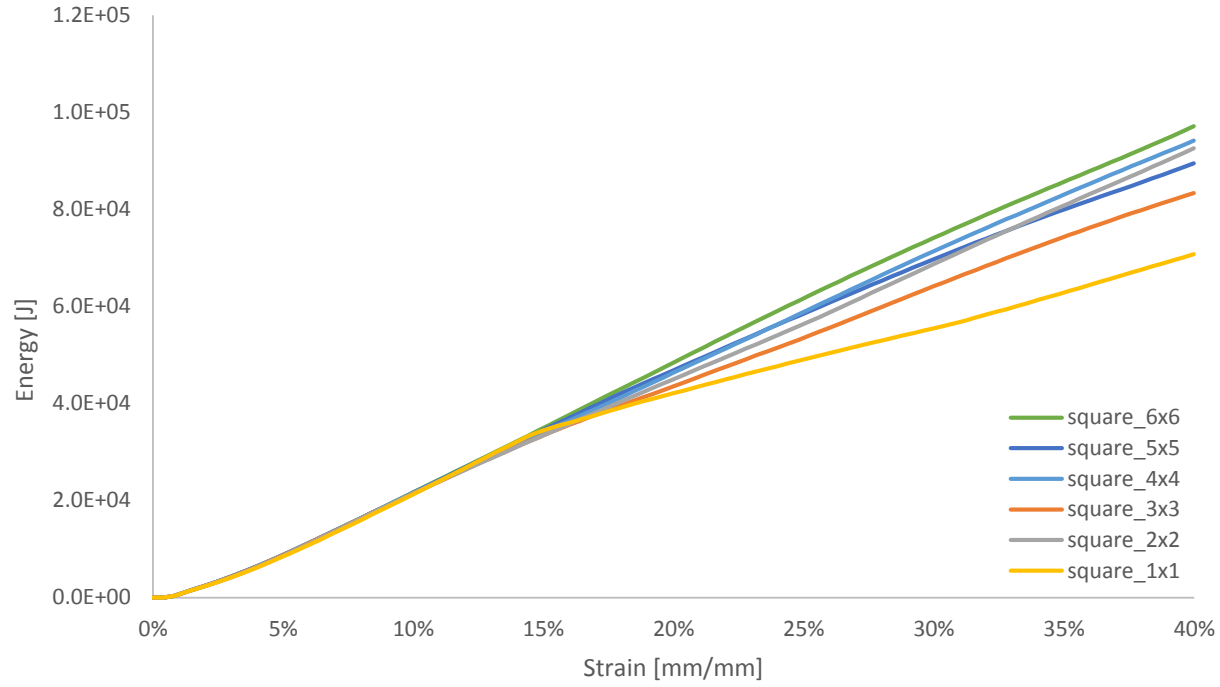

Figure 4.3.4 – Energy absorbed by square honeycombs of equal mass and boundary area.

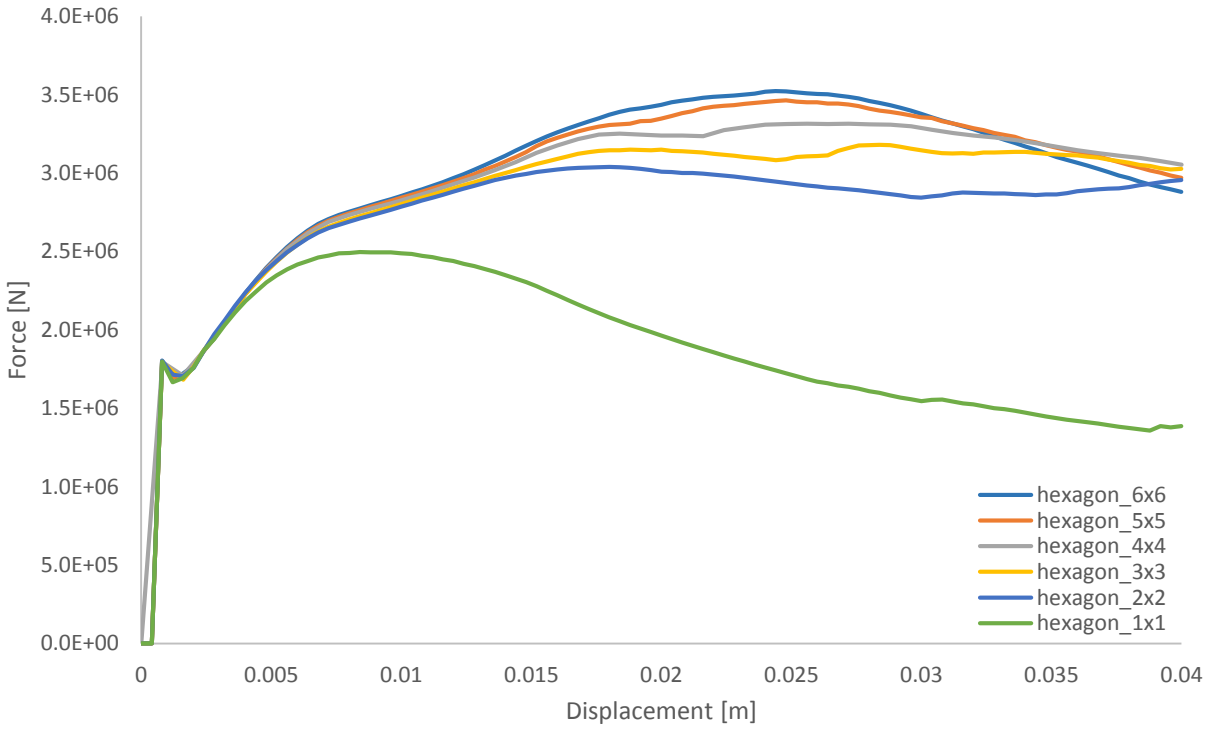

Figure 4.3.5 – Force displacement curves for hexagonal honeycombs.

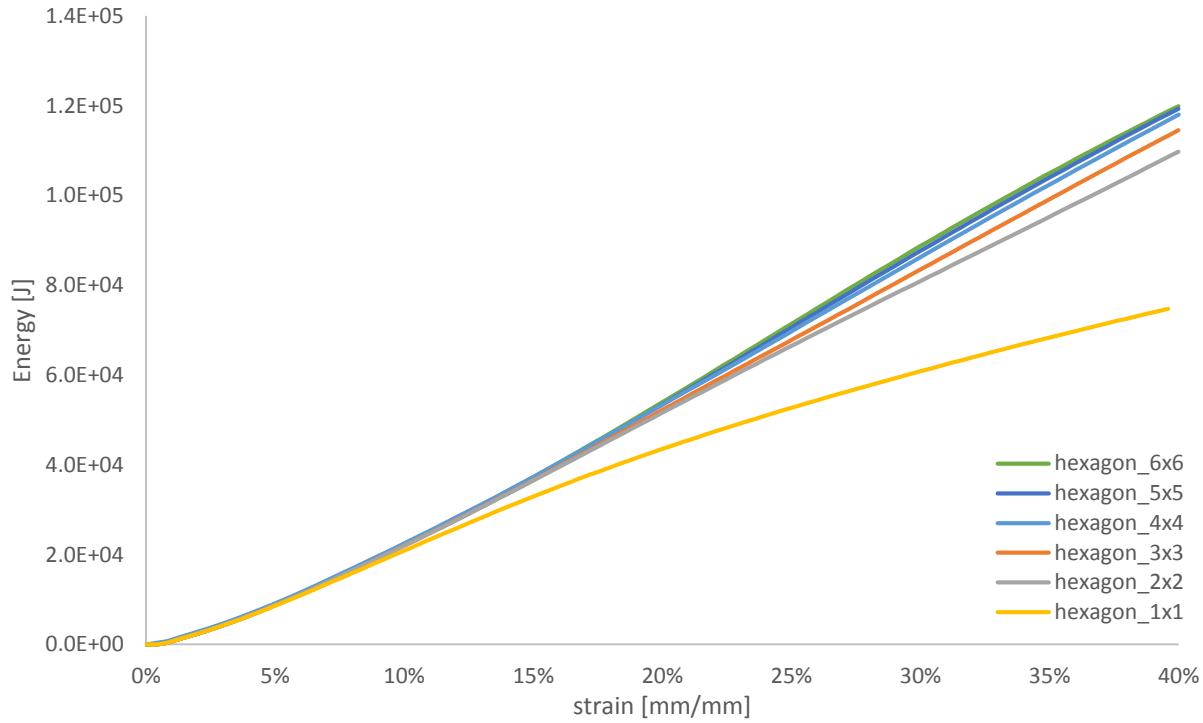

Figure 4.3.6 – Energy absorbed by hexagonal honeycombs of equal mass and boundary area.

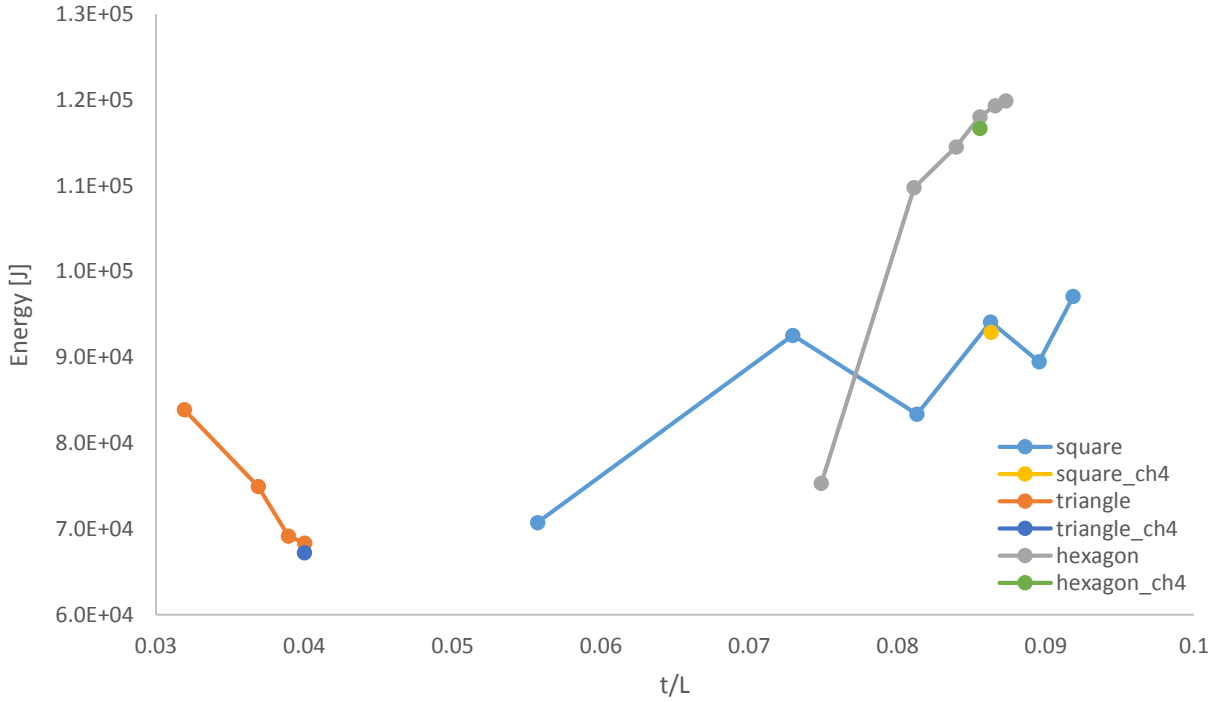

Figure 4.3.7 – Energy absorbed with respect to aspect ratio for square, triangular, and hexagonal honeycombs. Mass normalized results from chapter 4 are included for each honeycomb type to show repeatability.

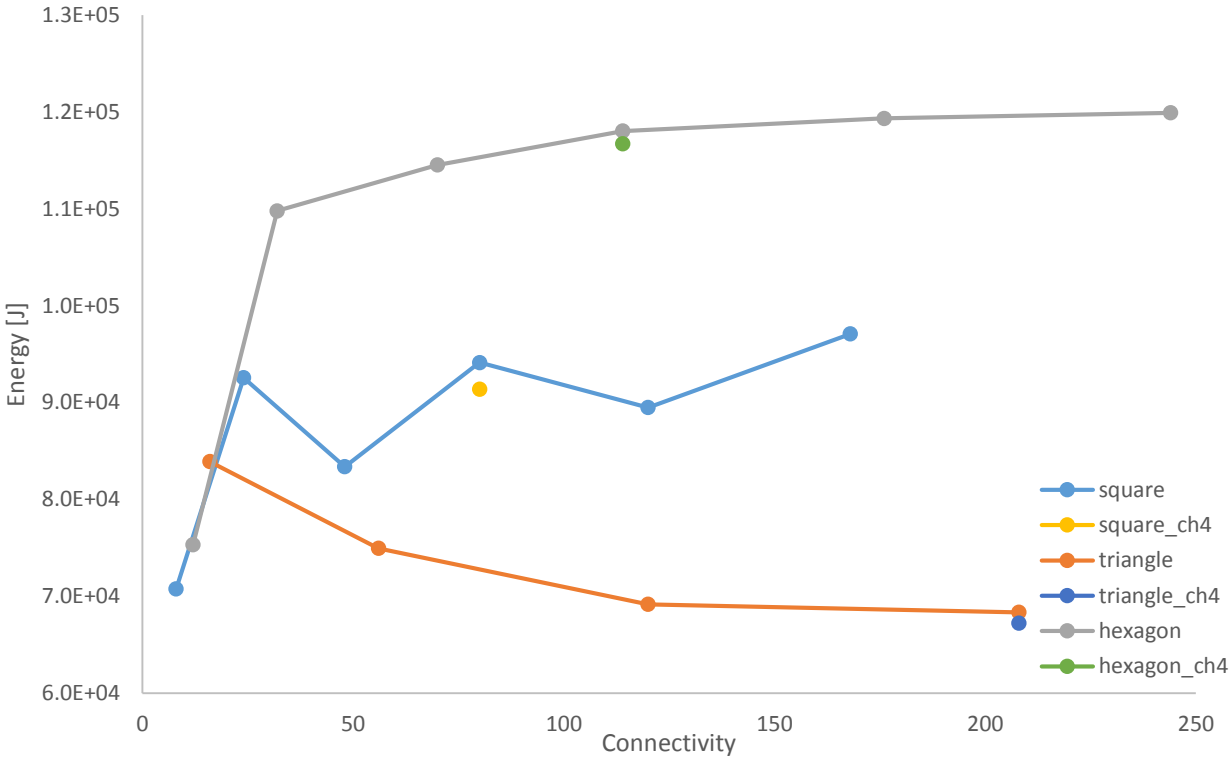

Figure 4.3.8 – Energy absorbed with respect to connectivity for square, triangular, and hexagonal honeycombs. Mass normalized results from chapter 4 are included for each honeycomb type to show repeatability.

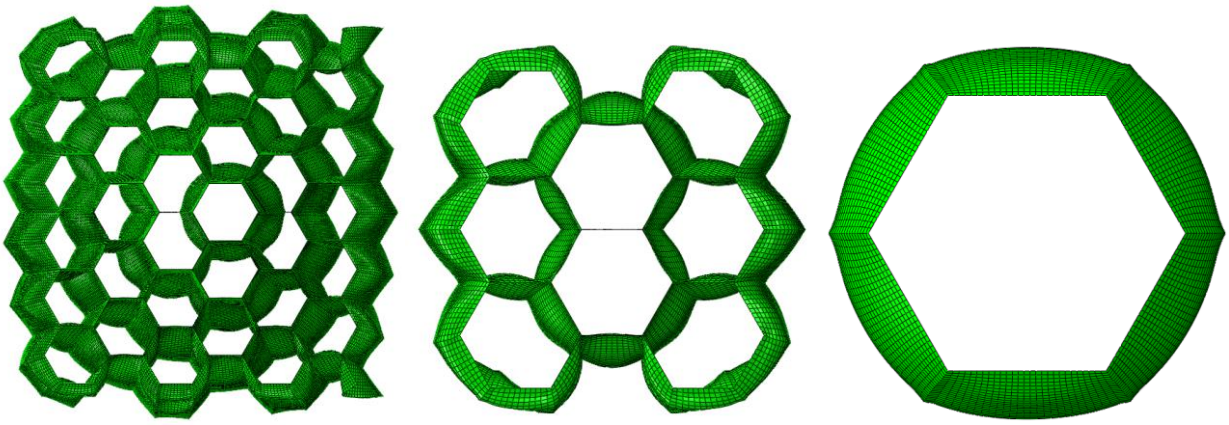

Figure 4.3.9 – Top view of hexagonal deformation for (left) 6x6, (middle) 3x3, and (right) 1x1 cell structures.

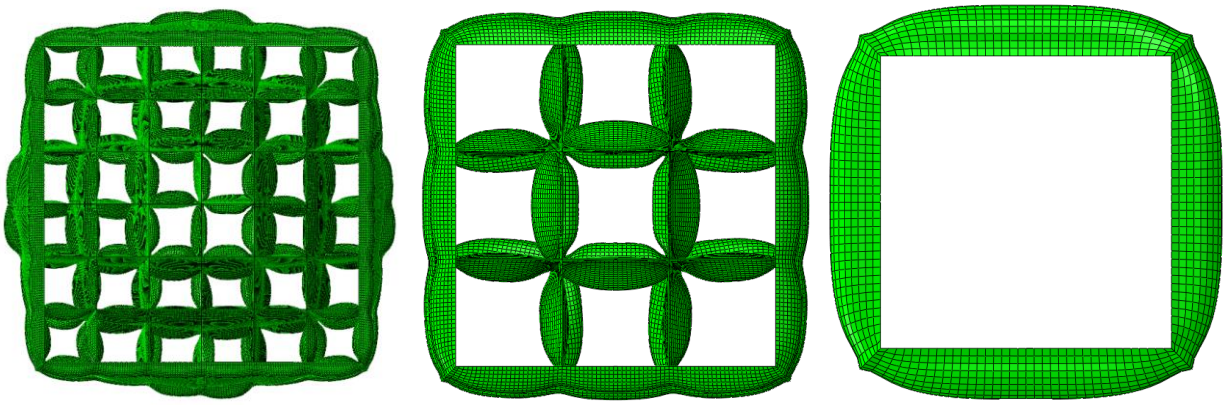

Figure 4.3.10 – Top view of square deformation for (left) 6x6, (middle) 3x3, and (right) 1x1 cell structures.

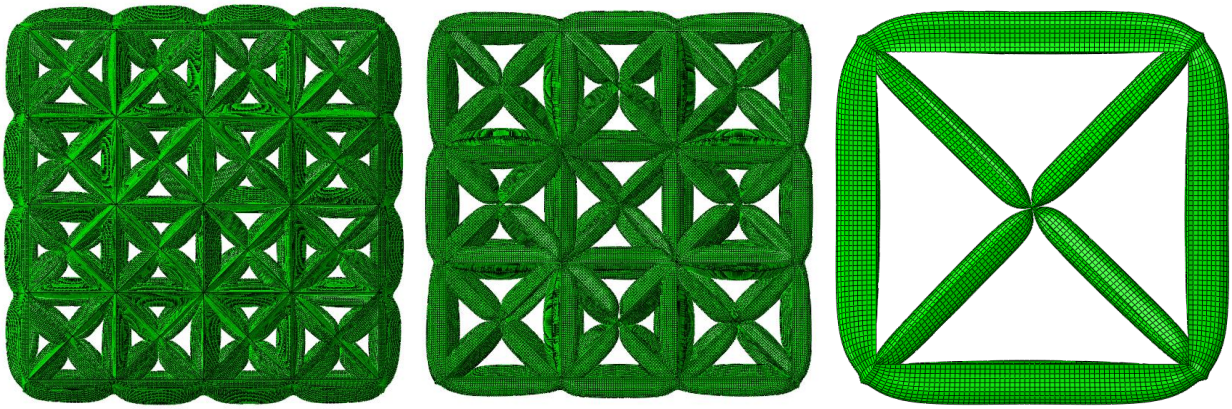

Figure 4.3.11 – Top view of triangular deformation for (left) 4x4, (middle) 3x3, and (right) 1x1 cell structures.

4.4 - Discussion

It's important to note that force-displacement curves don't exactly tabulate energy absorbed because of artificial energy contributions, but they are very close because artificial energies are kept below 5 % of total energy using the methods discussed in Chapter 2. Figure 4.3.2 shows that energy absorbed by triangular honeycombs increases as the number of cells within the system decreases, being maximized with only one cell. This figure also shows that increasing the number of cells beyond 3x3 has a negligible effect on energy absorbed. Figure 4.3.4 shows that square honeycombs generally absorb more energy when cell number increases and that having 1x1 cell structure dramatically reduces absorbed energy. Figure 4.3.6 shows energy absorption increases with *n* and that absorption is greatly reduced when the structure is a single cell. Figure 4.3.7 shows several important characteristics about the honeycombs being considered. It's

important to note from the tables above that *t/L* increases with *n*. Figure 4.3.7 shows square and hexagonal structures' energy absorbance increase with *t/L*—square being less dramatically influenced than hexagonal over the range examined. The triangular geometry shows the opposite, decreasing in absorbance with increasing *t/L*. Figure 4.3.8 shows hexagonal and square honeycombs have increased energy absorbance with larger connectivity while the triangular honeycombs perform best with minimal connectivity. Figure 4.3.8 also indicates the number of cells required by each geometry to approximately represent periodicity, or the number of cells required for no boundary effects to be present. Figure 4.3.9 shows hexagonal topology has all walls deforming in a low frequency manner for each *nxn* structure. Figure 4.3.10 shows all interior square topologies exhibit higher frequency buckling for 6x6 and 3x3 structures while low frequency is seen for 1x1 structure. Figure 4.3.11 shows that triangular topology always buckles at low frequency at the external walls vs. high frequency internally.

There are a few important characteristics that have emerged from this chapter. They are (1) hexagonal honeycombs again offer the greatest energy absorbance per unit mass when compare to square or triangular honeycombs at the same relative density. A 23% increase and 43% increase is seen when comparing maximum absorbance of hexagonal structure to those of square and triangular, respectively. This information is easily pulled from Figure 4.3.7. (2) Each structure has maximized or near maximized absorbance at different *t/L* values. Figure 4.3.7 shows the range of *t/L* values inherited by the area and boundary conditions in this chapter allow for hexagonal structure to converge to a maximized energy absorption but square and triangular geometries do not. If anything, triangular absorption is found to converge toward a minimum value. The next chapter will use an approach similar to chapter 4 to find the aspect ratios at which square and triangular honeycombs are maximized, tabulating hexagonal structure as well.

Chapter 5 - Aspect Ratio

5.1 - Introduction

The previous chapter showed a tendency for each topology to have enhanced energy absorption at different *t/L* values. The object of this chapter is to isolate the *n* values for which *t/L* tends not to change, removing the energy absorption dependence on aspect ratio found in the previous chapter. This is done using two approaches—an unbounded one like that used in Chapter 3 and a bounded one like in Chapter 4. The unbounded approach allows a large out-of-plane aspect ratio range to be looked at while the bounded method focuses on a smaller range. Bounded means the external area or perimeter is fixed, inherently fixing mass provided relative density is constant. Unbounded means the area expands naturally as *n* changes. To be more precise, the bounded area employs a third equation to solve for *B* as well as *t* and *L*, while unbounded uses only two equations to solve for *t* and *L*. Mass increases as hexagonal area increases during the unbounded analysis.

5.2 - Unbounded

5.2.1 - External Constraints and Boundary Conditions

All proceeding geometries will be based upon their infinite *nxn* sheets at 20% relative density. The same equations as before can be used to find *n* values at which *t/L* is constant or within a small tolerance of constant. Figure 5.2.1 shows *t/L* approaching constant values for each structure. It's important to point out that *n* is likely to be a large number when honeycombs are used in large sheets as energy absorbers. This relationship holds true regardless of which component—area, *t*, or *L*—is prescribed when solving for *n*. This is important because last chapter revealed an energy absorption dependence on *t/L* and we know *t* can substantially influence total solve time.

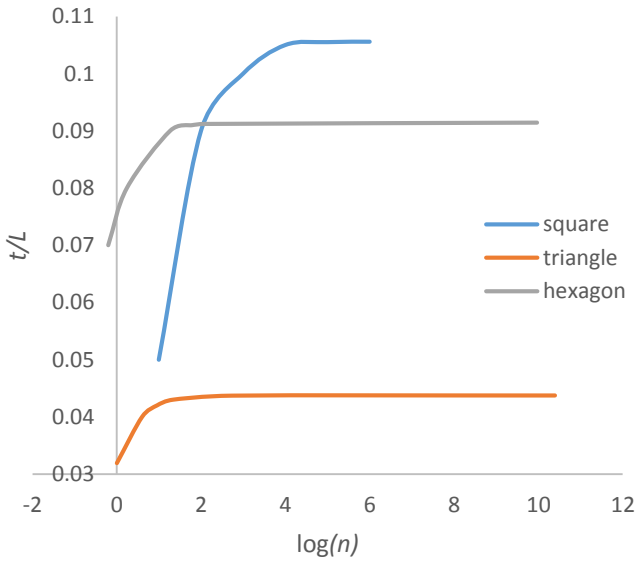

Figure 5.2.1 – In-plane aspect ratio's dependence on n for honeycomb structures.

5.2.2 - Procedure

Chapters 2 shows the solution is converged at global shell element size $t/2$. Since t/L is not dependent on t, it follows from a computational efficiency standpoint that t values should be chosen such that solve time is reasonable. The approach for this section is to generate models spanning the threshold n value of 20 from the left and right, removing energy absorbance dependence on t/L. An overall bounding area of 16 m^2 produces a thickness of 8.57 mm for a 20x20 triangular honeycomb; this thickness yields a reasonably large stable time increment, therefore 16 m^2 will be bound each geometry. Table 5.2.1 shows that an n value of 20 produces t/L ratios within 5 % of a constant value for each cell structure. This means using 20x20 structure suffices to describe a systems where $n \rightarrow \infty$, in terms of in-plane aspect ratio. Approaching the threshold t/L values from left and right means to generate structures with approximately $10 \leq n \leq 30$ so that a pattern is recognizable. Results are then normalized by mass.

Table 5.2.1 – Aspect ratios of cell structure at n of 20.

	Triangle	Square	Hexagon
t/L	0.04293437	0.10105360	0.09010863
% max	98.2%	95.7%	98.6%

Table 5.2.2 – Triangular cell structure for constant area and relative density.

n	30	22	20	15	10	5
t [mm]	5.75	7.80	8.57	11.35	16.80	32.31
L [mm]	133.14	181.46	199.57	265.91	398.32	793.54
t/L	0.04320	0.04301	0.04293	0.04268	0.04217	0.04071
H/L	0.75	0.55	0.50	0.38	0.25	0.13

Table 5.2.3 – Square cell structure for constant area and relative density.

n	40	30	22	20	15	10	5
t [mm]	10.30	13.62	18.36	20.11	26.39	38.39	70.38
L [mm]	99.74	132.88	180.98	198.99	264.91	396.16	785.92
t/L	0.10326	0.10252	0.10145	0.10105	0.09963	0.09691	0.08955
H/L	1.00	0.75	0.55	0.50	0.38	0.25	0.13

Table 5.2.4 – Hexagonal cell structure for constant area and relative density.

n	30	20	15	10
t [mm]	14.88	22.14	29.29	43.25
L [mm]	164.34	245.70	326.53	486.64
t/L	0.09054	0.09011	0.08969	0.08887
H/L	0.61	0.41	0.31	0.21

5.2.3 - Results

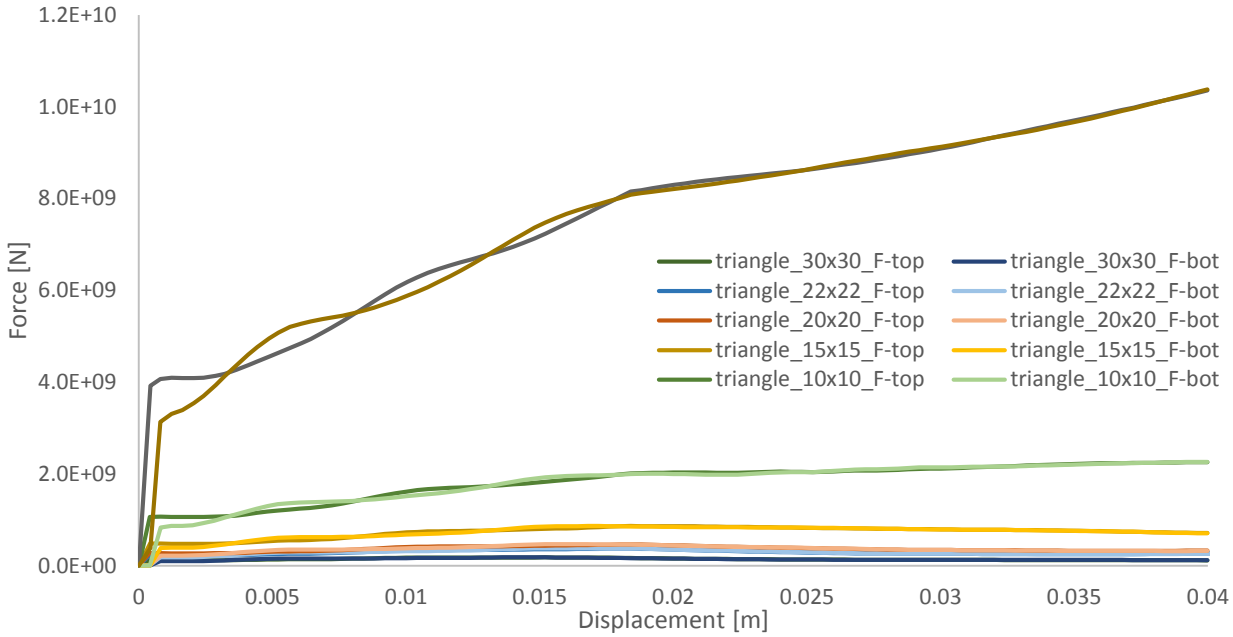

Figure 5.2.2 – Force displacement curves for triangular honeycombs.

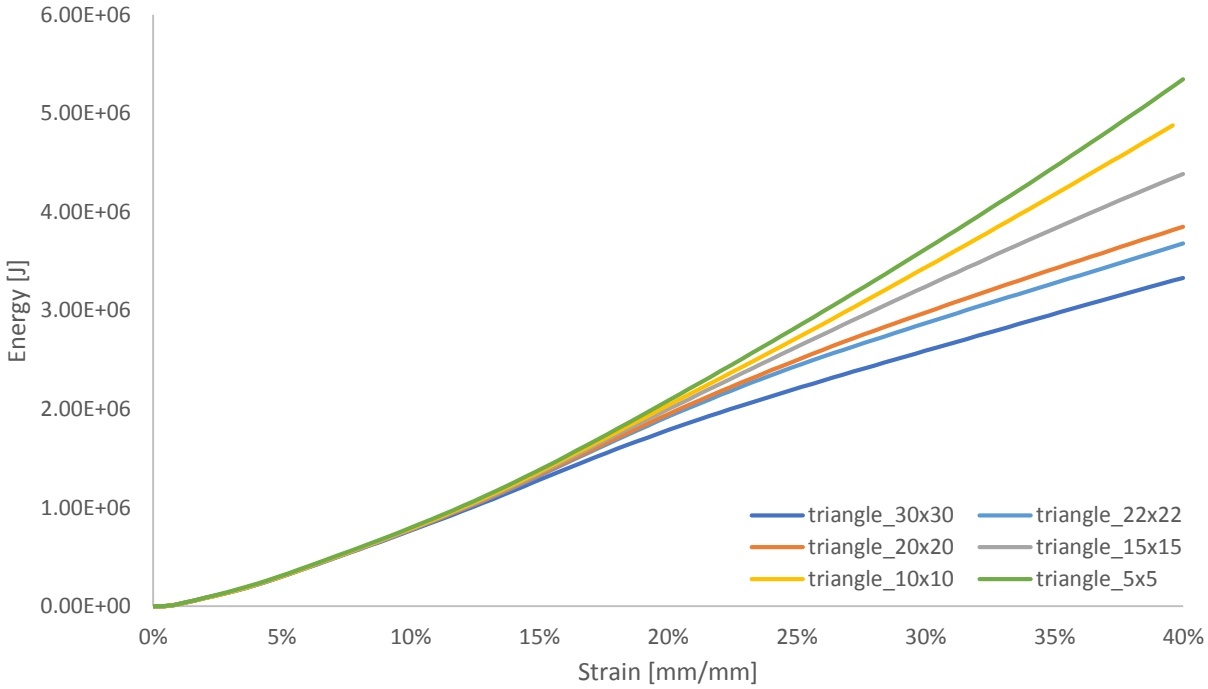

Figure 5.2.3 – Normalized energy absorbed by triangular honeycombs.

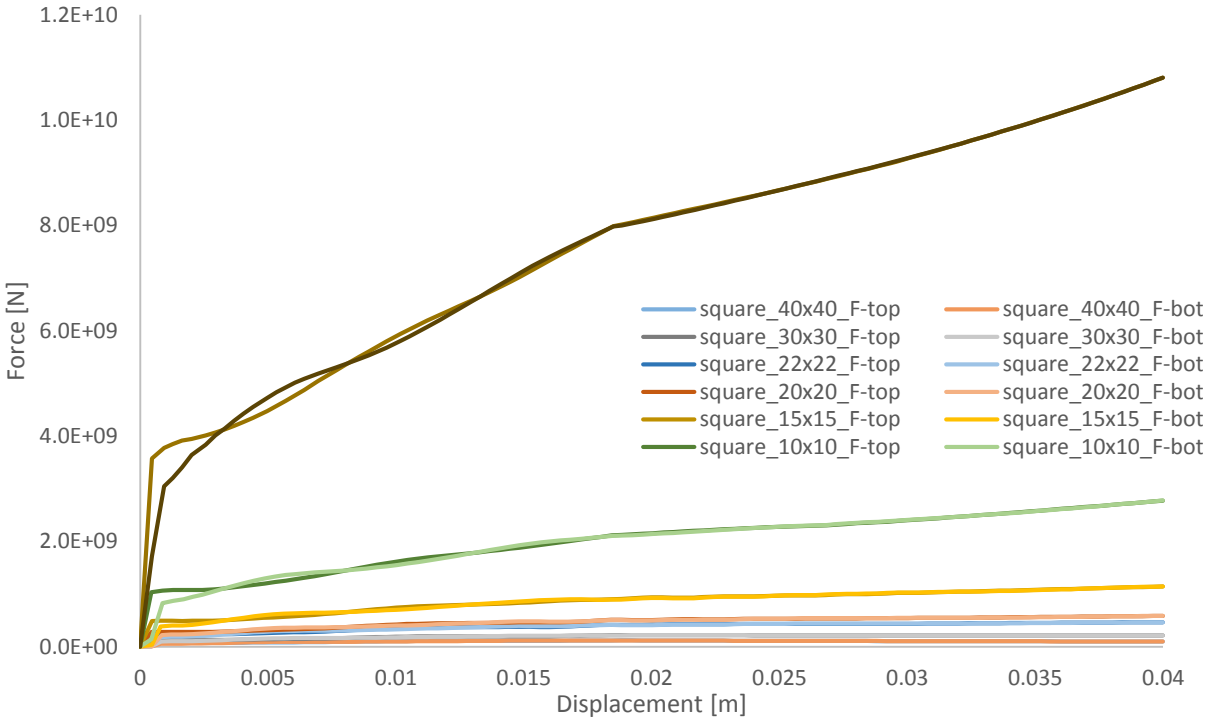

Figure 5.2.4 – Force displacement curves for square honeycombs.

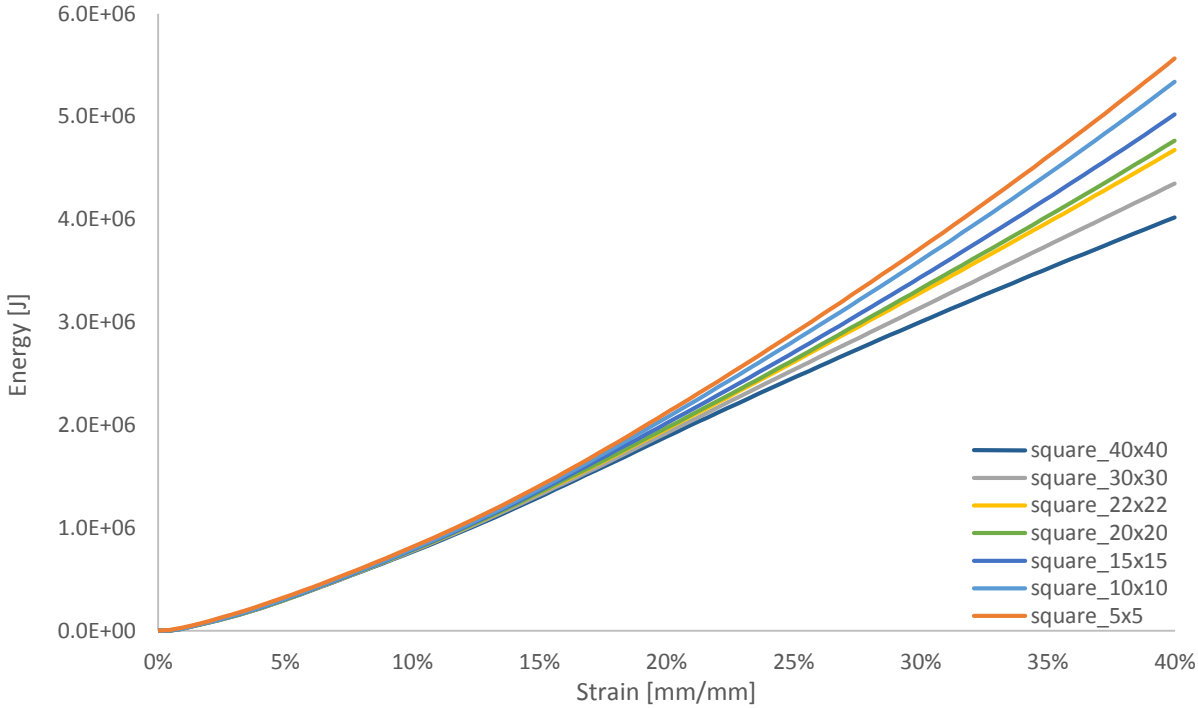

Figure 5.2.5 – Normalized energy absorbed by square honeycombs.

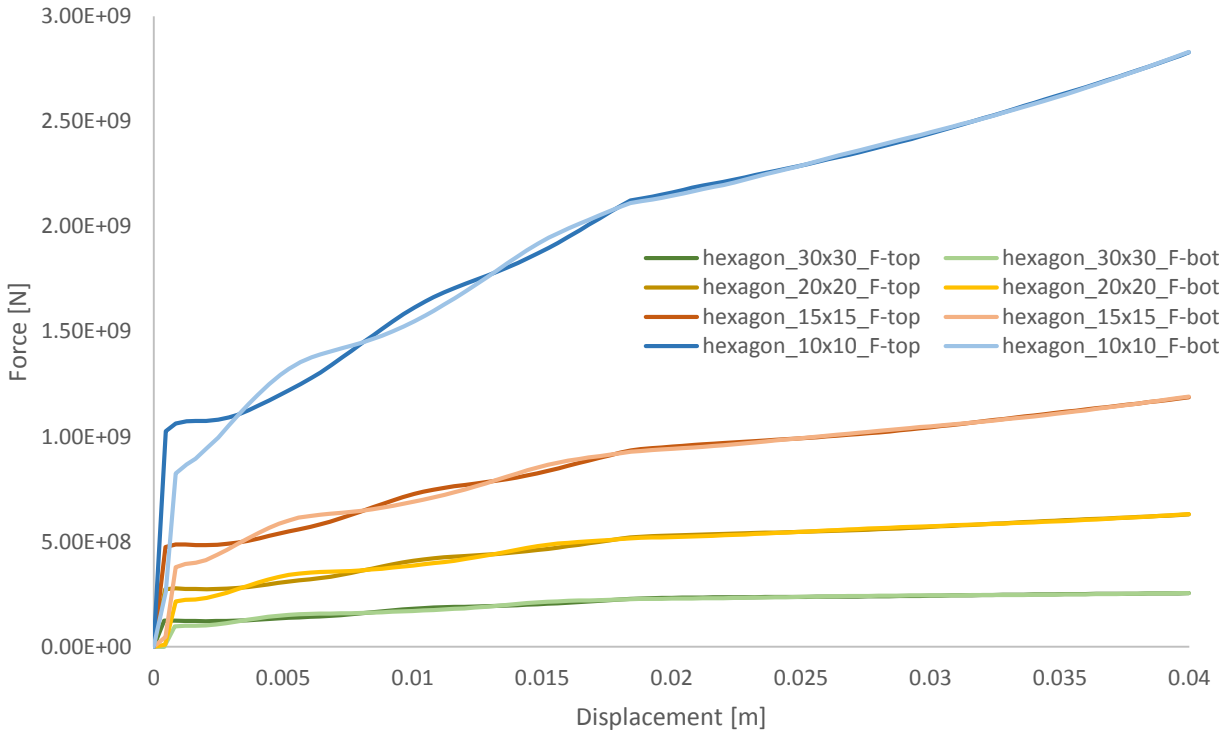

Figure 5.2.6 – Force displacement curves for hexagonal honeycombs.

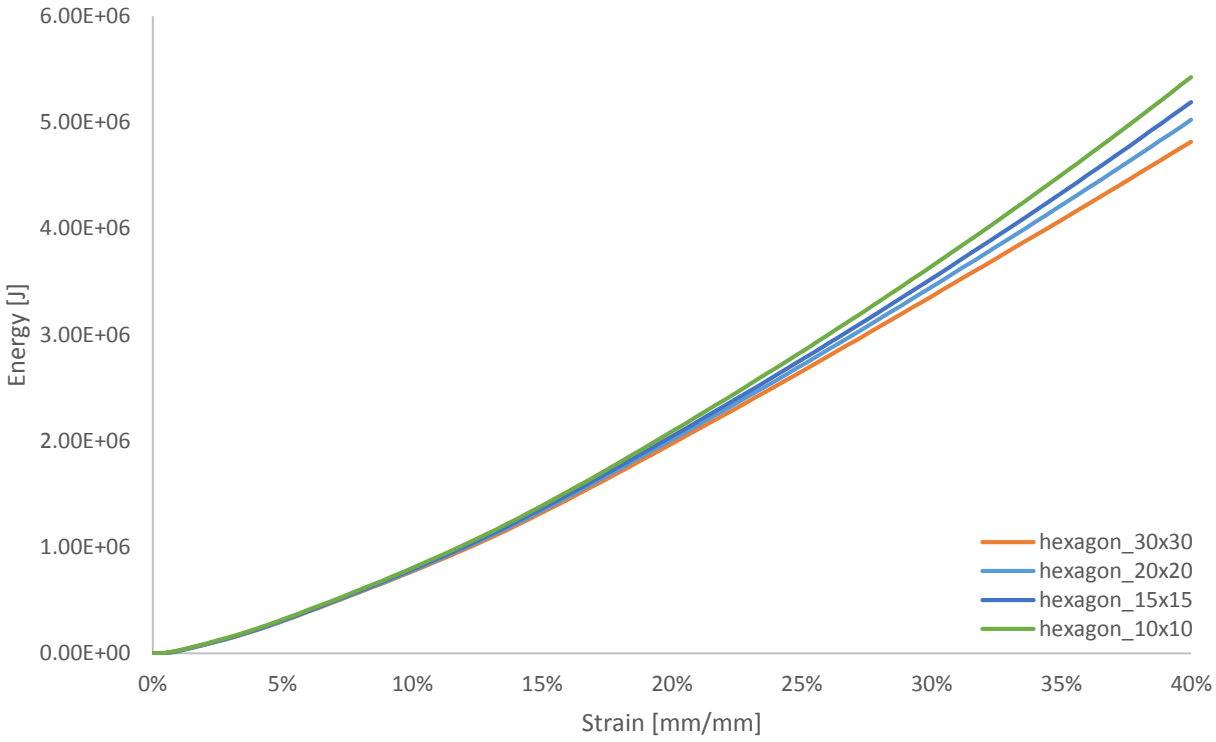

Figure 5.2.7 – Normalized energy absorbed by hexagonal honeycombs.

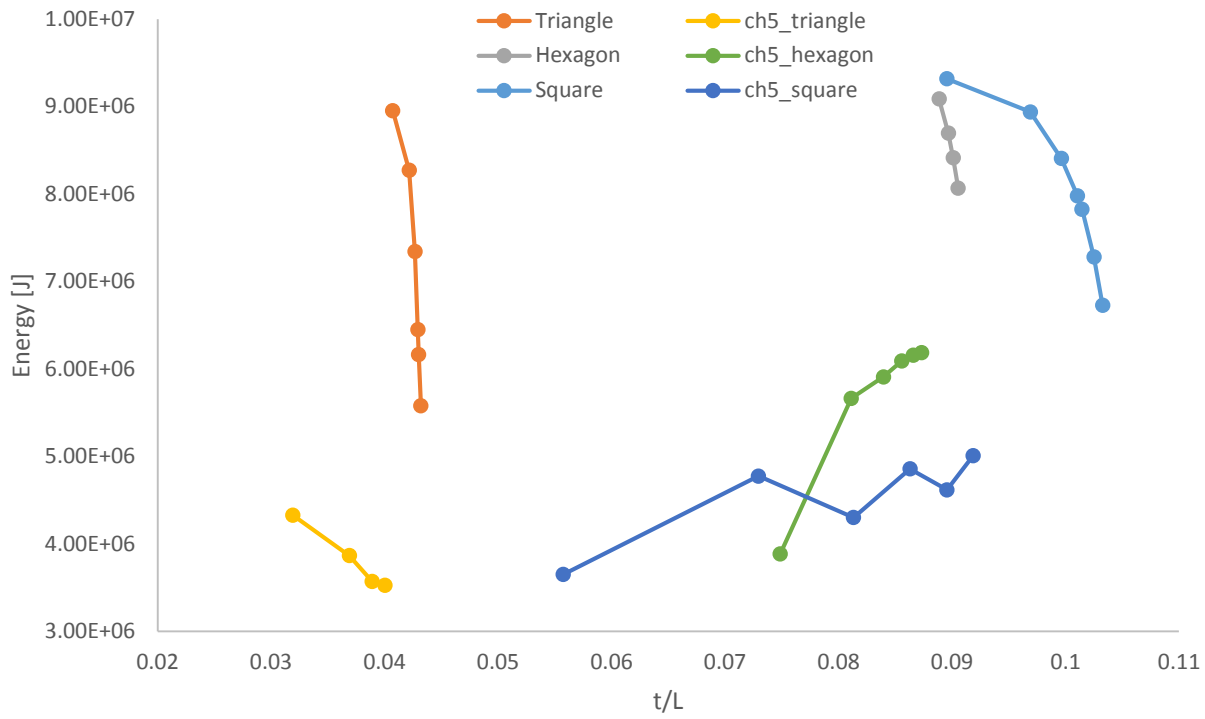

Figure 5.2.8 – Normalized energy vs. in-plane aspect ratio for honeycomb structures

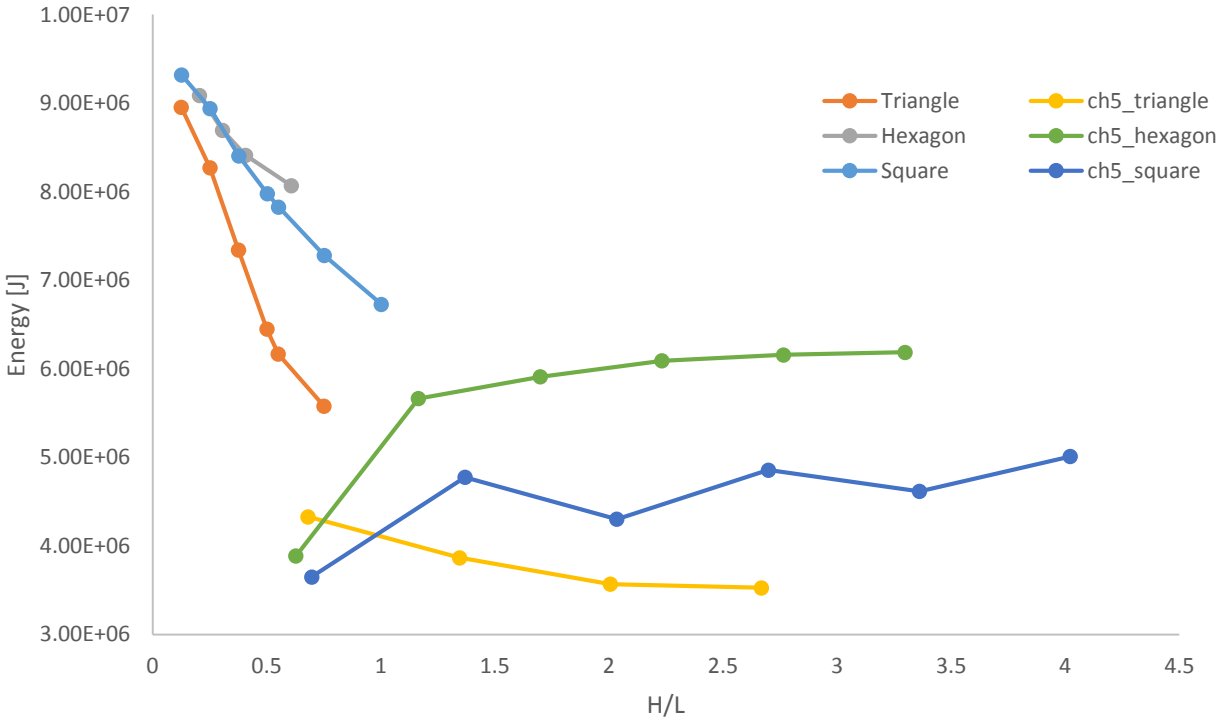

Figure 5.2.9 – Normalized energy vs. out-of-plane aspect ratio for Triangular, Square, and Hexagonal structures.

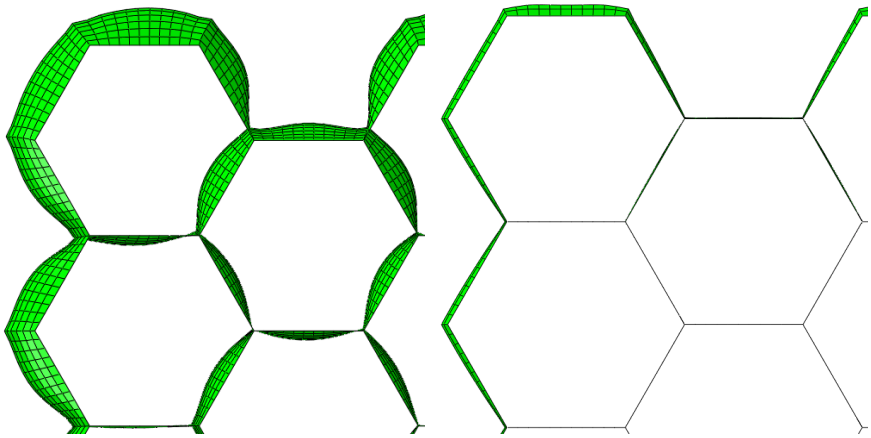

Figure 5.2.10 – Top view for hexagonal honeycomb corner bending, seen to be (left) substantial for n of 30 and (right) marginal for n of 10.

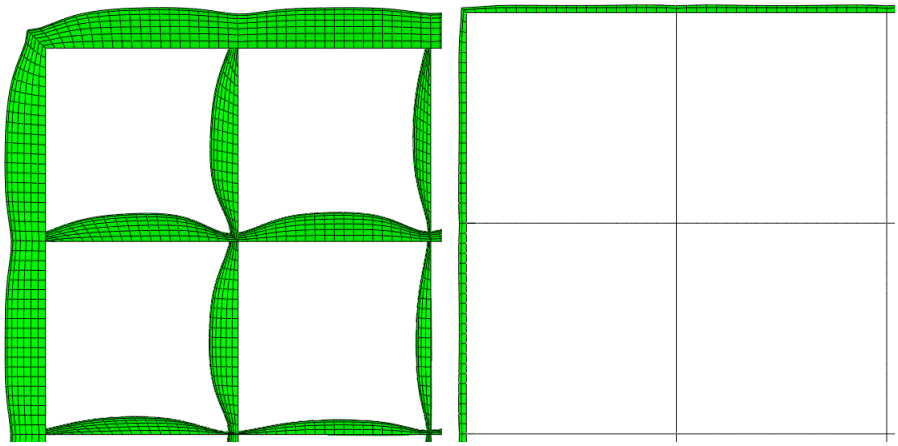

Figure 5.2.11 – Top view for square honeycomb corner bending, seen to be (left) substantial for n of 30 and (right) marginal for n of 10.

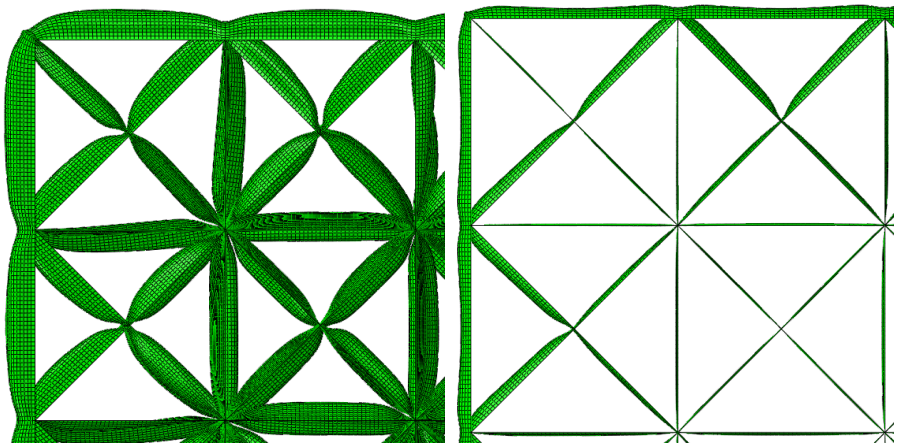

Figure 5.2.12 – Top view for triangular honeycomb center bending, seen to be (left) substantial for n of 30 and (right) marginal for n of 10.

The results of this section can be effectively determined by looking closely at Figure 5.2.8 and Figure 5.2.9. Both figures are normalized such that results have the same mass, just as in Chapter 3. The indication is that all cell structures show a sharp decrease in energy absorption with increasing *t/L*. This is an expected result for triangular structure according to the previous chapters' results. Square and hexagonal structures however, were supposed to show optimized energy absorbance characteristics as *t/L* approaches respective constant values at or beyond 20x20 cell types. The contrasting results are easily seen by observing the mismatch between current and Chapter 4 results on Figure 5.2.8 and Figure 5.2.9.

This mismatch is partially due to difference in approach between this section and the previous chapter—last chapter had the local number of cells being examined decrease as *H/L* decreased oppose to this section having a constant 8x8 locally examined cell. The most important relationship to take away from this section is the energy absorbance dependence on *H/L*, which is very apparent in Figure 5.2.9. Having $H/L \leq 0.25$ yields approximately the same response from square and hexagonal structures while triangular honeycombs have reduced absorption. Energy absorbance diverges as far as which cell structure is optimal as $H/L > 0.25$—the order of optimality being hexagonal, square, then triangular.

Figure 5.2.10 – Figure 5.2.12 show that each honeycomb has greater lateral deformation at larger *n* constructions. Larger *n* values correspond to larger *t/L* and *H/L* ratios for each topology, as seen on Table 5.2.2 – Table 5.2.4. By comparing Figure 5.2.9 with Figure 5.2.10 – Figure 5.2.12, we can safely say that smaller lateral deformation is associated with higher specific energy absorption. It is the goal of the next section to focus on small *H/L* ratios because this section has revealed it is more of an energy absorption determinant than *t/L*.

5.3 - Bounded

5.3.1 - External Constraints

This section uses the bounded approach like Chapter 4, where overall mass and relative density are fixed. It's best to fix mass along with relative density to avoid inertial contributions that may be nonlinear. Such contributions may have residuals once normalized by mass and may be an additional source of error. The process for this section is essentially the same as with the previous one, the difference being that the outer perimeter is fixed. An external area of 16 m^2 bounds each cell structure, meaning the relative density equations can be solved in the same

manner as in Chapter 4. The previous section revealed *t/L* isn't a dominating characteristic but allowing for the ratio to approach a constant value as before is a good idea. *n* is again chosen to approach 20 to accommodate an approximately steady-state *t/L* ratio, so each cell structure uses *n* of 20, 15, and 10 as seen on Table 5.3.1.

Table 5.3.1 – Square cell structure.

n	20	15	10
t [mm]	20.11	26.39	38.39
L [mm]	198.99	264.91	396.16
t/L	0.10105	0.09963	0.09691
H/L	0.50	0.38	0.25

Table 5.3.2 – Triangular cell structure.

n	20	15	10
t [mm]	8.57	11.35	16.80
L [mm]	199.57	265.91	398.32
t/L	0.04293	0.04268	0.04217
H/L	0.50107	0.37607	0.25105

Table 5.3.3 – Hexagonal cell structure.

n	20	15	10
t [mm]	22.14	29.29	43.25
L [mm]	245.70	326.53	486.64
t/L	0.09011	0.08969	0.08887
H/L	0.40700	0.30625	0.20549

5.3.2 - Results

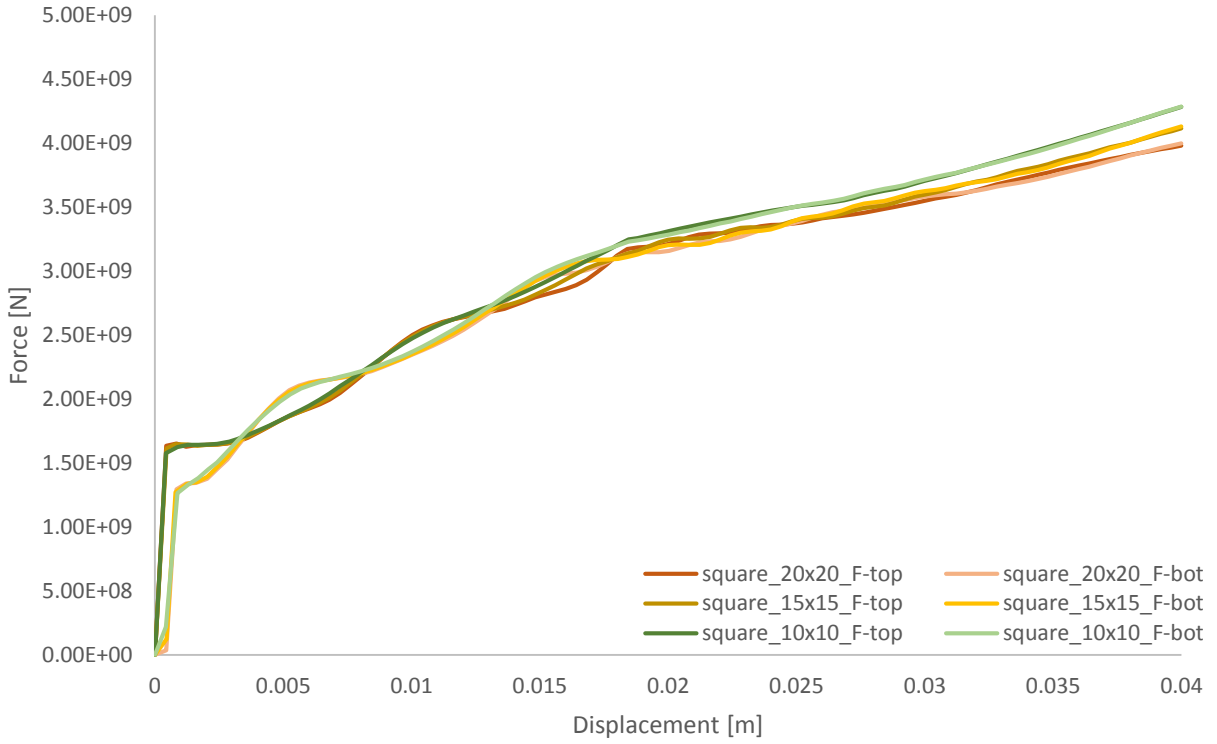

Figure 5.3.1 – Force displacement curve for square honeycombs.

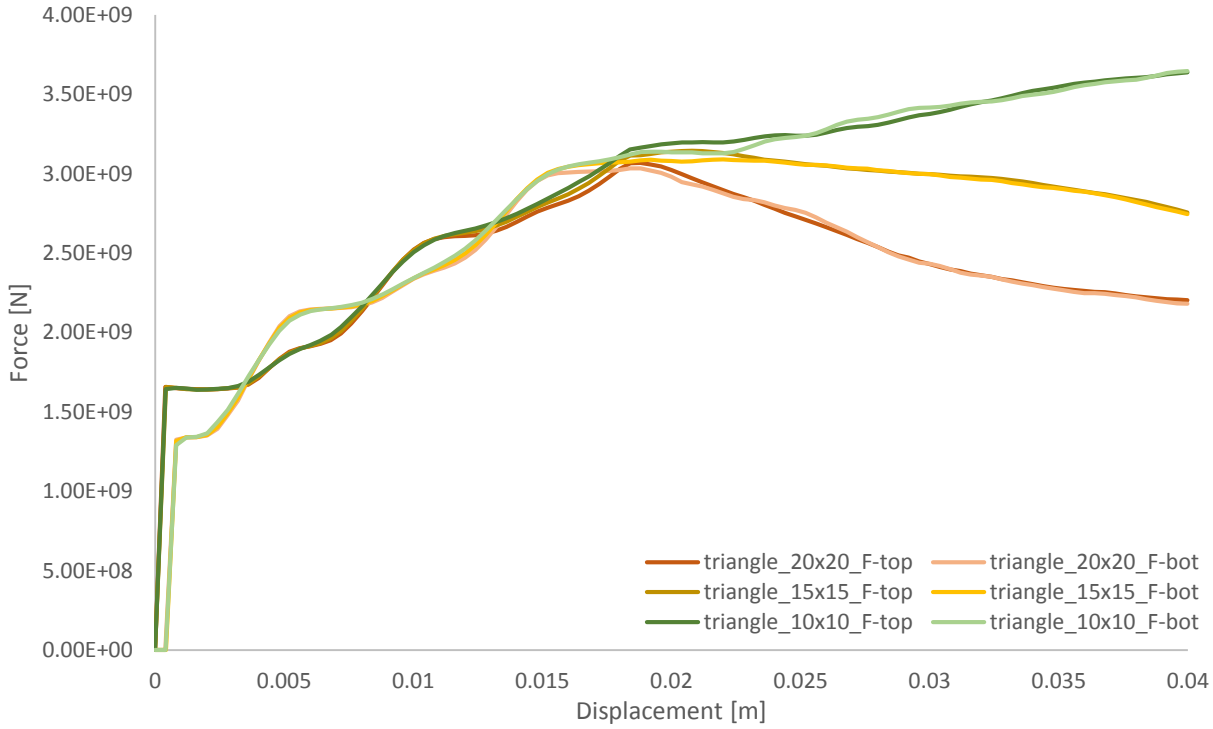

Figure 5.3.2 – Force displacement curve for triangular honeycombs.

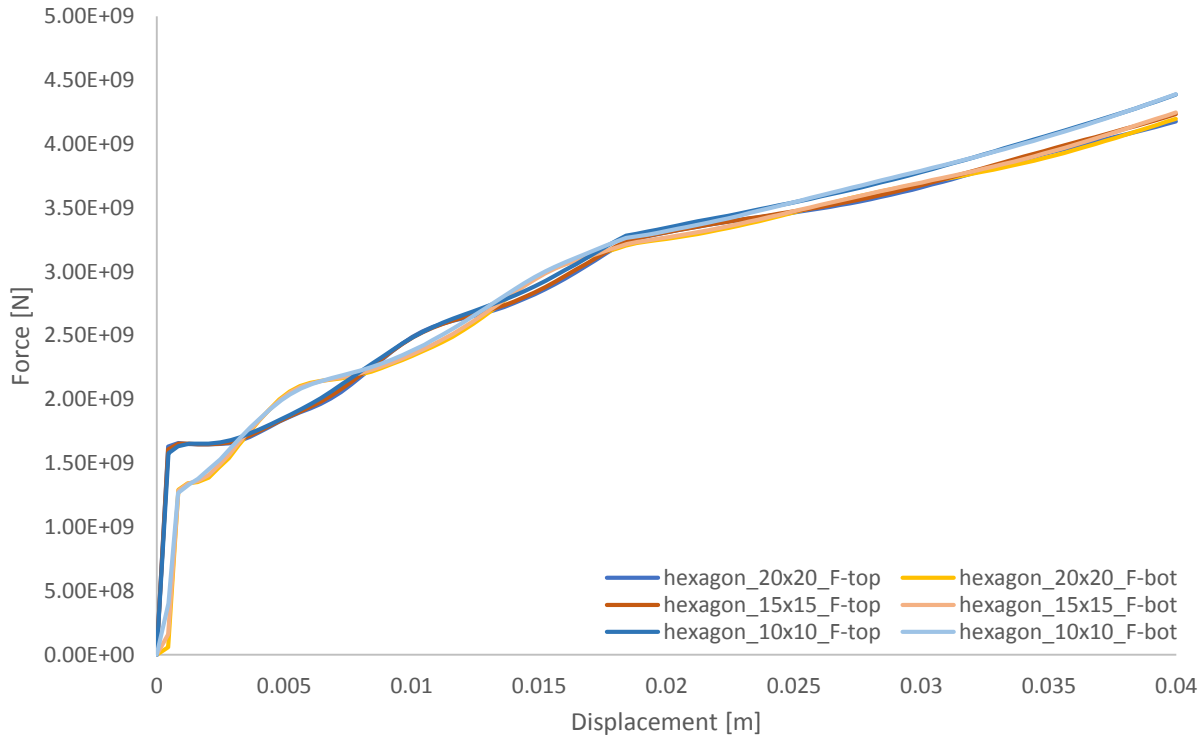

Figure 5.3.3 – Force displacement curve for hexagonal honeycombs.

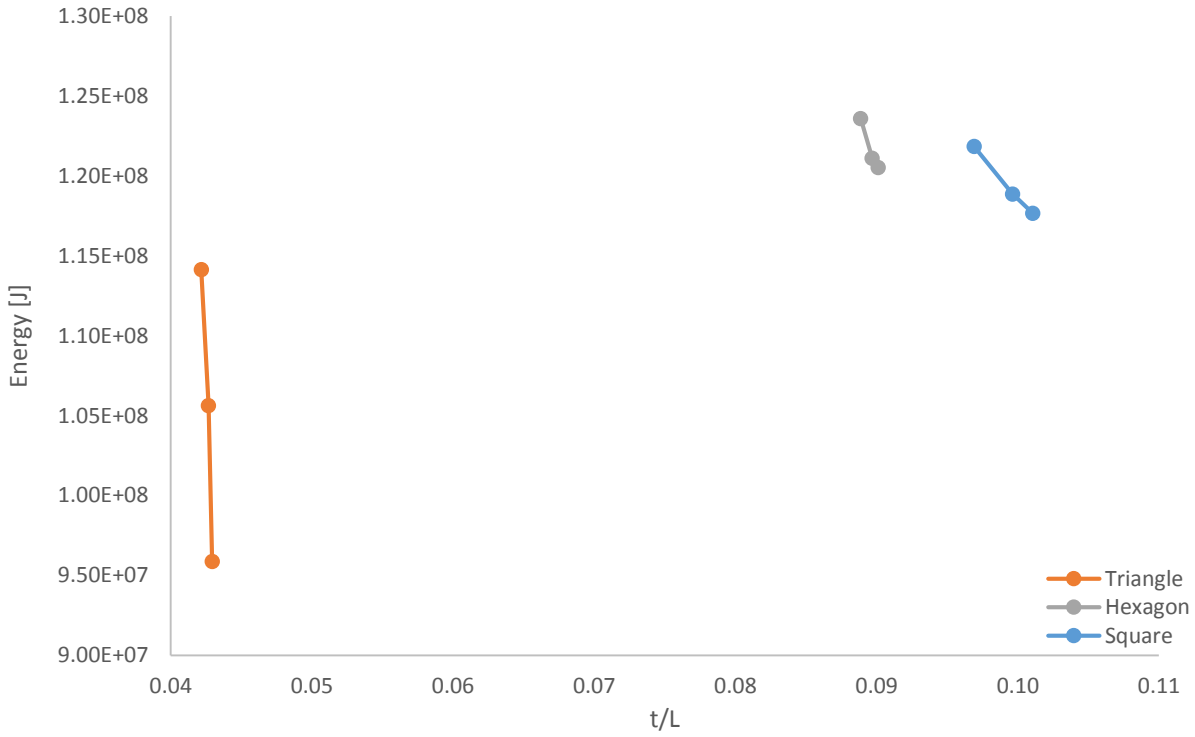

Figure 5.3.4 – Energy absorbed by honeycombs of different in-plane aspect ratio.

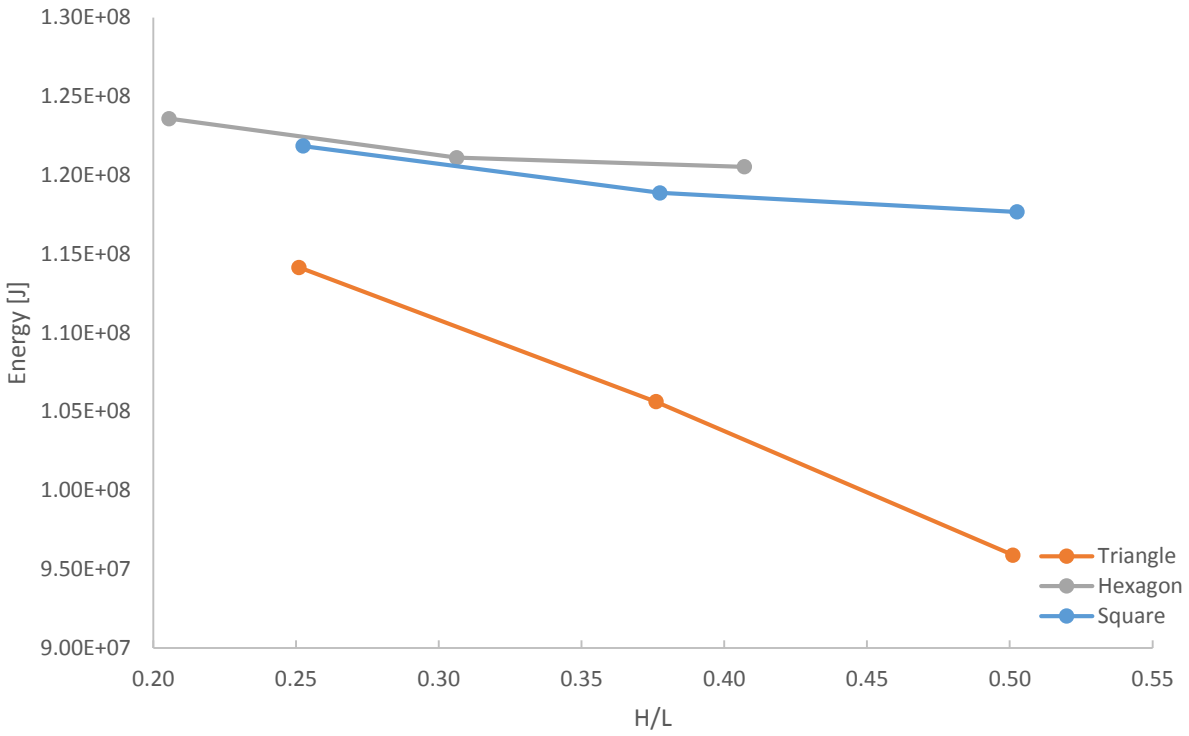

Figure 5.3.5 – Energy absorbed by honeycombs of different out-of-plane aspect ratio.

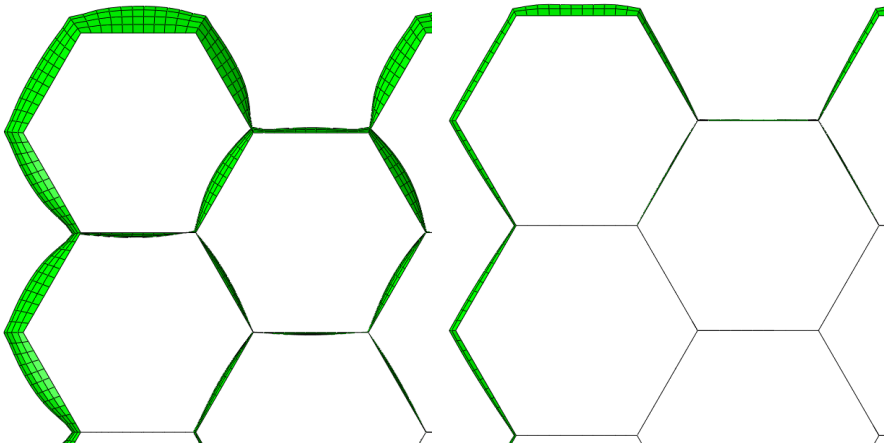

Figure 5.3.6 – Top view for hexagonal honeycomb corner bending, seen to be (left) substantial for n of 20 and (right) marginal for n of 10.

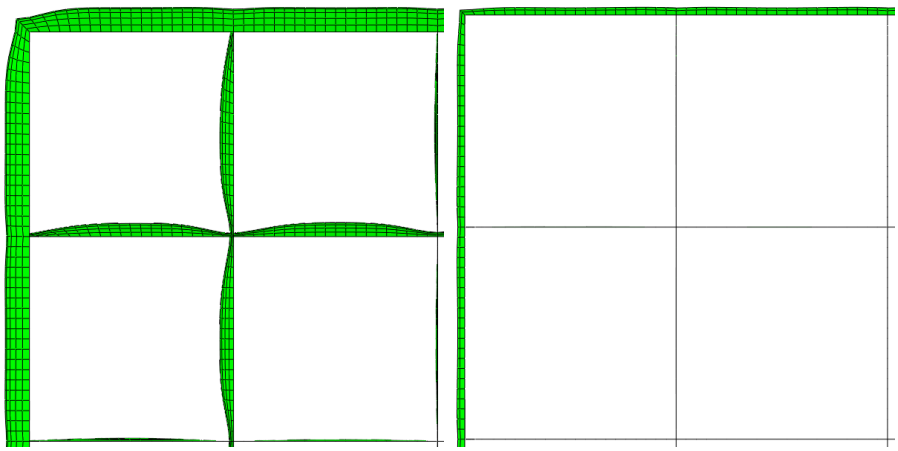

Figure 5.3.7 – Top view for square honeycomb corner bending, seen to be (left) substantial for n of 20 and (right) marginal for n of 10.

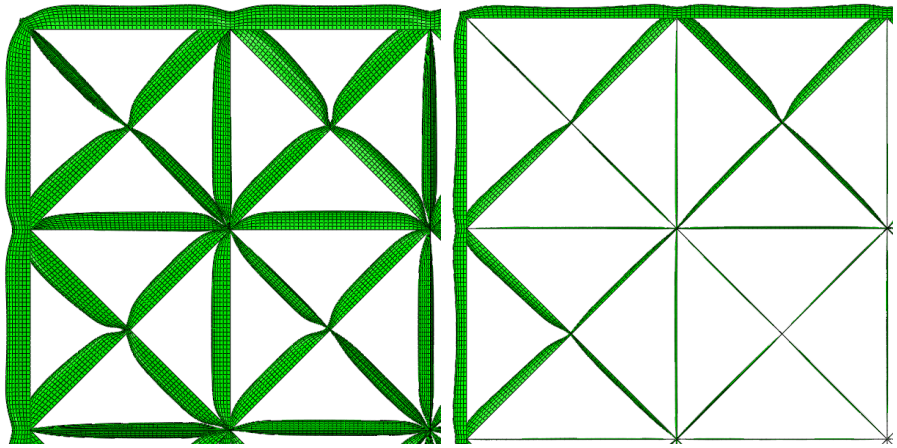

Figure 5.3.8 – Top view for triangular honeycomb center bending, seen to be (left) substantial for n of 20 and (right) marginal for n of 10.

Figure 5.3.1 and Figure 5.3.3 show little variation between force-displacement results for square and hexagonal topologies, respectively. Figure 5.3.2 however, shows a definite difference in strength characteristics of 10x10, 15x15, and 20x20 triangular topology after about 18 mm compression. This difference can be seen more clearly in the form of energy absorbed by looking at Figure 5.3.5, where smaller *H/L* correspond to smaller *n* structures. Figure 5.3.4 shows the same pattern as Figure 5.3.5 but unfortunately *t/L* is less indicative than *H/L* and the detail is accordingly reflected by comparing plots. Figure 5.3.5 shows that minimizing *H/L* allows energy absorbance to converge for hexagonal and square geometries at *H/L* of about 0.20 whereas triangular geometry requires a smaller *H/L* value if it is to converge at all. Figure 5.3.6 – Figure 5.3.8 show the same

trend as the previous section; greater energy absorption is observed to coincide with less lateral bending displacement.

5.4 - Discussion

This chapter has shown that out-of-plane aspect ratio *H/L* can be a good predictor of energy absorption—namely that more energy is absorbed when *H/L* is small. It's important to note that the results from Chapter 4 graphed along with the unbounded results from this chapter on Figure 5.2.9 in the *H/L* range of 0.5 – 1.5 show divergence, but this is due to boundary effects in the previous chapter as *n* approaches 1. Otherwise, there appears to be a decay to constant value as *H/L* becomes large for each topology. Once again, the order from greatest to least specific energy absorbed is hexagonal, square, and then triangular.

Chapter 6 - Mixed Mode Loading

6.1 - Introduction

All previous chapters have been an idealization in the sense that failure was induced by normal out-of-plane loading. Mixed mode loading is a critical part of impact because rarely is an impact exactly perpendicular to the surface and even if it were, it may be desirable to use energy absorbers in conjunction with curved surfaces. Honeycombs by design are orthotropic, meaning axial and transverse loading provoke different bulk material response. Increasing shear strain ratio during mixed mode quasi-static loading has been shown to reduce normal crush strength in regular hexagonal aluminum honeycombs [10]. Although it's expected for each geometry to display reduced energy absorption characteristics, it isn't necessarily true that all degradation will be equal. That is to say, triangular construction may be less sensitive to loading angle than square or hexagonal honeycombs.

6.2 - External Constraints

The geometry chosen are 4x4 structures from Chapter 4 because results across various chapters indicate lateral inertial effects may be present where mass normalization is invoked. All contact and interaction conditions remain the same as Chapter 4, the only difference being the introduction of loading angle β and orientation ϕ. Loading angles zero and ninety correspond to axial only and shear only loading, respectively—anything between is mixed mode. Three different in-plane orientations are chosen; 0°, 45°, and 90°. Hexagonal geometry displays orthotropy when approached using each ϕ whereas square and triangular construction are asymmetric only at ϕ of 45°. The prediction is that energy absorption is predominantly dependent on β and similar where symmetry exists. Loading angles of 0°, 23°, 45°, 68°, and 90° are used at each ϕ to ensure the mixed mode impact spectrum is adequately captured.

Velocity components are controlled such that displacement and velocity magnitudes for the top analytic surface is always 40 mm and 30 m/s, respectively. This ensures the same energy is available for absorption across all simulations and that only cell construction changes energy absorbed. It should be noted that only one simulation of β at 0° is performed for each topology because the response will be the same regardless of ϕ. Namely, normal axial loading produces a

response independent of in-plane orientation because there is no in-plane loading component. Figure 6.2.1 shows how the loading angles β and ϕ are defined.

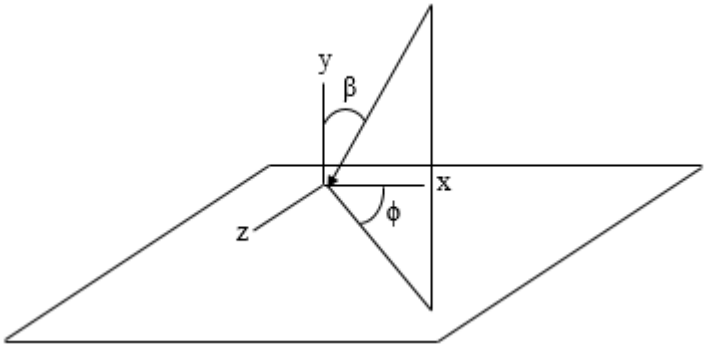

Figure 6.2.1 – Definition of loading and position angles.

Table 6.2.1 – Velocity components during loading.

V_x [m/s]			
ϕ / β	0°	45°	90°
0°	0.00	0.00	0.00
23°	11.48	8.12	0.00
45°	21.21	15.00	0.00
68°	27.72	19.60	0.00
90°	30.00	21.21	0.00
V_y [m/s]			
ϕ / β	0°	45°	90°
0°	-30.00	-30.00	-30.00
23°	-27.72	-27.72	-27.72
45°	-21.21	-21.21	-21.21
68°	-11.48	-11.48	-11.48
90°	0.00	0.00	0.00
V_z [m/s]			
ϕ / β	0°	45°	90°
0°	0.00	0.00	0.00
23°	0.00	8.12	11.48
45°	0.00	15.00	21.21
68°	0.00	19.60	27.72
90°	0.00	21.21	30.00

6.3 - Results

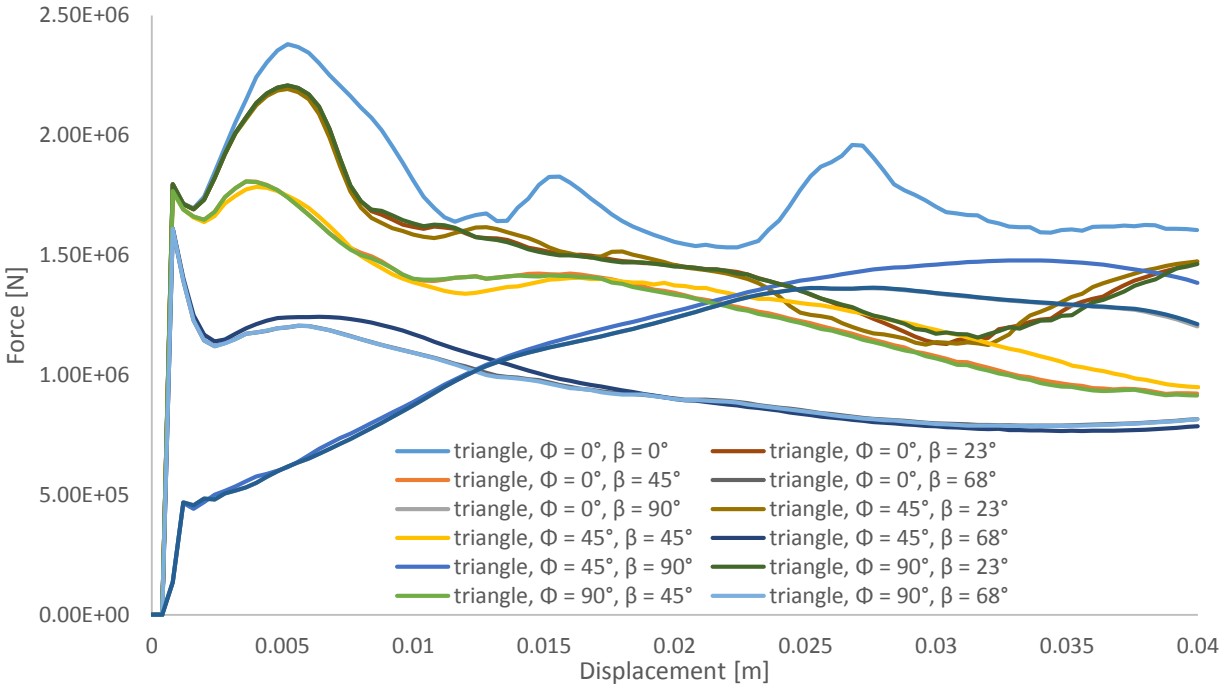

Figure 6.3.1 – Triangular force-displacement response across mixed-mode loading spectrum.

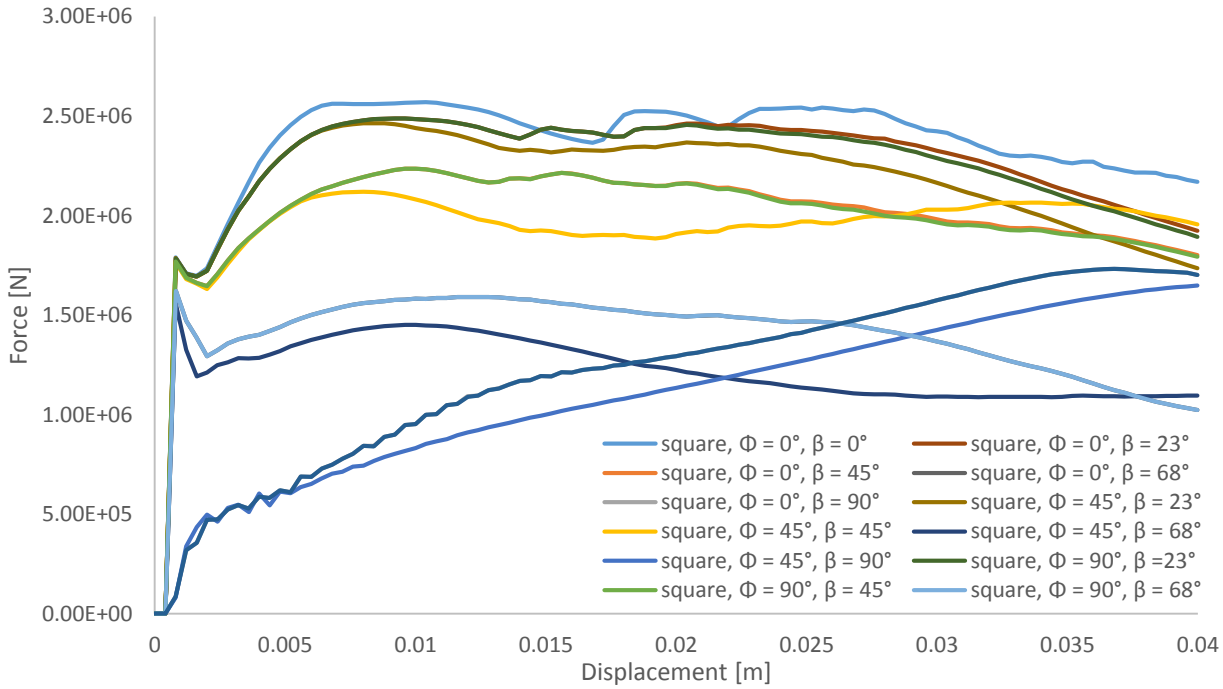

Figure 6.3.2 – Square force-displacement response across mixed-mode loading spectrum.

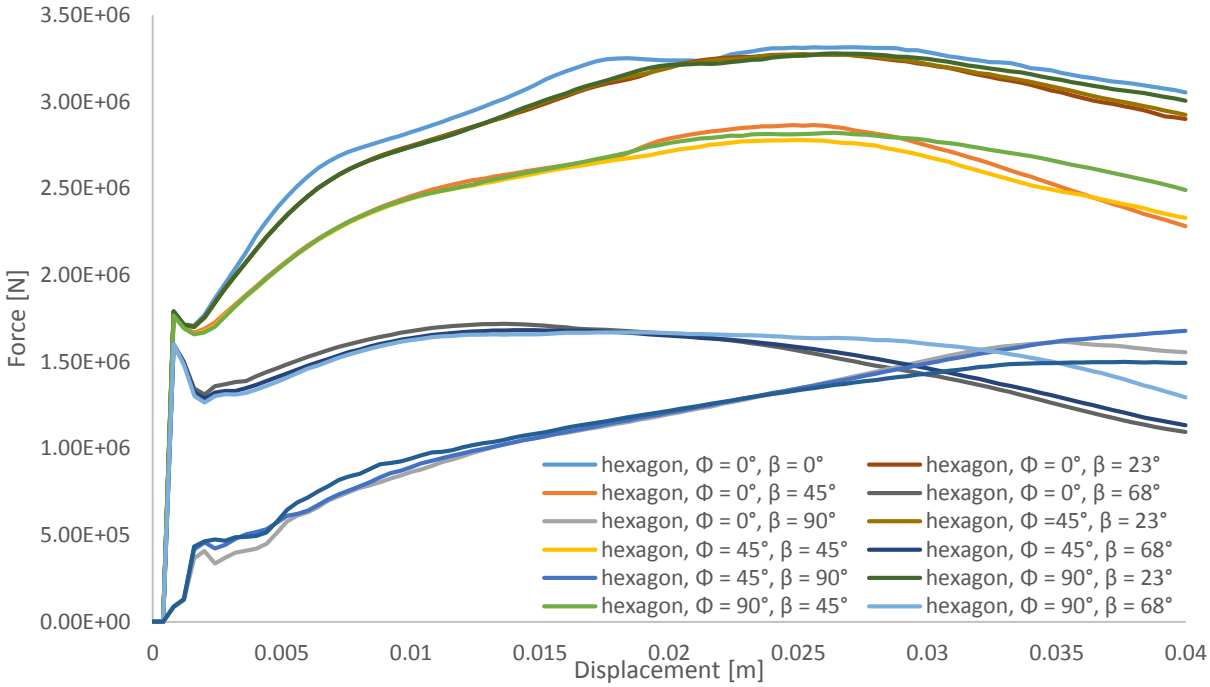

Figure 6.3.3 – Hexagonal force-displacement response across mixed-mode loading spectrum.

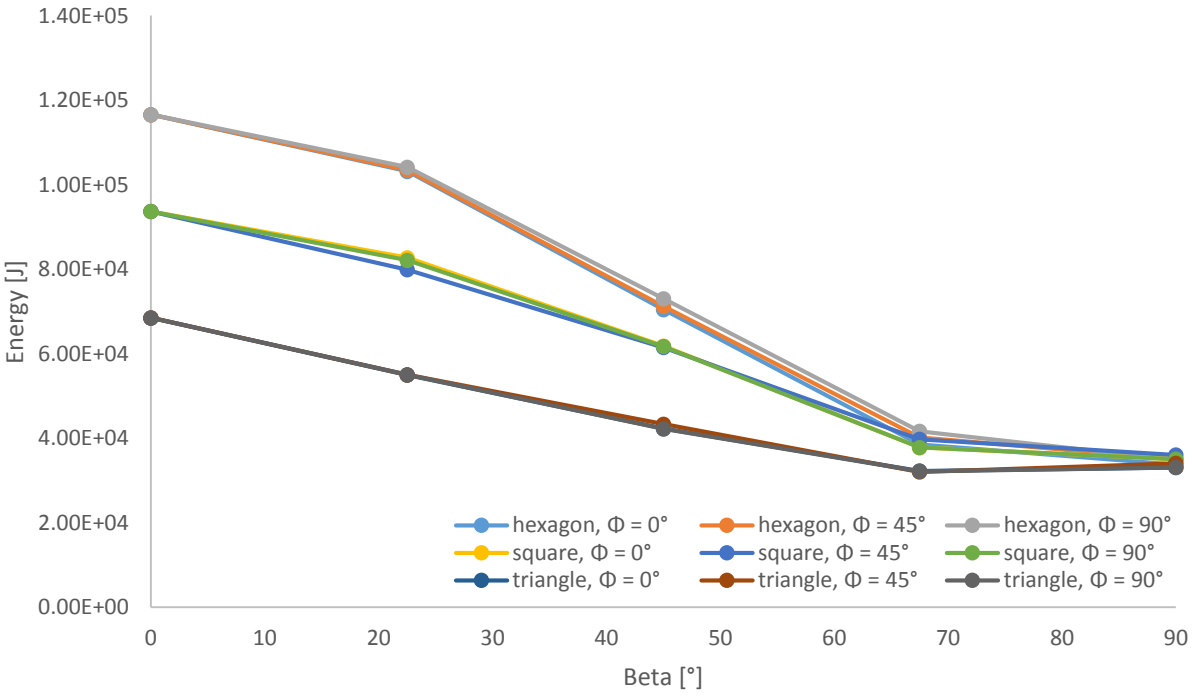

Figure 6.3.4 – Honeycomb energy absorbance across mixed-mode loading spectrum.

6.4 - Discussion

Figure 6.3.4 shows all topologies exhibit progressively reduced energy absorption with increasing shear loading. Hexagonal honeycomb initially absorbs much more energy than square and triangular but all topologies have about the same energy absorbed at β of 68º. Triangular geometry exhibits the least reduction in energy absorbed over the loading range while hexagonal is the most reduced. We see energy absorbed is the same if loading is pure shear, indicating porous honeycomb structure may need filler to increase mixed mode stability. Figure 6.3.4 also shows the examined topologies are relatively unaffected by in-plane orientation.

Chapter 7 - Polyurea as a Void Filler

7.1 - Introduction

Previous chapters proved over and over the performance dominance of the regular hexagonal honeycomb compared to square and triangular geometries. The assumption is then that for most applications, specific energy absorbance will be greater for hexagonal geometry and the other two need not be further investigated. The dominating absorbance parameter was also identified to be out-of-plane aspect ratio *H/L*, where absorbance increases with decreasing *H/L*. The intent of this chapter is to investigate a composite honeycomb system where the voids a filled with a load responsive polymer. The hope is that a composite system will increase specific energy absorption or force shielding. Polyurea is chosen as the filler because it's a very strain-rate sensitive material—having up to a factor of five increase in flow stress during high loading rates [23].Polyurea is also a rubber-like material with hyperelastic and viscoelastic properties. The reason for investigating a composite system is to show that overall energy absorbed as well as specific energy absorbed can be enhanced by using a customized polymer composite system.

7.1.1 - Hyperelasticity

Hyperelastic materials are generally those with large deformation elastic response. Such materials are normally dependent on temperature and loading rate, following a non-linear stress-strain relationship [32]. Such behavior also tends to be volume preserving or nearly incompressible. Several material models exist to describe hyperelastic response by defining strain energy density as a function of material and displacement parameters—Generalized neo-Hookean, Generalized Mooney-Rivlin, Generalized polynomial rubber elasticity potential, Ogden, and Arruda-Boyce eight-chain are just a few of the possible models [33]. This chapter uses the Ogden model—Eq. (7.1.1) describes strain energy density *U* using various material and displacement characteristics.

$$U = \sum_{i=1}^{N} \frac{2\mu_i}{\alpha_i^2}\left(\bar{\lambda}_1^{\alpha_i} + \bar{\lambda}_2^{\alpha_i} + \bar{\lambda}_3^{\alpha_i} - 3\right) + \frac{K_1}{2}(J-1)^2 \tag{7.1.1}$$

$$\sigma_{ij} = \frac{1}{J} F_{ij} \frac{\partial W}{\partial F_{jk}} \tag{7.1.2}$$

$$\sigma_{ij} = \frac{\lambda_1}{\lambda_1\lambda_2\lambda_3}\frac{\partial U}{\partial \lambda_1} b_i^{(1)} b_j^{(1)} + \frac{\lambda_2}{\lambda_1\lambda_2\lambda_3}\frac{\partial U}{\partial \lambda_2} b_i^{(2)} b_j^{(2)} + \frac{\partial U}{\partial \lambda_3}\frac{\lambda_3}{\lambda_1\lambda_2\lambda_3} b_i^{(3)} b_j^{(3)} \tag{7.1.3}$$

In this equation, $\bar{\lambda}$ and J represent space or displacement states while the others are material properties. After massaging Eq. (7.1.2), Cauchy stress σ_{ij} can be described by strain energy density and principle stretches in a form compliant with the Ogden model as seen in Eq. (7.1.3) [33]. Here, $b_i^{(n)}$ and $b_j^{(n)}$ represent eigenvectors of the Left Cauchy Green deformation tensor. See Appendix A for more detail. Abaqus allows for the specification of the constants for an Ogden or other models, or it can find the constants given test data. The latter is the process used for this chapter.

7.1.2 - Viscoelasticity

Some materials, polymers in particular, have a time sensitive response when loaded. This is due primarily to the molecular construction of the material but can be exacerbated by dynamic loading and environmental parameters such as temperature. Eq. (7.1.4) shows Shear modulus G as a function of steady-state stiffness and summation of stiffness's and time constants [33]. This is known as a relaxation modulus because it minimizes over time. This summation process is also known as a Prony series. Supplied with relaxation test data, Abaqus assembles a Prony Series and uses it when solving viscoelastic problems. The Prony Series can be used to describe the stress response over time by inserting Eq. (7.1.4) into Eq. (7.1.5), where t, γ, σ, and C are time, shear stress, shear strain, and strain-rate [34]. See Appendix A for more detail.

$$G(t) = G_\infty + \sum_{i=1}^{N} G_i e^{-t/t_i} \tag{7.1.4}$$

$$\sigma(t) = \int_0^t G(t'-t)\frac{d\gamma(t')}{dt'}dt' \tag{7.1.5}$$

7.2 - Setup

The response of AISI 304 Stainless Steel core composite was first investigated, then a reduced height polypropylene composite. This allows for large and small compliance mismatch between core and filler materials to be investigated. The density used for Polyurea filler is 1070 kgm^{-3}. Hyperelastic and viscoelastic material model information is given by Figure 7.2.1 [35]. This test data is input to Abaqus and no further hyperelastic/viscoelastic information is required. Ogden and Prony series coefficients can then be output as seen in Table 7.2.1 and Table 7.2.2.

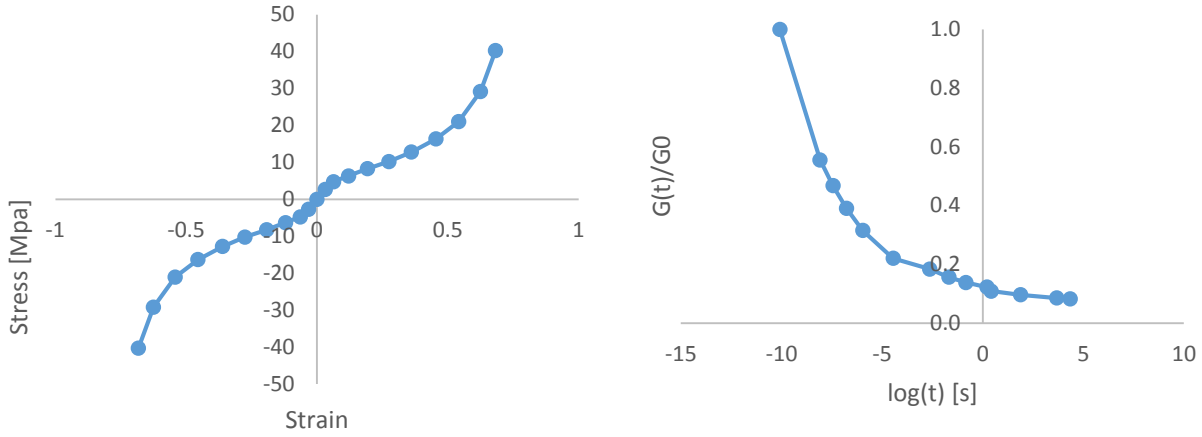

Figure 7.2.1 – Hyperelastic stress-strain response (left) and normalized relaxation modulus (right) for polyurea.

Table 7.2.1 – Ogden hyperelasticity model coefficient results from Abaqus.

i	μ_i	α_i
1	4.8483E+08	1.6443
2	-1.7415E+08	2.2705
3	-2.9538E+08	1.0209

Table 7.2.2 – Prony series constants for viscoelastic relaxation modulus via Abaqus.

i	G_i	t_i
1	5.0041E-01	4.0766E-09
2	1.7857E-01	1.8341E-07
3	1.3058E-01	2.4260E-05
4	4.8673E-02	1.7878E-02
5	4.4928E-02	2.4344
6	1.4124E-02	3.1241E+03

Table 7.2.3 – Mass makeup of composites.

	Mass [g]	Pieces	Total [g]
Composite 1			
Steel core	3700	1	3700
PU filler	138.1	14	1933
TOTAL			**5633**
Composite 2			
PP core, short	41.68	1	41.68
PU filler, short	13.81	14	193.3
TOTAL			**235.0**

A large displacement stress-strain response curve is used to model polypropylene [36] and density 909 kgm^{-3} is used [37]. The same material model for AISI 304 stainless steel is used as in previous chapters. It's important for all masses to be tabulated for easily comparing specific energy absorption, so each composite component is modeled in SolidWorks to accurately calculate mass. Composites 1 has the same core dimensions as the previous chapter. Composite 2 has the same in-plane dimensioning but is only extruded to 10% percent of the total length. The reason for using a reduced height composite is to decrease stress wave oscillation and overall dynamic equilibration time, concerning material response. Table 7.2.3 shows the mass composition of each system.

It's important to consider how a hyperelastic viscoplastic material responds to dynamic loading. If the material is long, the shocked volume may exhibit drastically different material properties compared to the unshocked end. By reducing the specimen height, we're effectively forcing the polymer to equilibrate faster and display a bulk response. A quickly equilibrated bulk response is desirable considering our material model for polyurea displays rapid relaxation characteristics. It's also expected to see enhanced energy absorption during high strain-rate loading. In hopes of provoking such enhanced properties, loading rates of 50 s^{-1}, 300 s^{-1}, 3000 s^{-1} are used.

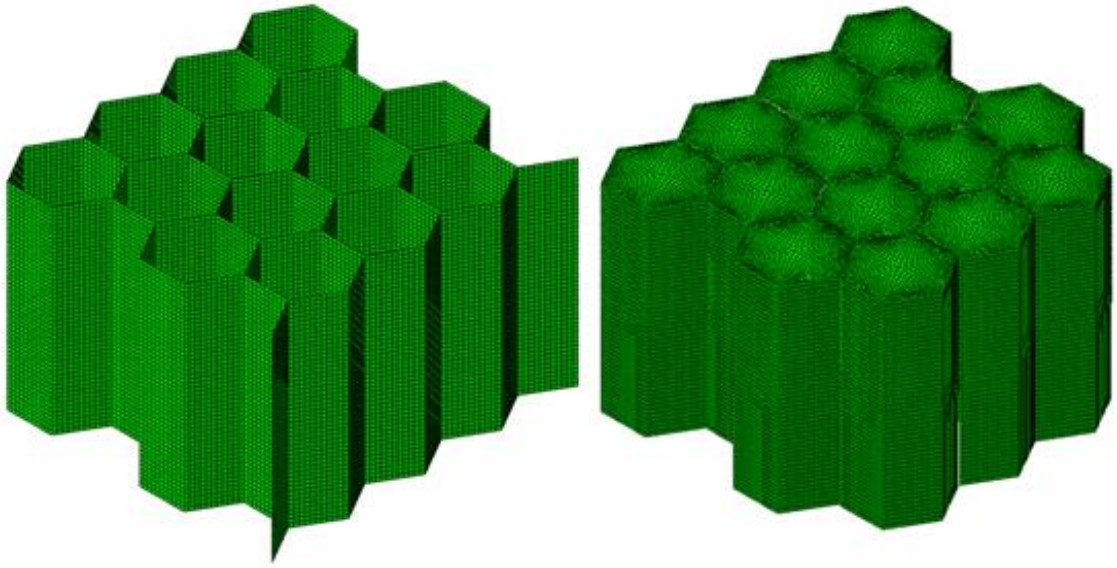

Figure 7.2.2 – Meshed core (left) and filler (right) parts of each composite system.

Every composite is essentially a sum of its parts however not all parts are created equally depending on the response in question. We hope to obtain better results in the composite form

than either part can display independently. It's then necessary to load each part of the system independently as well the composite. This leads to three simulations for each system at each loading rate, making a total of six simulations. The composite system is composed of a honeycomb core and polyurea, represented as shell and solid elements, respectively. It's assumed the polyurea is bonded to the core such that no displacements or rotations occur at the core/PU interface. This is a fair assumption considering polyurea is often used as a fast setting spray coating where good surface bonding is essential for performance [38]. Tie bonding at the nodes of shell and brick elements introduces error in the form of density overlap near the nodal region. This overlap region is equal to half the core thickness due to the shell occupying a mid-surface position. This error becomes neglibeable when considering the compliance of polyurea compared to steel.

7.3 - Results

7.3.1 - Composite 1

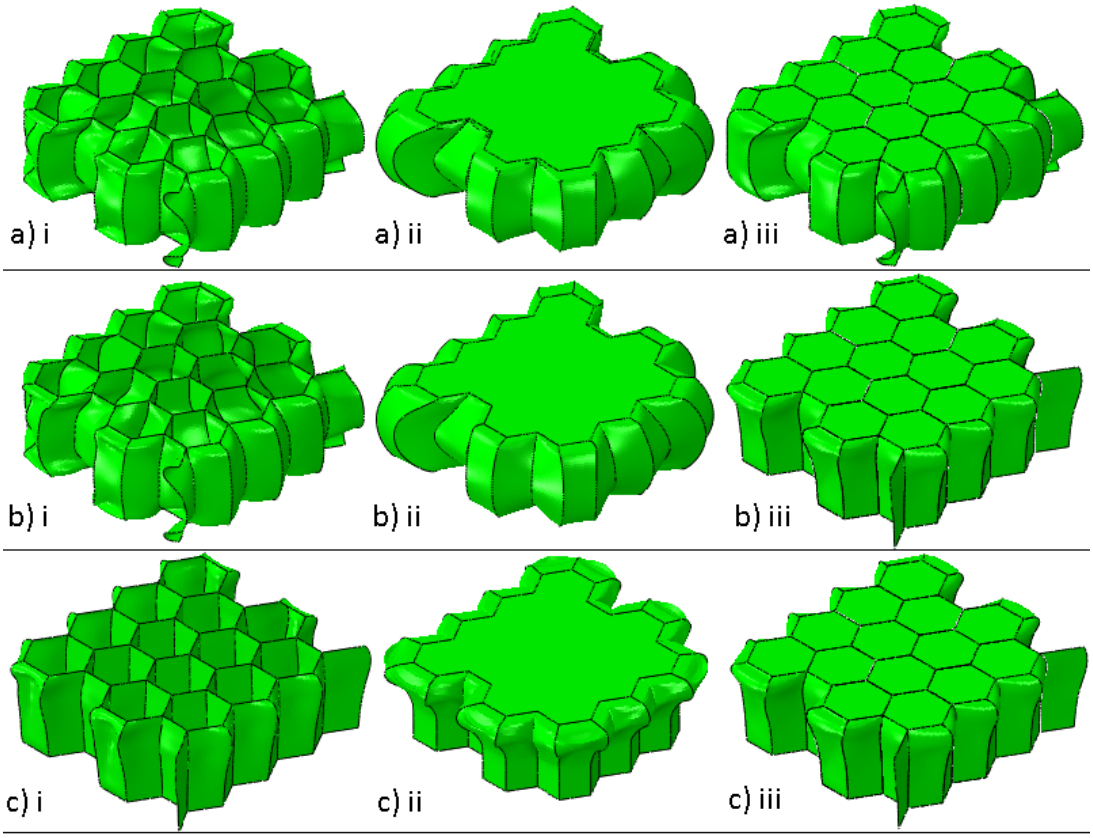

Figure 7.3.1 – Response of (i) core, (ii) polyurea, and (iii) composite, respectively. Loading rate is a) 50 s^{-1} b) 300 s^{-1}, and c) 3000 s^{-1}.

Table 7.3.1 – Energy absorbed by Composite 1 piecewise and systematically.

5 m/s

	mass [kg]	E [J]	e [J/kg]
core	3.696	1.040E+05	2.814E+04
filler	1.933	1.392E+04	7.199E+03
comp-tot	5.629	1.227E+05	2.180E+04
IMPROVEMENT OVER CORE		**18.0%**	**-22.5%**
IMPROVEMENT OVER PU		**781.7%**	**202.8%**

30 m/s

	mass [kg]	E [J]	e [J/kg]
core	3.696	1.069E+05	2.894E+04
filler	1.933	1.488E+04	7.695E+03
comp-tot	5.629	1.260E+05	2.238E+04
IMPROVEMENT OVER CORE		**17.8%**	**-22.7%**
IMPROVEMENT OVER PU		**746.9%**	**190.9%**

300 m/s

	mass [kg]	E [J]	e [J/kg]
core	3.696	1.727E+05	4.673E+04
filler	1.933	5.143E+04	2.660E+04
comp-tot	5.629	2.371E+05	4.212E+04
IMPROVEMENT OVER CORE		**37.3%**	**-9.9%**
IMPROVEMENT OVER PU		**361.0%**	**58.3%**

Table 7.3.1 shows that energy absorbed by the composite increases at least 17.8% and 360% when compared to the core and filler, respectively. The most energy is absorbed during the high strain-rate loading case. Comparing each component and the composite at low and high strain-rates, we see the core, polyurea, and system increase their energy absorbed by 66%, 269%, and 93%, respectively. Results for specific energy however, are less impressive. Table 7.3.1 shows the composite has increasing specific energy absorbed as strain-rate increases but is always less than the specific energy absorbed by the core. The opposite is true when comparing the composite to polyurea, where polyurea always has more specific energy absorbed but has this value decrease with higher strain-rate.

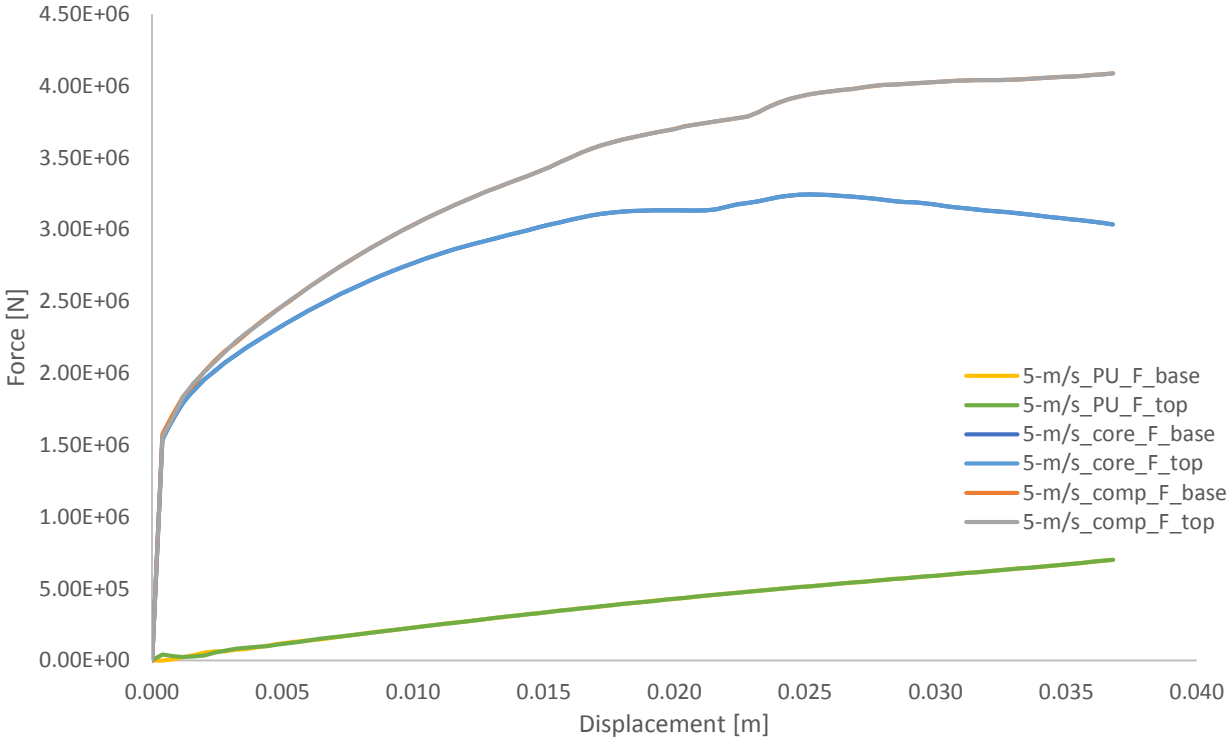

Figure 7.3.2 – Force-displacement plots for Composite 1 at 50 s^{-1} strain rate.

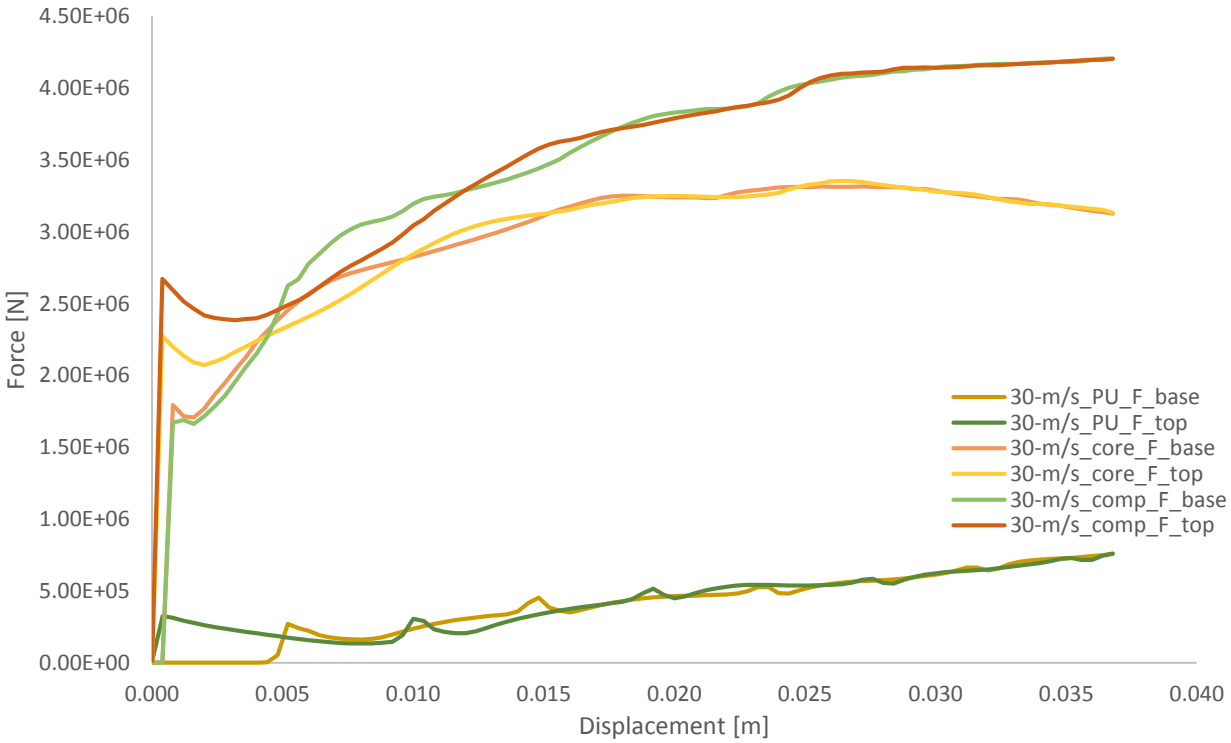

Figure 7.3.3 – Force-displacement plots for Composite 1 at 300 s^{-1} strain rate.

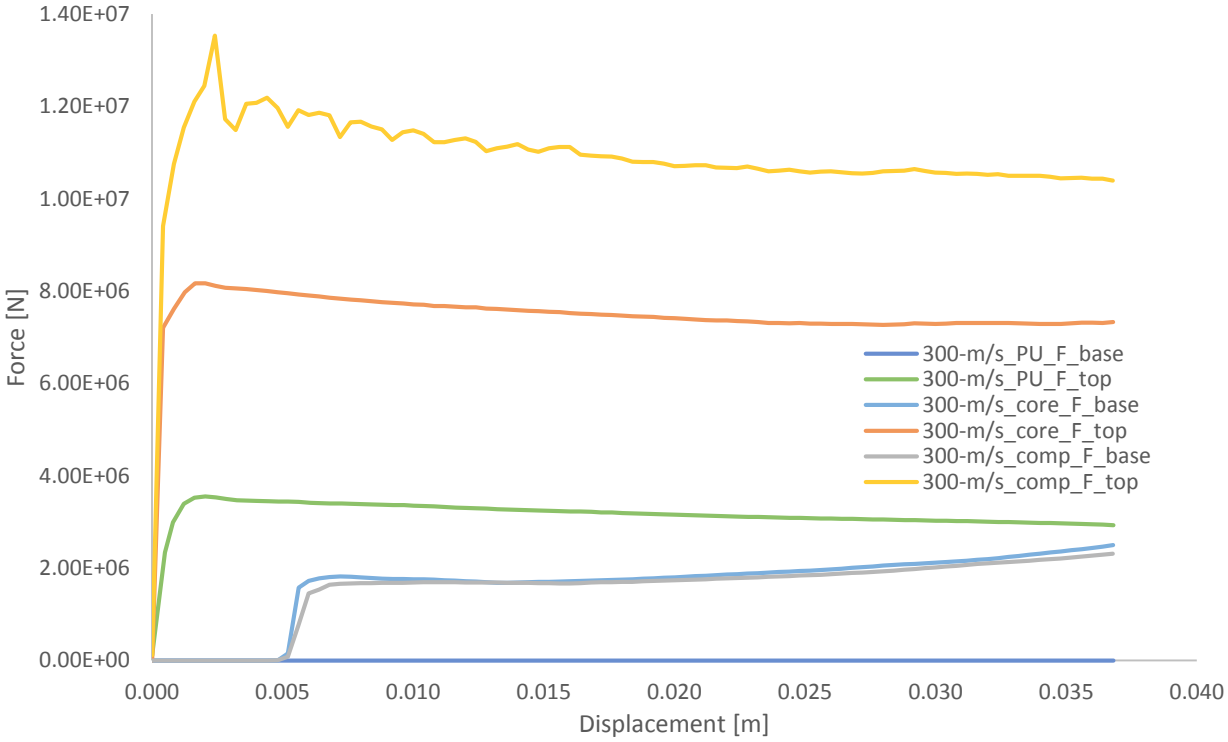

Figure 7.3.4 – Force-displacement plots for Composite 1 at 3000 s^{-1} strain rate.

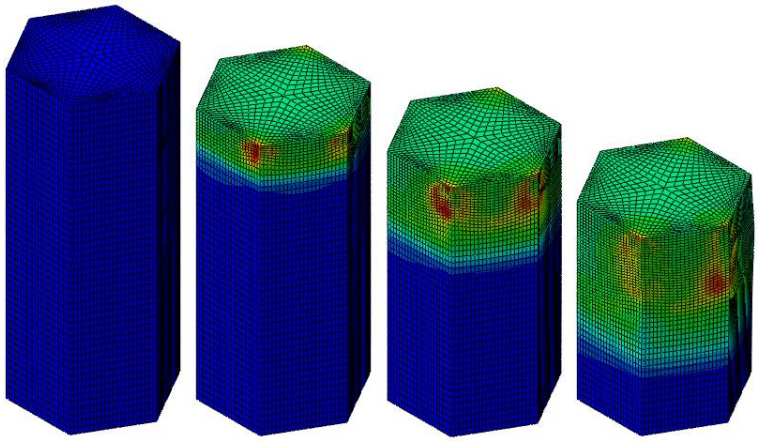

Figure 7.3.5 – Stress wave propogation over 3000 s^{-1} loading period.

Figure 7.3.2 shows the core and composite have sharp increases in force to peak value followed by polynomial increase compared to polyurea, which has a linear increase in force. Peak forces are approximately the same for the core and composite, both being substantially higher than polyurea. We see little or no oscillation between respective top and bottom forces throughout this low strain-rate loading. Figure 7.3.3 shows the same general peak force behavior over time

however the latency due to wave oscillation is more pronounced. A clear peak force mismatch is present when observing the response of each component and composite—being especially true for polyurea, where a peak force doesn't occur on the bottom surface for about 12% of the loading period. Figure 7.3.4 shows a very large disagreement between force response on the top and bottom surfaces. Polyurea registers little if any force on its' bottom surface throughout the duration of loading, this is easily confirmed by observing the stress wave propagation in Figure 7.3.5.

7.3.2 - Composite 2

Table 7.3.2 – Energy absorbed by Composite 2 piecewise and systematically.

	0.5 m/s		
	mass [kg]	E [J]	e [J/kg]
core	0.0417	5.745E+02	1.378E+04
filler	0.1933	3.842E+03	1.987E+04
comp-tot	0.2350	4.550E+03	1.936E+04
IMPROVEMENT OVER CORE		**692.0%**	**40.5%**
IMPROVEMENT OVER PU		**18.4%**	**-2.6%**
	3 m/s		
	mass [kg]	E [J]	e [J/kg]
core	0.0417	5.916E+02	1.419E+04
filler	0.1933	3.890E+03	2.012E+04
comp-tot	0.2350	4.598E+03	1.956E+04
IMPROVEMENT OVER CORE		**677.1%**	**37.8%**
IMPROVEMENT OVER PU		**18.2%**	**-2.8%**
	30 m/s		
	mass [kg]	E [J]	e [J/kg]
core	0.0417	7.099E+02	1.703E+04
filler	0.1933	4.110E+03	2.126E+04
comp-tot	0.2350	4.838E+03	2.058E+04
IMPROVEMENT OVER CORE		**581.5%**	**20.9%**
IMPROVEMENT OVER PU		**17.7%**	**-3.2%**

Table 7.3.2 shows that energy absorbed by the composite increases at least 580% and 17.7% when compared to the core and filler, respectively. As before, the most energy is absorbed during high strain-rate loading. Comparing each component and the composite at low and high strain-rates, we see the core, polyurea, and system increased their energy absorbed by 23%, 7%, and 6%, respectively. Oppose to Composite 1, this system shows consistently greater specific energy absorption when compared to the core but less when compared to polyurea.

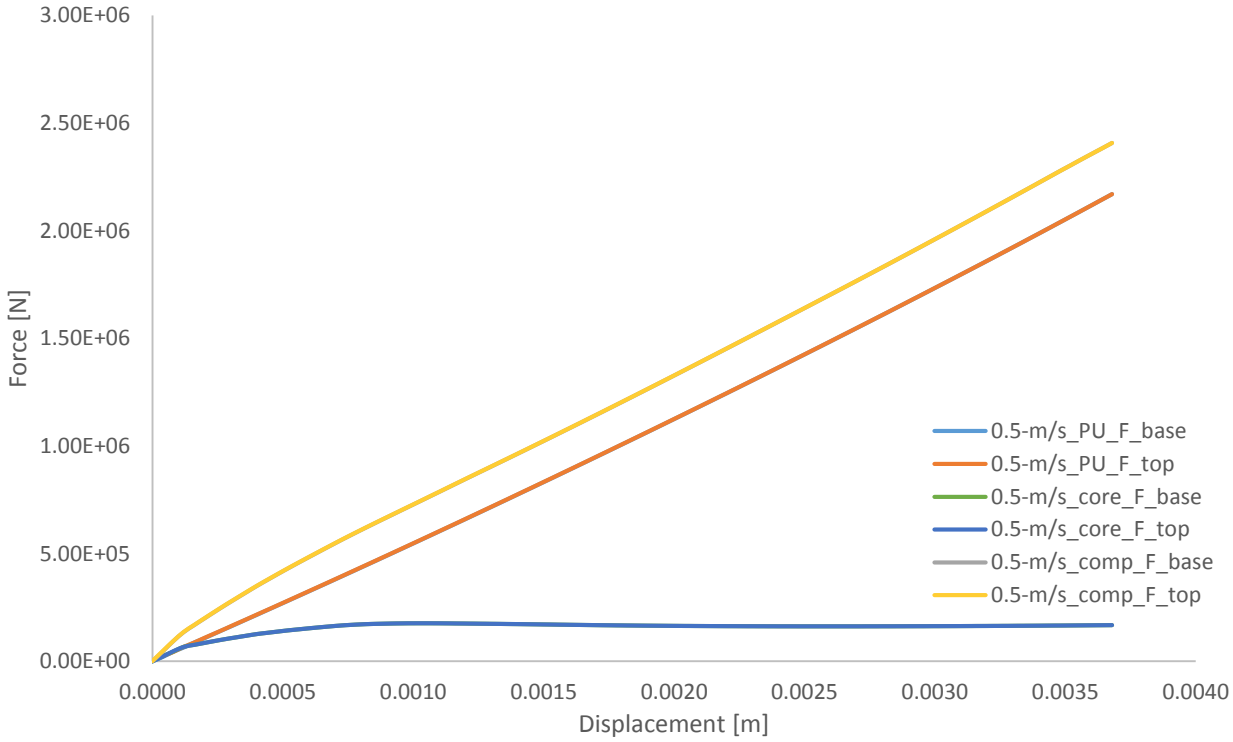

Figure 7.3.6 – Force-displacement plots for Composite 2 at 50 s^{-1} strain rate.

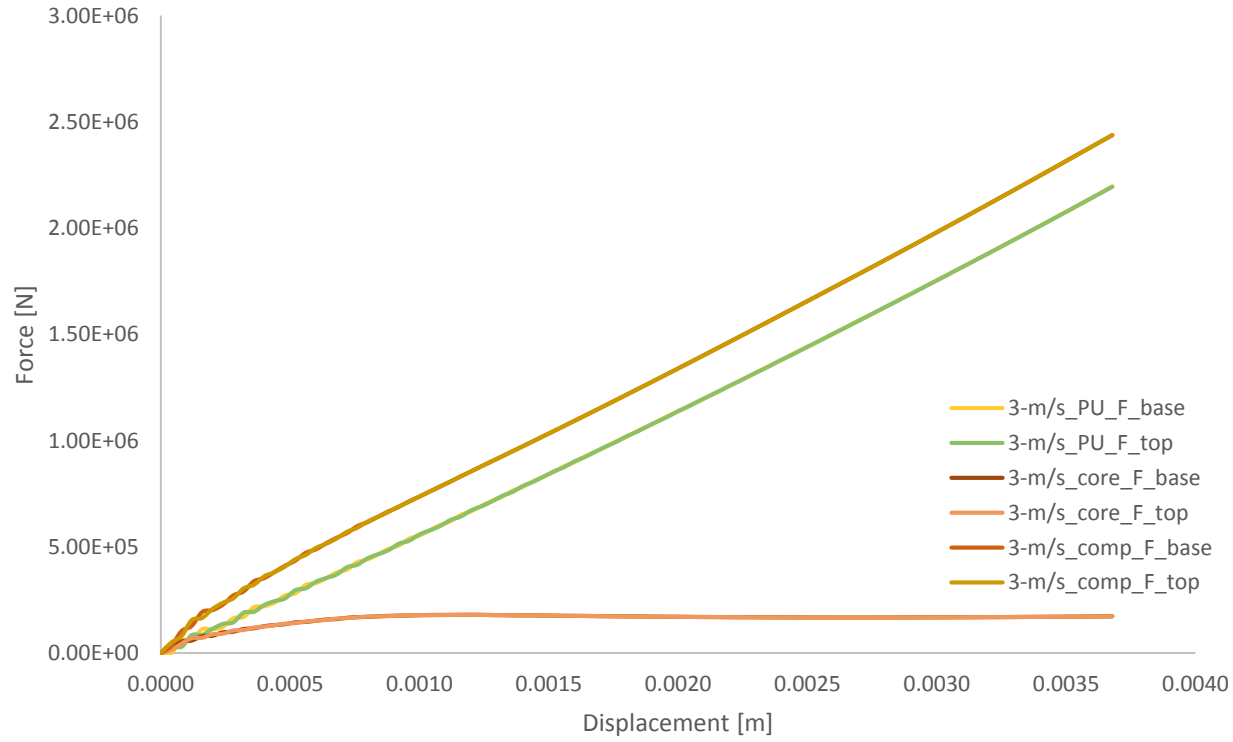

Figure 7.3.7 – Force-displacement plots for Composite 2 at 300 s^{-1} strain rate.

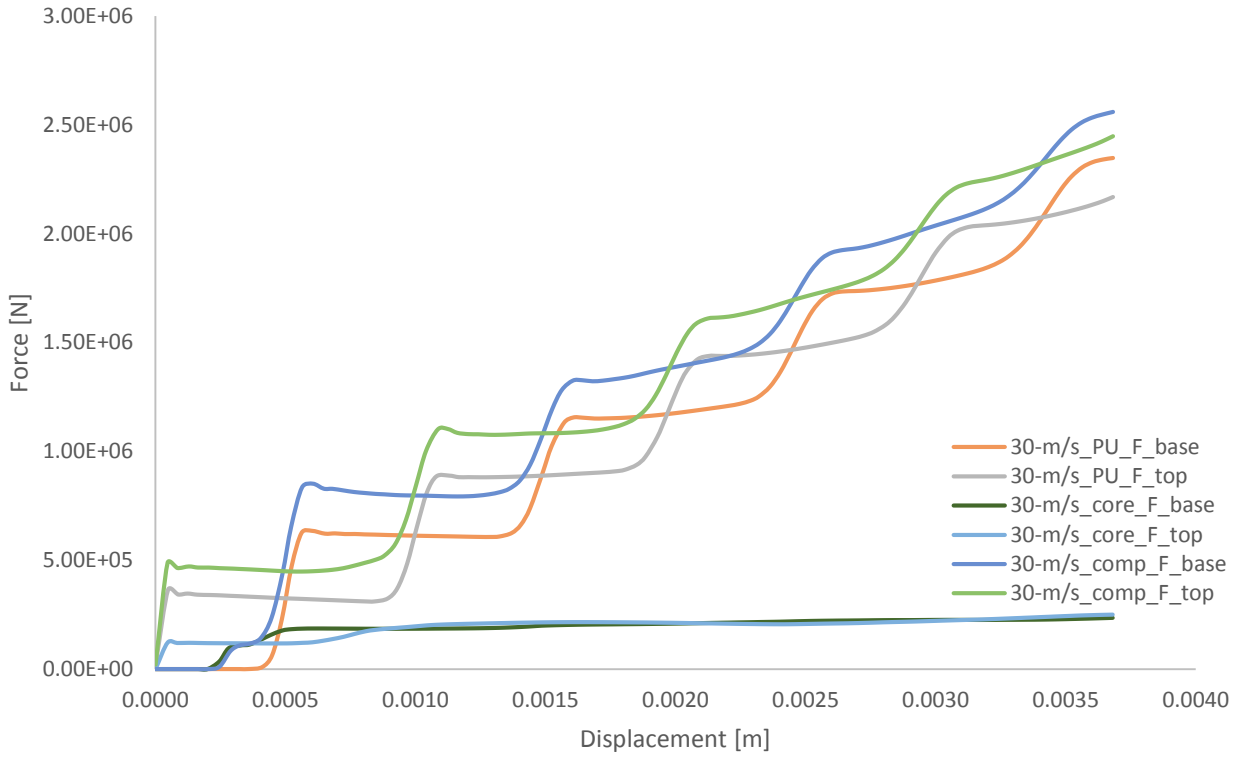

Figure 7.3.8 – Force-displacement plots for Composite 2 at 3000 s^{-1} strain rate.

Figure 7.3.6 and Figure 7.3.7 show that polyurea is the force determinant material since its force-displacement response is very nearly that of the composite. Figure 7.3.7 shows a little oscillation during the beginning of loading but pales in comparison to the high strain-rate case seen in Figure 7.3.8. The shock of the impact gives almost step-wise force oscillation at the beginning, transitioning to smoother oscillations as loading continues. As with the previous composite, this system does not reach a dynamic equilibrium before the end of high strain-rate loading.

7.4 - Discussion

The effect of using a hyper-viscoelastic polymer as the filler in a composite honeycomb system has been investigated using two different core materials and heights. Key points are: Filler specimen height can significantly impact dynamic equilibration time and inherently, bulk and specific energy absorption for polyurea; and Changing core material is a feasible way to control specific energy absorption or force shielding potential. The enhanced material properties of polyurea have also been verified by using 3000 s^{-1} strain-rate, although it's important to note such enhancement is highly dependent on specimen height.

Conclusion

This work has investigated the dynamic topological strength characteristics and energy absorbance of regular hexagonal, triangular, and square honeycombs subjected to normal and mixed mode loading. Results over the length scales examined strongly indicate that hexagonal geometry has higher specific and overall energy absorption during all modes of loading when compared to triangular or square geometry. The controlling mechanism is identified as a combination of plastic hinge wavelength and amplitude present in each buckling leg. Material between hinges has reduced energy absorbed due to the increased compliance of surrounding hinges. Accordingly, lateral buckling behavior is responsible for reduced energy absorption. Reducing out-of-plane aspect ratio *H/L* is identified as an efficient way to reduce hinge formation, increasing specific energy absorption.

The topological results were used to create a void filled honeycomb composites, revealing further enhancements can be achieved with polymer-composites—this work involved a hyper-viscoelastic polymer void filler. Results show the steel core system had reduced specific energy absorbed at all loading rates when compared to the steel core alone, while the polypropylene core system had improved specific energy absorption at all loading rates when compared to the polypropylene core alone. The difference between absorption abilities of steel and polypropylene cored composites is attributed to the large and small compliance mismatch present between core and filler—namely, steel and polyurea have a large compliance mismatch while polypropylene and polyurea have a much smaller compliance mismatch. Even so, both composites had more overall energy absorbed when compared to the core alone. Most importantly, polymer-composite systems with rate-responsive filler display potential as highly customizable energy absorbers.

References

[1] L. J. Gibson and M. F. Ashby, *Cellular solids - Structure and properties*, 2nd ed., 1997.

[2] Hexcel. (2013). *Honeycomb Energy Absorbers*. Available: http://www.hexcel.com/Solutions/Industries/IHoneycomb-Energy-Absorbers

[3] Plascore. (2013). *Energy Absorbers*. Available: http://www.plascore.com/energy_absorbers.php

[4] T. Wierzbicki, "Crushing analysis of metal honeycombs," *International Journal of Impact Engineering,* vol. 1, pp. 157-174, // 1983.

[5] R. K. McFarland, "Hexagonal cell structures under post-buckling axial load," *AIAA,* vol. 1, pp. 1380-1385, 1963.

[6] E. Wu and W.-S. Jiang, "Axial crush of metallic honeycombs," *International Journal of Impact Engineering,* vol. 19, pp. 439-456, 5// 1997.

[7] F. Côté, V. S. Deshpande, N. A. Fleck, and A. G. Evans, "The out-of-plane compressive behavior of metallic honeycombs," *Materials Science and Engineering: A,* vol. 380, pp. 272-280, 8/25/ 2004.

[8] A. Spadoni, M. Ruzzene, and F. Scarpa, "Global and local linear buckling behavior of a chiral cellular structure," *physica status solidi (b),* vol. 242, pp. 695-709, 2005.

[9] M. Yamashita and M. Gotoh, "Impact behavior of honeycomb structures with various cell specifications—numerical simulation and experiment," *International Journal of Impact Engineering,* vol. 32, pp. 618-630, 12// 2005.

[10] S. T. Hong, J. Pan, T. Tyan, and P. Prasad, "Quasi-static crush behavior of aluminum honeycomb specimens under compression dominant combined loads," *International Journal of Plasticity,* vol. 22, pp. 73-109, 1// 2006.

[11] S. T. Hong, J. Pan, T. Tyan, and P. Prasad, "Quasi-static crush behavior of aluminum honeycomb specimens under non-proportional compression-dominant combined loads," *International Journal of Plasticity,* vol. 22, pp. 1062-1088, 6// 2006.

[12] D. D. Radford, G. J. McShane, V. S. Deshpande, and N. A. Fleck, "Dynamic Compressive Response of Stainless-Steel Square Honeycombs," *Journal of Applied Mechanics,* vol. 74, pp. 658-667, 2006.

[13] M. R. Said and T. Chee-Fai, "Aluminum honeycomb under quasi-static compressive loading: an experimental investigation," *Suranaree Journal of Science & Technology,* vol. 16, pp. 1-8, 2009.

[14] Z. Q. Yang, B. J. Pang, and L. W. Wang, "Numerical and Experimental Investigation for Assessing the High Strain Rate Response of Nickel Based Multi-layerd Honeycomb Sandwiches," *AIP Conference Proceedings,* vol. 1195, pp. 1435-1438, 2009.

[15] G. Caserta, U. Galvanetto, and L. Iannucci, "Static and Dynamic Energy Absorption of Aluminum Honeycombs and Polymeric Foams Composites," *Mechanics of Advanced Materials and Structures,* vol. 17, pp. 366-376, 2010/06/24 2010.

[16] L. Aktay, C. Çakıroğlu, and M. Güden, "Quasi-Static Axial Crushing Behavior of Honeycomb-Filled Thin-Walled Aluminum Tubes," *Open Materials Science Journal,* vol. 5, pp. 184-193, 2011.

[17] M. Z. Mahmoudabadi and M. Sadighi, "A Study on Metal Hexagonal Honeycomb Crushing Under Quasi-Static Loading," *Proceedings of World Academy of Science: Engineering & Technology,* vol. 53, pp. 677-681, 2009.

[18] M. H. Bing, "Dynamic enhancement and multi-axial behavior of honeycombs under combined shear-compression," Dissertation, Laboratoire de Mécanique et Technologie, 2011.
[19] M. G. Stout and P. S. Follansbee, "Strain Rate Sensitivity, Strain Hardening, and Yield Behavior of 304L Stainless Steel," *Journal of Engineering Materials and Technology,* vol. 108, pp. 344-353, 1986.
[20] J. E. F. S.M. Walley, "Strain rate sensitivity of polymers in compression from low to high rates," *DYMAT,* vol. 1, pp. 211-227, September 1994 1994.
[21] S. Ouellet, D. Cronin, and M. Worswick, "Compressive response of polymeric foams under quasi-static, medium and high strain rate conditions," *Polymer Testing,* vol. 25, pp. 731-743, 9// 2006.
[22] G. Subhash, Q. Liu, and X.-L. Gao, "Quasistatic and high strain rate uniaxial compressive response of polymeric structural foams," *International Journal of Impact Engineering,* vol. 32, pp. 1113-1126, 7// 2006.
[23] S. S. Sarva, S. Deschanel, M. C. Boyce, and W. Chen, "Stress–strain behavior of a polyurea and a polyurethane from low to high strain rates," *Polymer,* vol. 48, pp. 2208-2213, 4/5/ 2007.
[24] K. L. Ehinger D., Krause S., Martin U., Weigelt C., Aneziris, C. G., "Dynamic impact response of high-density square honeycombs made of TRIP steel and TRIP matrix composite material," in *EPJ Web of Conferences 2012, Issue 26, Special section p1*, 2012, p. Special section p1.
[25] W. Moćko, J. A. Rodríguez-Martínez, Z. L. Kowalewski, and A. Rusinek, "Compressive Viscoplastic Response of 6082-T6 and 7075-T6 Aluminium Alloys Under Wide Range of Strain Rate at Room Temperature: Experiments and Modelling," *Strain,* vol. 48, pp. 498-509, 2012.
[26] Y. U. Shui-sheng, L. U. Yu-bin, and C. A. I. Yong, "The strain-rate effect of engineering materials and its unified model," *Latin American Journal of Solids & Structures,* vol. 10, pp. 833-844, 2013.
[27] A. F. Bower, "Applied Mechanics of Solids - Ch 8," ed, 2010, pp. 467-545.
[28] D. Systemes. *Abaqus Analysis User's Manual - Section 6.3.3*.
[29] D. Systemes. *Abaqus Theory Manual - Section 2.4.5*.
[30] M. Farshad, *Design and Analysis of Shell Structures*, 1992.
[31] Plascore. (2013). *Plascore CrushLite*. Available: http://www.plascore.com/energy_absorbers.php
[32] I. M. Ward, "An Introduction to the Mechanical Properties of Solid Polymers," 2 ed, 2004, pp. 53-76.
[33] A. F. Bower, "Applied Mechanics of Solids," 1 ed, 2010, pp. 93-102.
[34] M. Alkhader, W. G. Knauss, and G. Ravichandran, "A New Shear-Compression Test for Determining the Pressure Influence on the Shear Response of Elastomers," *Experimental Mechanics,* vol. 52, pp. 1151-1161, 2012/10/01 2012.
[35] M. Alkhader, W. Knauss, and G. Ravichandran, "Experimental Investigation of Failure in Viscoelastic Elastomers Under Combined Shear and Pressure," in *Challenges in Mechanics of Time-Dependent Materials and Processes in Conventional and Multifunctional Materials, Volume 2*, B. Antoun, H. J. Qi, R. Hall, G. P. Tandon, H. Lu, and C. Lu, Eds., ed: Springer New York, 2013, pp. 55-62.

[36] K. Kaneko, "Inelastic deformation behaviour of polypropylene in large strain region and after cyclic preloadings," *Defence Science Journal*, vol. 58, pp. 200-208, 2008.
[37] I. O. P. USA, "Typical Engineering Properties of Polypropylene," 2010.
[38] M. Broekaert, "Polyurea spray coatings-The technology and latest developments," 2002.

Appendix A

Deformation gradient tensor F_{ij} in terms of undeformed x_i and deformed X_i configuration

$$F_{ij} = \delta_{ij} + \frac{\partial x_i}{\partial X_j} \tag{7.4.1}$$

Kronecker delta function δ_{ij}

$$\delta_{ij} = \begin{cases} 0, & if\ i \neq j \\ 1, & if = j \end{cases} \tag{7.4.2}$$

Jacobian *J*

$$J = det(F_{ij}) \tag{7.4.3}$$

Left Cauchy-Green deformation tensor B_{ij}

$$B_{ij} = F_{ik}F_{jk} \tag{7.4.4}$$

Principle stretches λ_i in terms of eigenvalues of B_{ij}

$$\lambda_i = \sqrt{e_i} \tag{7.4.5}$$

Adjusted principle stretch $\bar{\lambda}_i$

$$\bar{\lambda}_i = \frac{\lambda_i}{J^{1/3}} \tag{7.4.6}$$

Shear strain γ

$$\gamma = Ct \tag{7.4.7}$$

Shear modulus *G*

$$G(t) = \frac{\partial \sigma}{\partial \gamma} = \frac{1}{C}\frac{\partial \sigma}{\partial t} \tag{7.4.8}$$